

2008

## Synthesis and field emission properties of carbon nanostructures

Kun Hou

*College of William & Mary - Arts & Sciences*

Follow this and additional works at: <https://scholarworks.wm.edu/etd>



Part of the [Condensed Matter Physics Commons](#), [Electrical and Computer Engineering Commons](#), and the [Materials Science and Engineering Commons](#)

---

### Recommended Citation

Hou, Kun, "Synthesis and field emission properties of carbon nanostructures" (2008). *Dissertations, Theses, and Masters Projects*. Paper 1539623523.

<https://dx.doi.org/doi:10.21220/s2-dn2g-zn95>

This Dissertation is brought to you for free and open access by the Theses, Dissertations, & Master Projects at W&M ScholarWorks. It has been accepted for inclusion in Dissertations, Theses, and Masters Projects by an authorized administrator of W&M ScholarWorks. For more information, please contact [scholarworks@wm.edu](mailto:scholarworks@wm.edu).

**Synthesis and Field Emission Properties of Carbon Nanostructures**

**Kun Hou**

**Harbin, Heilongjiang Province, P.R. China**

**M.E., Materials Science and Engineering, Zhejiang University, 2003  
B.E., Materials Science and Engineering, Zhejiang University, 1998**

**A Dissertation presented to the Graduate Faculty  
of the College of William and Mary in Candidacy for the Degree of  
Doctor of Philosophy .**

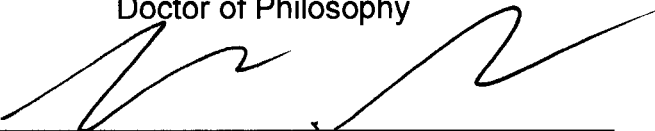
**Department of Applied Science**

**The College of William and Mary  
January, 2008**

## APPROVAL PAGE

This Dissertation is submitted in partial fulfillment of  
the requirements for the degree of

Doctor of Philosophy



---

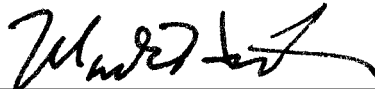
Kun Hou

Approved by the Committee, September, 2007



---

Committee Chair  
CSX Professor Dennis Manos, Applied Science  
College of William and Mary



---

Professor Mark Hinders, Applied Science,  
College of William and Mary



---

Research Professor Ron Outlaw, Applied Science  
College of William and Mary



---

Professor Jack Kossler, Physics  
College of William and Mary

## ABSTRACT PAGE

This dissertation focuses on developing carbon nanostructures for application as the electron emissive material in novel back-gated triode field emission devices. The synthesis, characterization, and field emission properties of carbon nanostructures, including 1-D carbon nanofibers (CNF), 2-D carbon nanosheets (CNS), and chromium oxide coated carbon nanosheets ( $\text{CrO}_x\text{-CNS}$ ), are presented in this work.

First, we have fabricated aligned carbon nanofiber based back-gated triode field emission devices and confirmed the operation of these devices. 1-D carbon nanofibers were directly synthesized on blank TiW substrates using direct current plasma enhanced chemical vapor deposition. It was found that the morphology of carbon nanofibers could be tuned from spaghetti-like to aligned by adjusting the applied plasma power. Field emission properties of spaghetti-like and aligned carbon nanofibers on blank TiW substrates were studied using the cartridge holder assembly. Results demonstrated that spaghetti-like carbon nanofibers had better field emission performance than aligned carbon nanofibers, however, the electrostatic simulation of the triode device demonstrated that aligned carbon nanofibers should yield the best device performance.

Second, we have demonstrated that carbon nanosheets, a 2-D carbon nanostructure developed by our group, were a competitive electron emissive material for application as the cold cathode in vacuum microelectronic devices. Carbon nanosheets were synthesized on a variety of substrates, without the need for catalysts, by radio frequency plasma enhanced chemical vapor deposition. Materials characterization results revealed that carbon nanosheets consisting of vertically oriented ultra-thin graphitic sheets terminating with 1-3 graphene layers were hundreds of nanometers in length and height but less than 4 nm in thickness. By using the diode holder assembly, field emission properties of carbon nanosheets were studied from a broad perspective, including turn-on and threshold field, maximum total current, emission lifetime and stability, and emission uniformity. The results revealed that the threshold field of nanosheets ranged from 3.5 to 5.2 V/ $\mu\text{m}$ , which was in the same range as 1-D carbon nanotubes and 3-D diamond. Moreover, the lifetime of nanosheets showed milliamperic current emission (1.5 mA in a dc mode and 13 mA in a slow pulse mode) for hundreds of hours without significant current degradation after the conditioning process. However, the emission uniformity of nanosheets was quite poor due to the existence of "hot runners" during PEEM and FEEM observations. Further, the effectiveness of carbon nanosheet based back-gated triode field emission device was briefly studied.

Third, we have demonstrated that the emission uniformity of nanosheets could be improved by incorporating a thin chromium oxide coating. The chromium oxide coated carbon nanosheets were fabricated by vacuum evaporating thin chromium films on carbon nanosheets and sequentially exposing them to the atmosphere. The stoichiometry of the oxide was estimated to be 0.37, very close to  $\text{Cr}_2\text{O}_3$ . PEEM and FEEM observations showed excellent emission uniformity of chromium oxide coated carbon nanosheets. The field emission properties of chromium oxide coated carbon nanosheets were dependent on the coating thickness. The enhanced field emission performance of chromium oxide coated carbon nanosheets was observed with an appropriate thickness (from 1.5 nm to 15 nm). An explanation for this thickness dependence is suggested.

## TABLE OF CONTENTS

List of Tables .....	v
List of Figures .....	vi
Dedication .....	xiv
Acknowledgements .....	xv
Chapter I Introduction .....	2
1.1 Introduction to vacuum microelectronics .....	2
1.2 Introduction to field emission .....	3
1.3 Introduction to carbon nanostructures .....	8
1.4 Work scope and organization .....	11
Chapter II Materials Characterization Techniques for Carbon Nanostructure Analysis..	15
2.1 Introduction .....	15
2.2 Scanning electron microscopy (SEM) and energy dispersive X-ray spectroscopy (EDX) .....	15
2.3 Raman spectroscopy .....	19
2.4 Auger electron spectroscopy (AES) .....	24
2.5 Photoelectron emission microscopy (PEEM) and field emission electron microscopy (FEEM) .....	26
2.6 Field emission measurement .....	30
2.7 Summary .....	37

Chapter III Field Emission Properties of Carbon Nanofibers .....	39
3.1 Introduction .....	39
3.2 Direct current plasma enhanced chemical vapor deposition (DC PECVD) apparatus .....	41
3.3 Deposition of carbon nanofibers .....	45
3.4 Characterizations of carbon nanofibers .....	47
3.5 Plasma diagnostics .....	53
3.6 Alignment of carbon nanofibers .....	58
3.7 Field emission of CNF on blank TiW substrates .....	59
3.8 Lifetime in a dc mode .....	61
3.9 Field emission of CNF based back gate triode devices .....	63
3.10 Summary .....	65
Chapter IV Field Emission Properties of Carbon Nanosheets .....	68
4.1 Introduction .....	68
4.2 Radio frequency plasma enhanced chemical vapor deposition (RFCVD) apparatus .....	70
4.3 Deposition of carbon nanosheets .....	72
4.4 Characterization of carbon nanosheets .....	73
4.5 Field emission properties of carbon nanosheets .....	78
4.5.1 Turn-on and threshold field .....	79
4.5.2 Total current and current density .....	81
4.5.3 Lifetime in a slow pulse mode .....	83
4.5.4 Lifetime in a dc mode .....	87

4.6 Study on field emission behavior of CNS .....	90
4.7 PEEM and FEEM observation on CNS .....	102
4.8 Field emission of CNS based back gate triode devices .....	106
4.9 Summary .....	109
<b>Chapter V Field Emission Properties of Chromium Oxide Coated Carbon Nanosheets</b>	
(CrO <sub>x</sub> -CNS) .....	115
5.1 Introduction .....	115
5.2 Synthesis of CrO <sub>x</sub> -CNS .....	117
5.3 Characterizations of CrO <sub>x</sub> -CNS .....	118
5.4 PEEM and FEEM observations on CrO <sub>x</sub> -CNS .....	125
5.5 Effects of coating thickness on field emission performance of CrO <sub>x</sub> -CNS .....	134
5.6 Summary .....	138
<b>Chapter VI Summary and Future Work .....</b>	
6.1 Summary .....	142
6.2 Future work .....	146
6.2.1 Study on work function of carbon nanosheets .....	146
6.2.2 PEEM and FEEM measurements on CNS .....	147
6.2.3 Effects of H <sub>2</sub> O on field emission properties of CNS .....	148
6.2.4 Effect of anode and cathode temperature on field emission properties of CNS .....	148
6.2.5 Study on field emission properties of wide-bandgap material coated CNS .....	149
6.2.6 CNS growth parameters optimization .....	150

Vita ..... 152



## LIST OF TABLES

Table 3.1 Summary of emission peaks observed from the pure NH <sub>3</sub> plasma, the pure C <sub>2</sub> H <sub>2</sub> plasma, and the working plasma [21].....	55
Table 4.1 Threshold fields of carbon materials .....	81
Table 4.2 Calculated field enhancement factor $\beta$ , the emission area $A$ , and the effective current density of the emission area $J_{eff}$ from the $F-N$ plots before and after the lifetime time test by substituting the work function into Fowler-Nordheim equation .....	95
Table 5.1 The thickness of CrO <sub>x</sub> coating with regard to various evaporation time .....	125
Table 5.2 Turn-on field and applied electric fields required to generate 1.445 mA emission current of CrO <sub>x</sub> -CNS samples with a variety of coating thicknesses .....	136

## LIST OF FIGURES

Figure 1.1 Diagram of the potential energy of electrons at the surface of a metal [3]. ....	4
Figure 1.2 “Hemisphere on a post” model for the field enhancing effect. ....	6
Figure 1.3 (a) A schematic of C <sub>60</sub> [12], (b) A HRTEM image of a single-walled carbon nanotubes [16], (c) A HRTEM image of a multi-walled carbon nanotubes [17], (d) A HRTEM image of carbon nanofibers [18], (e) A HRTEM image of carbon nanosheets [20]. ....	10
Figure 2.1 Schematic drawing of the electron optics of a SEM [1]. ....	17
Figure 2.2 A picture of Hitachi S-4700 field emission scanning electron microscope used in this work .....	18
Figure 2.3 Atomic displacements for the zone-center optical modes for graphite [4]. ...	22
Figure 2.4 A picture of Renishaw inVia Raman Spectrometer at College of William and Mary. ....	23

Figure 2.5 A schematic of the Auger process [5]. .....	25
Figure 2.6 Diagram of major components of PEEM [7]. .....	28
Figure 2.7 Pictures of applied PEEM systems. (a) A modified Elmitec PEEM III at Ohio University, (b) a modified Staib PEEM at NIST. ....	29
Figure 2.8 A schematic of the automated FE measurement system. ....	31
Figure 2.9 A picture of the automated FE test system. ....	32
Figure 2.10 A schematic of the cartridge holder assembly. ....	33
Figure 2.11 A photograph of the 24 pin header assembly [8]. ....	34
Figure 2.12 (a) The top view schematic of the diode holder assembly, (b) the cross- sectional view schematic of the diode holder assembly, (c) a picture of the diode holder assembly mounted with the copper electric-feedthrough. ....	36
Figure 3.1 Schematics of DC PECVD apparatus. ....	42
Figure 3.2 A picture of the DC PECVD apparatus. ....	43

Figure 3.3 Schematics of blank TiW substrate and back gate triode device. ....	46
Figure 3.4 SEM images of carbon nanofibers synthesized on blank TiW substrates under different plasma powers, (a) 16W, (b) 51W, (c) 72W, (d) 100W. ....	48
Figure 3.5 Average growth rate of CNF as a function of plasma power. ....	49
Figure 3.6 HRTEM image of a representative CNF grown on blank TiW substrate. ....	50
Figure 3.7 Raman spectra of CNF grown on blank TiW substrates with regarding to various plasma powers. ....	51
Figure 3.8 SEM images of spaghetti-like and aligned CNF based back gate triode device before and after post-treatments applied to clean the co-deposited amorphous carbon between two nearest TiW cathode crests. (a) spaghetti-like CNF based back gate triode device before post-treatments, (b) aligned CNF based back gate triode device before post-treatments, (c) spaghetti-like CNF based back gate triode device after post-treatments, (d) aligned CNF based back gate triode device after post-treatments. ....	52
Figure 3.9 Optical emission spectra of (a) pure C <sub>2</sub> H <sub>2</sub> plasma, (b) pure NH <sub>3</sub> plasma, and (c) a typical working plasma used for CNF synthesis on blank TiW substrates. ....	54

Figure 3.10 Intensities of CN violet system, $N_2^+$ first negative system, and $H_\alpha$ line detected from the working plasma as a function of plasma powers. ....	56
Figure 3.11 Emission currents as a function of the applied electric field and corresponding $F-N$ plots (insert). ....	60
Figure 3.12 Emission current of CNF grown on blank TiW substrates as a function of time operated in a dc mode. ....	62
Figure 3.13 $I-V$ characteristics of aligned CNF based back gate device, (a) in a diode mode, (b) in a triode mode. ....	64
Figure 4.1 Schematics of RFCVD apparatus. ....	71
Figure 4.2 A picture of the RFCVD apparatus. ....	73
Figure 4.3 SEM images of representative nanosheets fabricated with the standard CNS deposition conditions. (a) Top-view image, (b) high magnification image, (c) cross-section view image. ....	75
Figure 4.4 (a) TEM image of CNS grown on a grid, (b) HRTEM image of a piece of CNS. ....	76

Figure 4.5 Raman spectrum of a typical CNS sample using a 514 nm excitation laser wavelength. ....	78
Figure 4.6 Turn-on fields of CNS samples as a function of their threshold fields, revealing that the turn-on and threshold field of a typical nanosheet lie in the range from 3 to 4.7 V/ $\mu\text{m}$ and 3.5 to 5.2 V/ $\mu\text{m}$ , respectively. ....	80
Figure 4.7 (a) Field emission current of a CNS sample as a function of the applied electric field, (b) its corresponding $F-N$ plot. ....	84
Figure 4.8 Two consecutive ramps versus time. ....	85
Figure 4.9 Peak current as a function of time in a slow pulse mode. ....	86
Figure 4.10 (a) Field emission currents recorded every ten hours in the stable emission period as a function of the applied electric field, (b) their corresponding $F-N$ plots. ....	88
Figure 4.11 Field emission current as a function of time in dc mode. ....	89
Figure 4.12 (a) $I-V$ curves collected immediately before and after the dc lifetime test together with corresponding calculated $I-V$ curves, (b) their corresponding $F-N$ plots measured and calculated. ....	91

Figure 4.13 2D electrostatic electric field simulation conducted by Maxwell SV at tips of (a) identical emitters, (b) one high hot runner, (c) one thin hot runner. ....	98
Figure 4.14 SEM images of the CNS sample before and after the dc lifetime test. (a) top view image before the dc lifetime test, (b) top view image after the dc lifetime test, (c) cross-section view image before the dc lifetime test, (d) cross-section view image after the dc lifetime test. ....	100
Figure 4.15 Raman spectra of the CNS sample before and after the dc lifetime test. ...	101
Figure 4.16 PEEM and FEEM images captured in the same test area in a typical CNS sample. Only one bright spot is found in the field of view. This bright spot reveals the existence of hot runners in CNS. (a) PEEM image, (b) FEEM image. ....	104
Figure 4.17 Field emission current of the hot runner as a function of the applied electric field. ....	105
Figure 4.18 Emission current of the hot runner as a function of time in a dc mode. ....	106
Figure 4.19 SEM images of CNS based “buried-line” back-gated triode device. (a) top view image, (b) cross-section view image. ....	108
Figure 4.20 Emission current as a function of back gate voltage. ....	109

Figure 5.1 EDX spectra of as-grown and coated CNS samples and their corresponding SEM images of the survey area. (a) as-grown CNS, (b) coated CNS. ....	119
Figure 5.2 Auger spectrum of CrO <sub>x</sub> -CNS. ....	120
Figure 5.3 Raman spectra of CrO <sub>x</sub> -CNS and as-grown CNS. ....	122
Figure 5.4 SEM images of as-grown CNS and CrO <sub>x</sub> -CNS with a variety of evaporation time. (a) T=0 second (as-grown CNS), (b) t=2 seconds, (c) t=5 seconds, (d) t=10 seconds, (e) t=15 seconds. ....	124
Figure 5.5 SEM, PEEM, and FEEM images of patterned CrO <sub>x</sub> -CNS, (a) SEM image, (b) PEEM image, (c) FEEM image. ....	127
Figure 5.6 Collected emission current of patterned CrO <sub>x</sub> -CNS and as-grown CNS as a function of the applied electric field. ....	129
Figure 5.7 PEEM and FEEM images of CrO <sub>x</sub> -CNS with a coating thickness of 1.5 nm. (a) PEEM image taken at 4.34 V/μm as a reference for FEEM images, (b) FEEM image taken at 4.34 V/μm, (c) FEEM image taken at 4.08 V/μm, (d) FEEM image taken at 3.58 V/μm, (e) FEEM image taken at 3.33 V/μm. ....	131



Figure 5.8 Collected emission current of CrO<sub>x</sub>-CNS with a thickness of 1.5 nm as a function of the applied electric field. .... 132

Figure 5.9 *J-V* characteristics of CrO<sub>x</sub>-CNS with a coating thickness of 1.5 nm and 15 nm. .... 133

Figure 5.10 Emission currents of CrO<sub>x</sub>-CNS with a variety of coating thicknesses as a function of the applied electric field. These *I-V* curves show that the best field emission performance is achieved from CrO<sub>x</sub>-CNS with a coating thickness of 1.5 nm. .... 135

Figure 5.11 The band diagram of CrO<sub>x</sub>-CNS with onset of electron emission. Here,  $\Phi_{\text{CNS}}$  is the work function of CNS,  $\chi_{\text{CrO}_x}$  is the electron affinity of CrO<sub>x</sub>, and  $E_g$  is the bandgap of CrO<sub>x</sub>. .... 138

Dedicated to my wife, Minyi, and my parents

## ACKNOWLEDGEMENTS

The author wishes to express his sincere appreciations to Dr. Dennis Manos, Dr. Mark Hinders, and Dr. Brian C. Holloway for their patient advising and valuable criticism throughout this investigation. I am honored to have the opportunity to study under their guidance.

The author is indebted to Dr. Jianjun Wang (Now of Intel. Inc) and Dr. Ron Outlaw for their continuous and unconditioned helps in this study. Their knowledge and experience are invaluable to this work. The author would also like to express a debt of gratitude to Dr. Martin Kordesch in Ohio University for his assistances on PEEM and FEEM study of carbon nanosheets.

The author extends his gratitude to Dr. Jack Kossler for his contributions and service on the oral exam committee.

The author wishes to express his gratitude to the research group members, they are: Dr. Sigen Wang (Now of NCU), Dr. Mingyao Zhu, Dr. Xin Zhao (Now of JLab), Dr. Ben French (Now of Intel. Inc), Dr. Nimel Theodore (Now of ONR), Dr. Shannon Watson (Now of NIST), Peter Miraldo, Ron Quinland, Michael Bagge-Hansen.

**Synthesis and Field Emission Properties of  
Carbon Nanostructures**

# CHAPTER I

## INTRODUCTION

### 1.1 INTRODUCTION TO VACUUM MICROELECTRONICS

Vacuum microelectronics is a rapidly growing research area that utilizes new materials, new microelectronic fabrication techniques, and new approaches in order to achieve record levels of performance and reliability. In contrast to solid state microelectronics, which operate by virtue of electron movement in the lattice of the semiconductor material, vacuum microelectronics relies on the electric field to control electron transport in the vacuum [1]. To date, vacuum microelectronics has become the most important technology for entire classes of high-power, high-frequency amplifiers with the most demanding specifications for use in both military and commercial systems.

The core component of a vacuum microelectronic device is the electron source, also called the cathode, which emits free electrons into the vacuum. Traditional cathodes in these devices are thermionic emitters operated at temperatures between 950°C and 2000°C. Although thermionic emitters are relatively inexpensive, demonstrate high reliability, and provide high current densities, they have a number of significant drawbacks. First, the direct modulation of emitted electrons is rather slow since thermionic emission is controlled via emitter temperature. Second, the energy consumption of thermionic emitters is quite high. Third, the miniaturization of devices equipped with thermionic emitters is almost impossible because of the high heat load.

Currently, field emission emitters are considered a better choice to use as the electron source in vacuum microelectronic devices because of their high emission current density (up to  $10^7$  A/cm<sup>2</sup> at the emission site), low energy spread of emitted electrons (less than 500 meV), and simultaneous device response [2]. Since field emission electron sources do not require thermal excitation, they can significantly reduce energy consumption and increase the lifetime of vacuum microelectronic devices. Moreover, the capability of field emission electron sources fabricated to submicrometer scales results in the development of very small vacuum microelectronic devices.

## 1.2 INTRODUCTION TO FIELD EMISSION

Field emission is a process by which electrons are extracted from a solid material into the vacuum by an intense electric field ( $10^7$ - $10^8$  V/cm). It is a quantum-mechanical phenomenon in which electrons tunnel through a potential barrier at the surface of a solid, as a result of the electric field. The external electric field lowers the surface barrier that confines the electrons within the solid so that the barrier becomes nearly triangular in shape. As the width of the surface potential barrier at the Fermi energy approaches 2 nm, electrons will have a significant probability to tunnel from the highest occupied states of the solid into the vacuum. A diagram of the potential energy of electrons at the surface of a solid is presented in Figure 1.1 [3].

In 1928, Fowler and Nordheim proposed the first widely accepted theory to explain field emission from a planar metal cathode [4]. Their theory is based on the following assumptions: (1) The metal obeys the Sommerfeld free electron model; (2) The metal surface is planar. Therefore, only one-dimensional problem is considered; (3) The

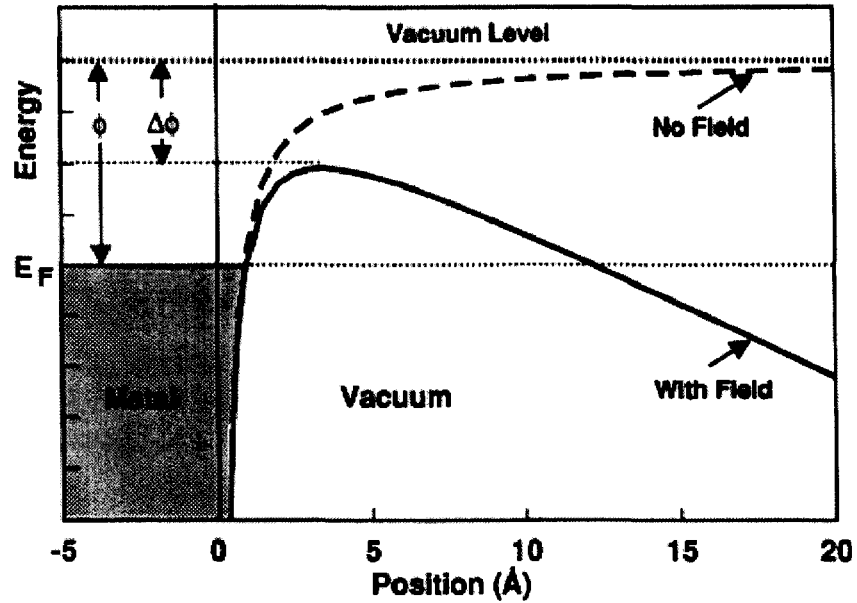


Figure 1.1 Diagram of the potential energy of electrons at the surface of a metal [3].

potential within the metal is treated as constant, while the potential outside the metal changes with regard to the image force and the externally applied electric field. The externally applied electric field does not penetrate the metal, and therefore has no effect on the electron state inside the metal; (4) The calculation is performed assuming the Fermi-Dirac electron distribution in the solid remains at  $T=0$  K.

Under these assumptions, the current density ( $J$ ) is given by integrating the product of the transport probability function of an electron with a given energy tunneling through the potential barrier and the electron supply function in the available range of electron energies, as given by [5]

$$J = e \int_0^{\infty} n(E_x) D(E_x, F) dE_x, \quad (1.1)$$

where  $n(E_x)$  is the supply function in the form of [6]

$$n(E_x) = 4\pi mkTh^{-3} \ln\{1 + \exp[-(E_x - E_F)/kT]\} , \quad (1.2)$$

and  $D(E_x, F)$  is the transport probability function presented as [5]

$$D(E_x, F) = \exp\left[-\frac{8\pi(2m)^{1/2}}{3he}\right] \frac{|E_x|^{3/2}}{F} \vartheta(y) . \quad (1.3)$$

where,  $m$  is the electron mass,  $T$  is the absolute temperature,  $E_x$  is the electron kinetic energy normal to the metal surface,  $\varphi$  is the work function of the metal,  $F$  is the externally applied electric field, and  $\vartheta(y)$  is the Nordheim (elliptic) function. The Nordheim function has an expression of

$$\vartheta(y) = \frac{1}{\sqrt{2}} [1 + (1 - y^2)^{1/2}]^{1/2} \cdot [E(k) - \{1 - (1 - y^2)^{1/2}\}K(k)] , \quad (1.4)$$

where

$$y = \frac{(e^3 F)^{1/2}}{\varphi} , \quad (1.5)$$

and

$$E(k) = \int_0^{\pi/2} \frac{d\alpha}{(1 - k^2 \sin^2 \alpha)^{1/2}} , \quad K(k) = \int_0^{\pi/2} (1 - k^2 \sin^2 \alpha)^{1/2} d\alpha . \quad (1.6)$$

Substituting (1.2) and (1.3) into (1.1) and integrating (1.1) give

$$J = \frac{e^3}{4(2\pi)^2 t^2(y) \hbar \Phi} F^2 \exp\left(-\frac{4\sqrt{2m_e}}{3\hbar e F} \Phi^{1.5} \vartheta(y)\right) , \quad (1.7)$$

where  $t(y) = \vartheta(y) - (2y/3)(d\vartheta(y)/dy)$ ,  $\Phi$  is the work function of the metal, and  $F$  is the external electric field. This general expression is called the Fowler-Nordheim equation.

Even though the Fowler-Nordheim equation has been widely used to study field emission performance of emissive materials, the validation of the equation is strictly limited to perfect conductors that have flat surfaces and are held at  $T=0$  K. Therefore,



efforts that aim to apply the equation to practical surfaces have to extend the equation to a range of applications far beyond the assumptions used to derive it.

In theory, a high external electric field, on the order of  $3000 \text{ V}/\mu\text{m}$ , would be required to achieve detectable field emission current. Such a high electric field is very difficult to generate on flat surfaces, but it can be generated by the field enhancing effect of a sharp tip-like structure. If a tip-like structure is exposed to an electric field  $F_0$ , the local electric field  $F$  at the tip apex is higher by a multiplication factor of  $\beta$ . In the case of carbon nanostructures, the most geometrically realistic model of this field enhancing effect is a “hemisphere on a post” model, as shown in Fig. 1.2. In this model, a post of

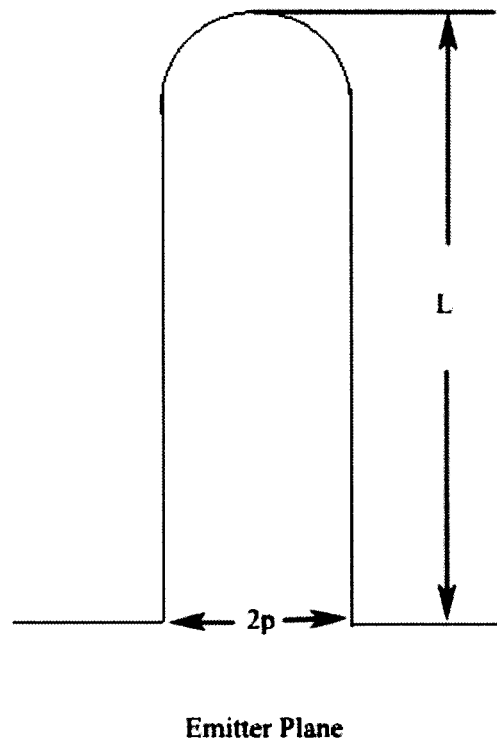


Figure 1.2 “Hemisphere on a post” model for the field enhancing effect.

height  $L$  capped by a hemispherical tip is located on a larger emitter plane. The potential of the post is equal to that of the emitter plane. Forbes et al[7] calculated the field enhancement factor of this model using conventional finite-element analysis of the field and potentials. For  $L/p$  in the range from 4 to 3000, the field enhancement factor  $\beta$  can be represented as

$$\beta \cong 1.2(2.15 + \frac{L}{p})^{0.9}. \quad (1.8)$$

For  $L/p > 3000$ , the field enhancement factor can be approximately expressed as

$$\beta = \frac{L}{p}. \quad (1.9)$$

In the case of thin film emitters where a multiplicity of closely-spaced emitters may exist, the field enhancement factor of a given emitter is significantly decreased in comparison to the value calculated by this model, due to a screening effect to be described later in this thesis.

When the aspect ratio  $L/P$  exceed a thousand, the required electric field of 3000 V/ $\mu\text{m}$  for electron field emission will occur at the apex of the tip at actual fields as low as a few volts per micron.

A field emission electron source of this sort was developed by Spindt and his co-workers in 1968 [8]. Spindt-type field emission sources are arrays of thousands or even millions of metal cones with sub-micron tip radii formed on silicon substrates using conventional lithographic patterning techniques. By placing an electrode a few microns away from the emitters, electrons can be extracted at very low applied voltages.

Unfortunately, Spindt-type arrays have drawbacks that have made them unreliable for vacuum microelectronic devices. A catastrophic failure of a single tip often destroys the

whole Spindt-type arrays. Also, Spindt-type field emission arrays suffer from high manufacturing costs and limited lifetime even in the absence of catastrophic failures.

Consequently, there is a strong incentive to simplify both the production and design of the cathode in vacuum microelectronic devices by replacing Spindt-type field emission arrays with carbon nanostructure based thin film emitters. Carbon nanostructures have the right combination of properties to make them excellent electron emitters: nanometer-size tips, high electrical and thermal conductivity, chemical stability, and potentially low manufacturing costs [9].

### 1.3 INTRODUCTION TO CARBON NANOSTRUCTURES

Carbon nanostructures are material forms composed of carbon atoms, which have at least one dimension less than 100 nm [10]. Depending on the morphology, a carbon nanostructure is said to be zero-dimensional (0-D), one-dimensional (1-D), or two-dimensional (2-D) nanostructure when it has one or more of its dimension less than a hundred nanometers. Conventional forms of carbon, like graphite or diamond, are generally referred to as “bulk” material.

Fullerenes are well-known 0-D carbon nanostructures. Fullerenes were first discovered and developed by Smalley and co-workers at Rice University in 1985 [11]. A fullerene is a geometric cage-like structure of carbon atoms composed of hexagonal and pentagonal faces. The first fullerene discovered was the  $C_{60}$  molecule, a closed cage of 60 carbon atoms where each side of a pentagon is adjacent to one side of a hexagon. This pattern is similar to a soccer ball. An image of  $C_{60}$  is illustrated in Figure 1.3(a) [12].

Carbon nanofibers (CNF) and carbon nanotubes (CNT) are 1-D carbon

nanostructures. The earliest reference to carbon fibers is an 1889 patent by Hughes and Chambers describing the growth of “hair-like carbon filaments” from carbon-containing gases in an iron crucible [13]. The existence of carbon nanotubes in materials engineering can be traced back to the seventeenth century with the application as a strengthening component in Damascus blades [14]. However, it was not until 1991 that Iijima first imaged carbon nanotubes using high-resolution transmission electron microscopy [15]. Carbon nanotubes exist in two classes: single-walled and multi-walled. Single-walled nanotubes consist of one graphene sheet rolled up in the form of a cylinder with a diameter of 1 to 2 nm. Multi-walled nanotubes are formed from arrays of single-walled nanotubes that are concentrically nested like rings of a tree trunk. Images of single-walled and multi-walled nanotubes are shown in Figure 1.3(b) and 1.3(c), respectively [16, 17]. Carbon nanofibers differ from nanotubes in the orientation of their graphene layers with respect to the cylinder axis. A nanofiber has an orientation angle between its graphene layers and its axis, while a nanotube has graphene layers parallel to its axis. An image of carbon nanofibers is displayed in Figure 1.3(d) [18].

Carbon nanosheets, consisting of 1-3 graphene layers, are 2-D carbon nanostructures. Even though 2-D carbon nanostructures have been used in theoretical calculations for graphite related materials for years, it was in the 1990s that petal-like graphitic sheets were first discovered by Ando et al [19]. Our group, together with others, first reported the existence of self-assembled multilayer graphitic sheets with thickness less than 1 nm [20-28]. These carbon nanosheets consist of 1-7 graphene layers, which are usually hundreds of nanometers in height and length but only ~1-2 nanometer in thickness. During growth, nanosheets may be composed of several graphene layers, but often

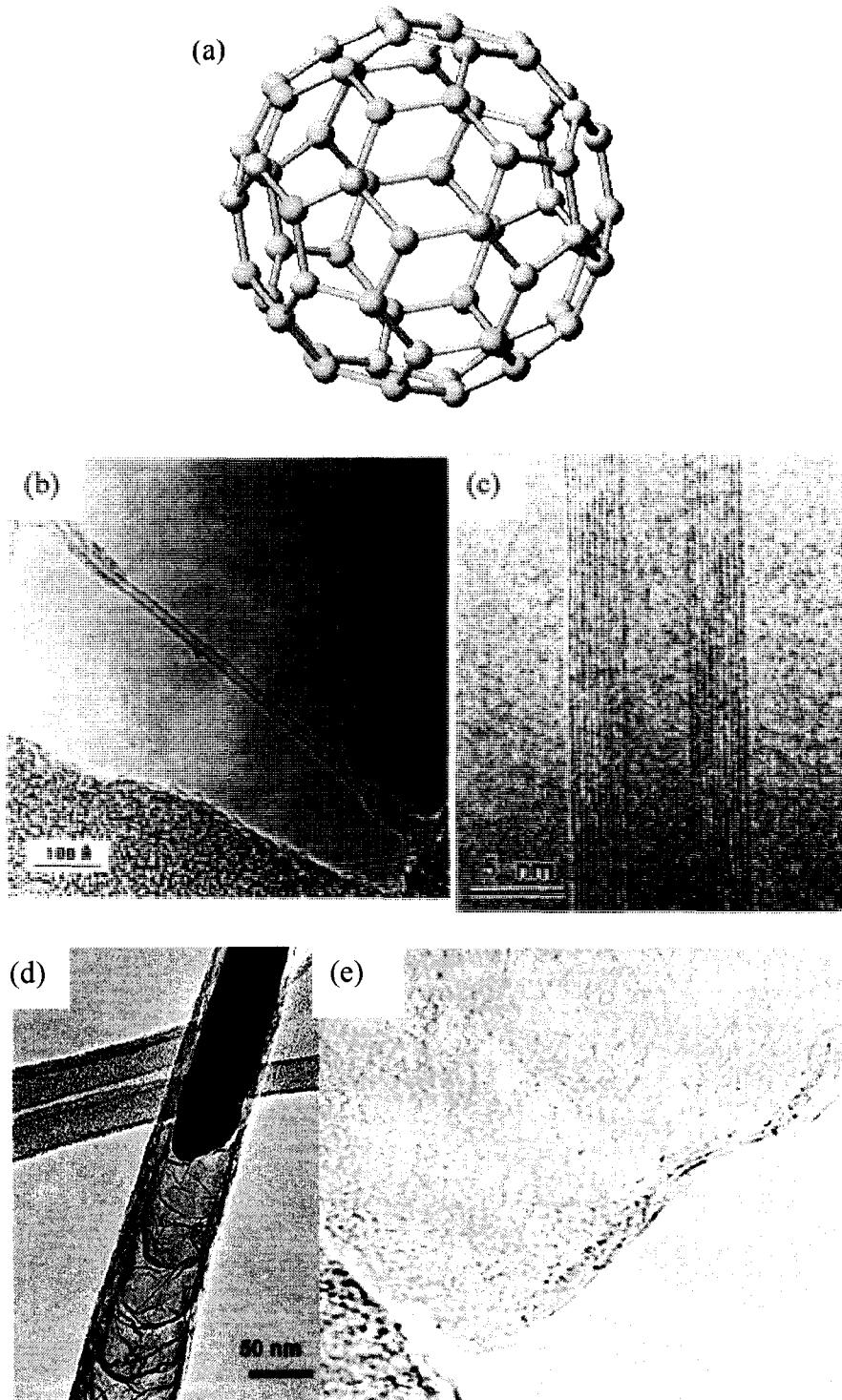


Figure 1.3 (a) A schematic of C<sub>60</sub>[12], (b) A HRTEM image of a single-walled carbon nanotubes[16], (c) A HRTEM image of a multi-walled carbon nanotubes[17], (d) A HRTEM image of carbon nanofibers[18], (e) A HRTEM image of carbon nanosheets[20].

grow and terminate as 1-2 nanosheets. An image of carbon nanosheets is shown in Figure 1.3(e) [20].

#### 1.4 WORK SCOPE AND ORGANIZATION

This dissertation focuses on field emission performances of selected carbon nanostructure thin films to develop a novel high brightness electron source for the application in vacuum microelectronic devices. This application requires that the electron source has greater than 10 mA total emission current and stable emission for hundreds of hours. To achieve these requirements, the synthesis, material characterization, and field emission properties of carbon nanostructures-including 1-D carbon nanofibers and 2-D carbon nanosheets-are studied in this work.

Chapter II briefly introduces the materials characterization apparatus used for carbon nanostructure analysis and the operational principles of these apparatus, including scanning electron microscopy (SEM), Raman spectroscopy (Raman), Auger electron spectroscopy (AES), energy dispersive X-ray spectroscopy (EDX), photoelectron emission microscopy (PEEM), field emission electron microscopy (FEEM), and field emission (FE) test system.

Chapter III outlines the synthesis, structure, and field emission properties of 1-D carbon nanofibers directly deposited on blank TiW substrates by direct current plasma enhanced chemical vapor deposition (DC PECVD) together with the field emission performance of nanofiber based back-gated triode devices.

Chapter IV presents the synthesis, structure, and field emission properties of 2-D carbon nanosheets grown on Si substrates by radio frequency plasma enhanced chemical

vapor deposition (RFCVD) and the field emission performance of nanosheet based back-gated triode devices. The turn-on field, maximum total current, emission stability and lifetime, and emission uniformity of carbon nanosheets are discussed in detail.

Chapter V demonstrates the synthesis, structure, and field emission properties of chromium oxide coated carbon nanosheets fabricated by vacuum evaporation of a thin chromium layer on nanosheets and subsequently exposing to the atmosphere.

Chapter VI summarizes the overall work of this dissertation and suggests future research directions for developing carbon nanostructure based high brightness electron source for the application in vacuum electronic devices.

## References for Chapter I:

- [1] Groning O, Kuttel OM, Emmenegger C, Groning P, Schlapbach L. Field emission properties of carbon nanotubes. *Journal of Vacuum Science & Technology B: Microelectronics and Nanometer Structures*. 2000;18(2):665-78.
- [2] Baptist R, Ghis A, Meyer R. *Second International Conference on Vacuum Microelectronics*; 1989; Bath, UK.
- [3] Temple D. Recent progress in field emitter array development for high performance applications. *Materials Science and Engineering: R: Reports*. 1999;24(5):185-239.
- [4] Fowler RH, Nordheim LW. *Proc R Soc London, Ser A*; 1928:119-73.
- [5] Fursey G. *Field Emission in Vacuum Microelectronics*: Kluwer Academic/Plenum Publishers 2005.
- [6] Murphy EL, Good RH. Thermionic Emission, Field Emission, and the Transition Region. *Physical Review*. 1956;102(6):1464.
- [7] Forbes RG, Edgcombe CJ, Valdre U. Some comments on models for field enhancement. *Ultramicroscopy*. 2003;95:57-65.
- [8] Spindt CA. A Thin-Film Field-Emission Cathode. *Journal of applied physics*. 1968;39:3504-5.
- [9] Dresselhaus MS, Dresselhaus G, Avouris P. *Carbon Nanotubes: Synthesis, Structure, Properties, and Applications*. Heidelberg: Springer 2000.
- [10] Koch CC. *Nanostructured Materials*: Noyes Publications 2002.
- [11] Kroto HW, Heath JR, O'Brien SC, Curl RF, Smalley RE. C60: Buckminsterfullerene. *Nature*. 1985;318(6042):162-3.
- [12] <http://www.sussex.ac.uk/users/kroto/fullerencenter/banner1.html>, 2007.
- [13] Hughes TV, Chambers CR, inventors; *Manufacture of Carbon Filaments*. US. 1889.
- [14] Reibold M, Paufler P, Levin AA, Kochmann W, Patzke N, Meyer DC. *Materials: Carbon nanotubes in an ancient Damascus sabre*. *Nature*. 2006;444(7117):286.
- [15] Iijima S. Helical microtubules of graphitic carbon. *Nature*. 1991;354(6348):56-8.
- [16] Bethune DS, Klang CH, de Vries MS, Gorman G, Savoy R, Vazquez J, Beyers R. Cobalt-catalysed growth of carbon nanotubes with single-atomic-layer walls. *Nature*. 1993;363(6430):605-7.
- [17] Baughman RH, Zakhidov AA, de Heer WA. *Carbon Nanotubes--the Route Toward Applications*. *Science*. 2002;297(5582):787-92.
- [18] Melechko AV, Merkulov VI, McKnight TE, Guillorn MA, Klein KL, Lowndes DH, Simpson ML. Vertically aligned carbon nanofibers and related structures: Controlled synthesis and directed assembly. *Journal of Applied Physics*. 2005;97(4):041301-39.
- [19] Ando Y, Zhao X, Ohkohchi M. Production of petal-like graphite sheets by hydrogen arc discharge. *Carbon*. 1997;35(1):153-8.
- [20] Wang JJ, Zhu MY, Outlaw RA, Zhao X, Manos DM, Holloway BC, Mammana VP. Free-standing subnanometer graphite sheets. *Applied Physics Letters*. 2004;85(7):1265-7.
- [21] Zhu M, Wang J, Outlaw RA, Hou K, Manos DM, Holloway BC. Synthesis of carbon nanosheets and carbon nanotubes by radio frequency plasma enhanced chemical vapor deposition. *Diamond and Related Materials*. 2007;16(2):196-201.



- [22] Wang S, Wang J, Miraldo P, Zhu M, Outlaw R, Hou K, Zhao X, Holloway BC, Manos D, Talmage T, Shenderova O, Mark R, Dalton J, McGuire G. High field emission reproducibility and stability of carbon nanosheets and nanosheet-based backgated triode emission devices. *Applied Physics Letters*. 2006;89(18):183103-3.
- [23] Wang J, Zhu M, Zhao X, Outlaw RA, Manos DM, Holloway BC, Park C, Anderson T, Mammana VP. Synthesis and field-emission testing of carbon nanoflake edge emitters. *Journal of Vacuum Science & Technology B: Microelectronics and Nanometer Structures*. 2004;22(3):1269-72.
- [24] Wang J, Zhu M, Outlaw RA, Zhao X, Manos DM, Holloway BC. Synthesis of carbon nanosheets by inductively coupled radio-frequency plasma enhanced chemical vapor deposition. *Carbon*. 2004;42(14):2867-72.
- [25] Novoselov KS, Geim AK, Morozov SV, Jiang D, Zhang Y, Dubonos SV, Grigorieva IV, Firsov AA. Electric Field Effect in Atomically Thin Carbon Films. *Science*. 2004;306(5696):666-9.
- [26] Novoselov KS, Geim AK, Morozov SV, Jiang D, Katsnelson MI, Grigorieva IV, Dubonos SV, Firsov AA. Two-dimensional gas of massless Dirac fermions in graphene. *Nature*. 2005;438(7065):197-200.
- [27] Berger C, Song ZM, Li TB, Li XB, Ogbazghi AY, Feng R, Dai ZT, Marchenkov AN, Conrad EH, First PN, de Heer WA. Ultrathin epitaxial graphite: 2D electron gas properties and a route toward graphene-based nanoelectronics. *Journal of Physical Chemistry B*. 2004;108(52):19912-6.
- [28] Berger C, Song Z, Li X, Wu X, Brown N, Naud C, Mayou D, Li T, Hass J, Marchenkov AN, Conrad EH, First PN, de Heer WA. Electronic Confinement and Coherence in Patterned Epitaxial Graphene. *Science*. 2006;312(5777):1191-6.

CHAPTER II  
MATERIALS CHARACTERIZATION TECHNIQUES FOR CARBON  
NANOSTRUCTURE ANALYSIS

## 2.1 INTRODUCTION

The carbon nanostructures of interest in this work are only nanometers in dimensions; thus they can not be observed by optical microscopy. Therefore, a variety of materials characterization techniques have been applied to investigate the field emission properties of carbon nanostructures with respect to their morphologies, microstructures, and components. These techniques include scanning electron microscopy (SEM), Energy dispersive X-ray spectroscopy (EDX), Raman spectroscopy (Raman), Auger electron spectroscopy (AES), photoelectron emission microscopy (PEEM), field emission electron microscopy (FEEM), and field emission (FE) measurement, etc. In this chapter, a brief introduction to the materials characterization techniques used for carbon nanostructure analysis and their operational principles is presented.

## 2.2 SCANNING ELECTRON MICROSCOPY (SEM) AND ENERGY DISPERSIVE X-RAY SPECTROSCOPY (EDX)

Scanning electron microscopy is one of the most widely used imaging techniques in material surface analysis because of its high magnification and high resolution. A scanning electron microscope (SEM) uses electrons as the light source and collects

ejected electrons from the specimen surface for imaging. The microscope takes advantage of the short wavelength of the electron to achieve high spatial resolution of the specimen surface. A state-of-the-art SEM has a spatial resolution of 0.4 nm at an accelerating voltage of 30 KV.

Beam electrons of SEM are either generated via field emission or thermal emission from the cathode material that is usually tungsten or lanthanum hexaboride ( $\text{LaB}_6$ ). Electrons are then accelerated toward the anode and tuned to a focused electron beam, with a diameter on the order of nanometers, through a series of electromagnetic lenses. The deflection coil connected to a scan generator makes the primary electron beam raster across the specimen surface. Therefore, the magnification of SEM is achieved by variation of the length of the primary beam scan as a function of the length displayed on the viewing screen.

When the electron beam strikes the surface of the specimen, it produces two separate groups of “reflected” electron that can be used for imaging: backscattered electrons and secondary electrons. Backscattered electrons with energies similar to the primary electrons originate from the elastic scattering of the beam electrons in the specimen. They are used to form images to provide direct information on compositional heterogeneity of the sample surface. Secondary electrons, ejected from the specimen during the inelastic scattering of beam electrons in the 5-50 nm outermost layer of the specimen, have energies in the range of 0 to 50 eV. Secondary electrons are commonly used for surface topography imaging. All SEM images presented in this work are generated from secondary electrons ejected from the specimen.

An SEM can be subdivided into several component systems that perform various

functions, including electron optical and beam control systems, sample manipulation system, vacuum system, electron detector, signal processing, and recording systems. A schematic drawing of the electron optics of a SEM is displayed in Figure 2.1.

An SEM can only precisely image conducting solid specimens. Nonconducting specimens require some pre-treatments to eliminate or reduce the electric charge build-up for SEM imaging when a nonconductor is scanned by the primary electron beam. Normally, a thin conformal layer (several nanometers in thickness) of conducting

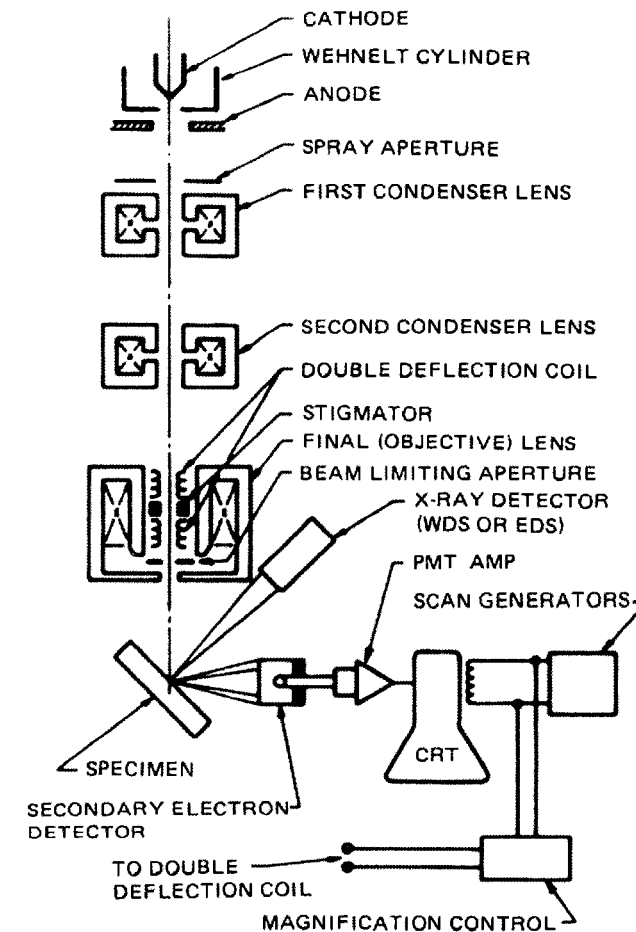


Figure 2.1 Schematic drawing of the electron optics of a SEM [1].

materials such as Au and C is deposited on nonconducting specimens to suppress the charge build-up.

A Hitachi S-4700 field emission SEM was used in this work to conduct most of studies. A picture of this S-4700 SEM is displayed in Figure 2.2. The magnification of this microscope ranges from 20 to 500K at an accelerating voltage of 15 KV, yielding a spatial resolution of  $\sim 1.5$  nm at a working distance of 12 mm.

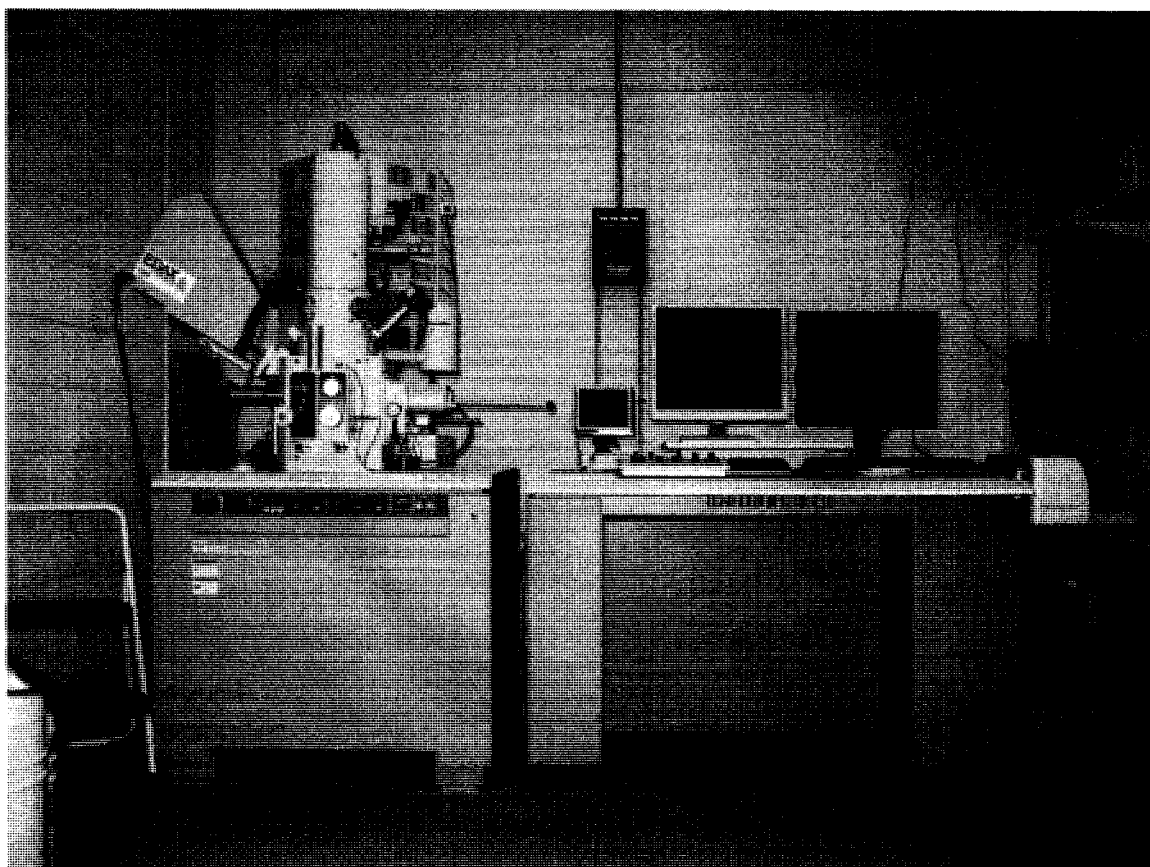


Figure 2.2 A picture of Hitachi S-4700 field emission scanning electron microscope used in this work.

In addition to secondary electrons and backscattered electrons, characteristic X-rays can also be ejected from the specimen when a high energy (15-30KV) electron beam of SEM strikes a specimen surface. When beam electrons collide with the inner shell electrons of specimen atoms, they eject some of these inner shell electrons. The vacancy generated in the inner shell is eventually occupied by a high energy electron from an outer shell. During this process, the outer shell electron can release its excess energy by emitting an X-ray. The X-rays have kinetic energies highly specific to individual elements. These characteristic X-rays are detected by energy dispersive X-ray spectroscopy (EDX), which allows identification of the elemental composition of the specimen. The characteristic X-rays are generated in a region about 2  $\mu\text{m}$  in depth, so EDX measures a very thick layer relative to the thickness of our CNS thin film.

The EDX spectroscopy used in this work is an EDX PV 7746/61 with an energy resolution of  $\sim 2.5$  eV, which can be seen at the top left (labeled EDX) in Fig. 2.2.

### 2.3 RAMAN SPECTROSCOPY

Raman spectroscopy can provide information of the vibrational frequencies of solid materials that depend on the mass of atoms, the strength of interatomic bonds, and the geometrical arrangement of atoms in the crystal structure. Raman spectroscopy is a conventional material characterization technique used to analyze the microstructure of carbon materials.

Raman scattering, first discovered by Raman in 1928 [2], occurs during the interaction between the incident light and the specimen. Raman scattering is a two-photon process that involves the simultaneous absorption of an incident photon and the

emission of a secondary photon. If the frequency of the secondary photon,  $\omega_s$ , is smaller than that of the incident photon,  $\omega_L$ , a quantum of energy  $\hbar(\omega_L - \omega_s)$  is added to the medium and the event is referred to as a Stokes process. If  $\omega_s > \omega_L$ , an elementary excitation of the medium is annihilated and this event is called as anti-Stokes process. Raman scattering, as an inelastic scattering process, satisfies the conservation of momentum. Therefore, the momentum conservation for Raman scattering can be written as

$$\mathbf{k}_L - \mathbf{k}_S = \sum_j \mathbf{q}_j, \quad (2.1)$$

where  $\mathbf{k}_L$  is the incident wave vector,  $\mathbf{k}_S$  is the scattering wave vector, and  $\mathbf{q}_j$  is the individual wave vector ranging from zero to the values at the Brillouin zone boundary. In the first-order process, only a single quantum of excitation in the medium participates. Therefore, their Raman spectra display a discrete set of peaks that are associated with elementary (single-quantum) excitations at the center of the Brillouin zone. However, higher-order (multi-quantum) Raman spectra give continua consisting of wave vectors that span the whole Brillouin zone of the crystal and correlate to structure in the density of states of representative modes.

Raman scattering can be studied by analyzing the induced polarization  $\mathbf{P}$  in the scattering medium that oscillates at the frequency  $\omega_s$ . The polarization is expressed as

$$\mathbf{P}_i(\omega_s) = \sum_j \delta_{\chi_{ij}} E_j(\omega_L), \quad (2.2)$$

where  $E(\omega_L)$  is the electric field of the incident beam and  $\delta_{\chi_{ij}}$  is the modulated Raman susceptibility. This Raman susceptibility is a second-rank tensor with non-zero components determined by the symmetries of the scattering medium and of the

elementary excitations. The displacement of an atom in the unit cell at  $\mathbf{r}$  is written as

$$\mathbf{U}_s(\mathbf{r}, t) \propto Q_m(\omega, \mathbf{q}) e^{i(\mathbf{q} \cdot \mathbf{r} - \omega t)}, \quad (2.3)$$

where  $Q_m(\omega, \mathbf{q})$  is the phonon coordinate or the amplitude of the mode of frequency  $\omega$  and wave vector  $\mathbf{q}$  belonging to the  $m$ th-branch. For a small amplitude, the modulated Raman susceptibility  $\delta\chi_{ij}$  can be expanded as a function of  $Q_m$ , written as

$$\delta\chi_{ij} = \sum_m R_{ij}^{(m)} Q_m(0) + \sum_{mn, \mathbf{q}\mathbf{p}} R_{ij}^{(mn)} Q_m(\mathbf{q}) Q_n(\mathbf{p}) + \dots \quad (2.4)$$

Here,  $R_{ij}^{(m)}$  and  $R_{ij}^{(mn)}$  are first-order and second-order Raman tensor, respectively. If the first term in the right hand side does not vanish for a particular mode, this mode is said to be Raman active.

When incident laser photons or scattered laser photons have the same kinetic energies as the energy separation between two electronic energy states, resonance Raman (RR) scattering occurs. The resonance Raman scattering can enhance the intensities of a Raman mode by a factor of  $10^3$  to  $10^5$ .

Under ambient condition, the crystalline structure of graphite belongs to  $D_{6h}^4$  hexagonal space group. Therefore, the Brillouin zone-center optical phonon modes for 3D graphite can be represented by the following combination of irreducible representations [3]

$$\Gamma_{opt} \rightarrow 2E_{2g} + E_{1u} + A_{2u} + 2B_{1g}, \quad (2.5)$$

which are first-order Raman scatterings. Among these irreducible representations, only the doubly degenerate  $E_{2g}$  mode is Raman active. The corresponding atomic displacement for  $E_{2g}$  mode is displayed in Fig. 2.3. The  $E_{2g_1}$  mode occurs at  $42 \text{ cm}^{-1}$  and is usually not present in the spectrum. The  $E_{2g_2}$  mode at  $1582 \text{ cm}^{-1}$ , the so-called G band, is the most



prominent feature in the Raman spectrum of graphite.

Since impurities and defects break the translation symmetry of the crystal in the host material, they can lead to scattering by phonons that have wave vectors far away from the zone center. In the case of graphite, a so-called disorder induced band, D band, appears at  $1350\text{ cm}^{-1}$  for a laser excitation wavelength of  $488\text{ nm}$ . The D band represents a second-order Raman scattering consisting of one-phonon and one-elastic event. Since the laser excitation wavelength can alter the phonon frequencies, the frequency of D band changes by  $53\text{ cm}^{-1}$  corresponding to a change of the laser energy by  $1\text{ eV}$ . The so-called G' band is also a second-order Raman scattering that mixes  $\mathbf{q}$  and  $-\mathbf{q}$  scattering wave vectors. Since the G' band is located at  $2700\text{ cm}^{-1}$ , almost twice frequency of the D band, the G' band can also be thought as a harmonic overtone of D mode.

In addition, a small disorder induced feature, the so-called D' band, is sometimes observed at  $1620\text{ cm}^{-1}$ . This feature originates from the high phonon density of states near the maximum optic phonon frequency, which is forbidden under defect-free conditions.

A Raman spectrometer commonly consists of four major components, including

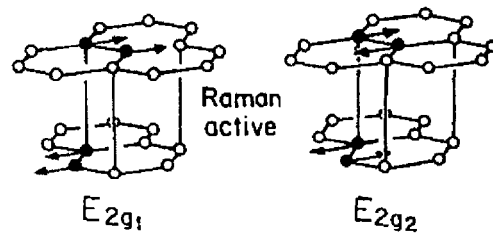


Figure 2.3 Atomic displacements for the zone-center optical modes for graphite [4].

excitation source, sample illumination and collection system, wavelength selector and detection system, and computer control/processing system.

In this work, all spectra were collected using a Renishaw inVia Raman Microscope equipped with four wavelength excitation sources, including Ar<sup>+</sup> laser (488 and 514 nm), He-Ne laser (633 nm), and NIR laser (785 nm). A picture of this spectrometer is shown in Figure 2.4.

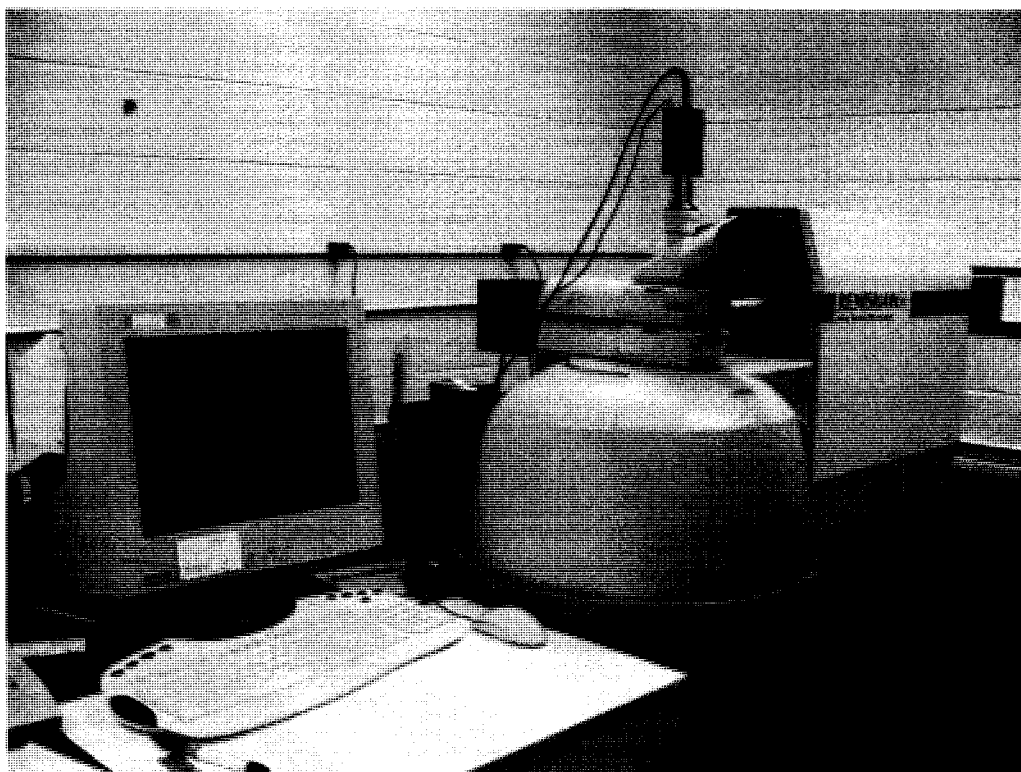


Figure 2.4 A picture of Renishaw inVia Raman Spectrometer  
at College of William and Mary.

## 2.4 AUGER ELECTRON SPECTROSCOPY (AES)

Auger electron spectroscopy (AES) is a widely used chemical analysis technique of the solid surface. This spectroscopy employs a primary electron beam with typical energies between 3 and 30 keV to focus and scan across the top-most atomic layers of a conducting sample. Emitted Auger electrons with energy characteristics of the surface atom are generated by electron bombardment in a process similar to that producing X-rays for EDX.

Figure 2.5 displays a schematic of the Auger process. When a primary electron beam with sufficient kinetic energy impinges a solid surface, a core level W (i.e. K, L, ...) electron of a surface atom with energy of  $E_w$  is ionized and leaves a hole there. This empty position can be filled by an electron from a higher energy level  $E_x$ . The transition of the electron between levels W and X releases an energy corresponding to  $\Delta E = E_w - E_x$  that excites a third electron of the same atom at energy level  $E_y$ . This third electron is called an Auger electron. The kinetic energy of the Auger electron is the difference of energy between three electronic levels involved minus the work function of the solid sample

$$E_{wxy} = E_w - E_x - E_y - \Phi . \quad (2.6)$$

As a result, the kinetic energy of the Auger electron characterizes the emitting element of the solid surface.

The Auger peaks are usually small and are superimposed on a slowly-varying energy distribution spectrum of secondary electrons that is much higher in intensity, which makes them hard to distinguish. Therefore, the spectrum is differentiated to enhance the peak features enabling detection of subtle differences and fine structure of

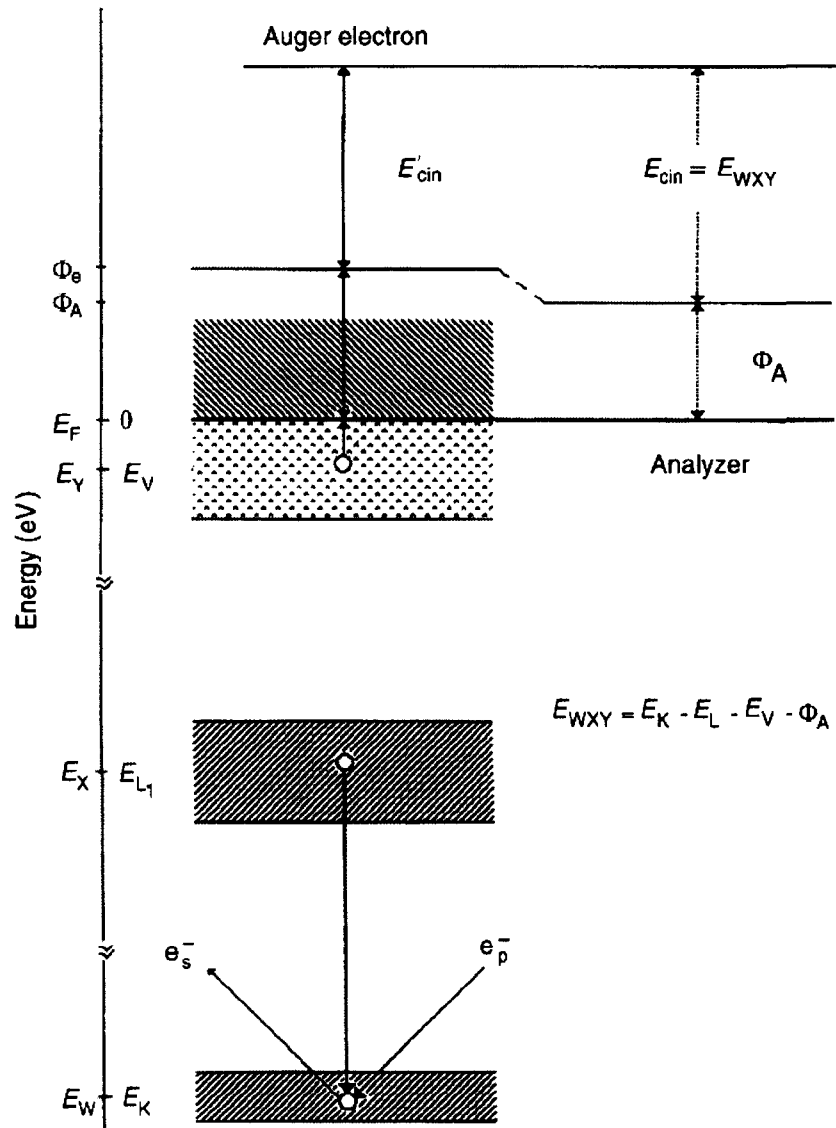


Figure 2.5 A schematic of the Auger process [5].

the spectrum. Therefore, the normal representation of Auger spectra is  $\frac{dN(E)}{d(E)}$  against  $E$ .

Auger peaks of light elements are often more easily identified than those of heavier elements because a large number of transitions of heavier elements often overlap with those of other atoms.

An Auger electron spectrometer usually consists of five components, including electron source, electrostatic energy analyzer, sample manipulating system, ultra-high vacuum chamber, and data collecting system.

A Physical Electronic 590 surface analysis system was used to collect Auger spectra in this work, which has a base pressure of  $\sim 1 \times 10^{-11}$  Torr. The electron gun of the system can provide a 5 kV/50  $\mu$ A electron beam with a minimum beam spot size of 25  $\mu$ m. A double pass cylindrical mirror analyzer (DP CMA) is employed to measure the kinetic energy of Auger electrons. More information about the system can be found elsewhere [6].

## 2.5 PHOTOELECTRON EMISSION MICROSCOPY (PEEM) AND FIELD EMISSION ELECTRON MICROSCOPY (FEEM)

Photoelectron emission microscopy (PEEM) is a non-destructive surface microscopic imaging technique that uses photons for illumination. Without the photon source, PEEM can be deployed as a field emission electron microscope (FEEM) to investigate the field emission property of the specimen.

PEEM uses both photoelectrons and field emission electrons ejected from the specimen surface for imaging. When photons with kinetic energy larger than the work function of the specimen strike the surface of the specimen, photoelectrons can be

emitted from the specimen surface with a kinetic energy, usually on the order of several eVs, defined by

$$E_k = h\nu - \Phi \quad (2.9)$$

where  $\Phi$  is the work function of the specimen. To the extent that  $\Phi$  varies with topography and surface composition, these low energy photoelectrons provide local topographical information about the specimen surface and compositional surface sensitivity of PEEM observations. An accelerating electric field on the order of several V/ $\mu\text{m}$  is applied between the specimen mounted in the cathode lens and the first objective lens (the extractor) to collect low energy photoelectrons for imaging. Therefore, field emission electrons escaping from the surface are captured by the microscope to form surface images. These field emission electrons give information about emission sites in the form of a single spot or clusters of bright spots. Even though PEEM images both photoelectrons and field emission electrons simultaneously using the same electron optics, photoelectrons can be made to dominate the image by lowering the extraction field to values near (or below) the field emission threshold field of the specimen.

FEEM images can be captured by simply increasing the accelerating voltage with the illumination source switched off. Information about the distribution of emission sites and emission uniformity of the specimen can be acquired from these FEEM images.

PEEM instruments usually consist of five major components, including UV light source, sample manipulation system, electron optical system, imaging system, and vacuum system. A schematic section view of a typical PEEM is presented in Figure 2.6. The ultimate resolution of PEEM is limited by aberrations associated with the cathode lens and the accelerating electric field. To date, a state-of-the-art PEEM has a resolution

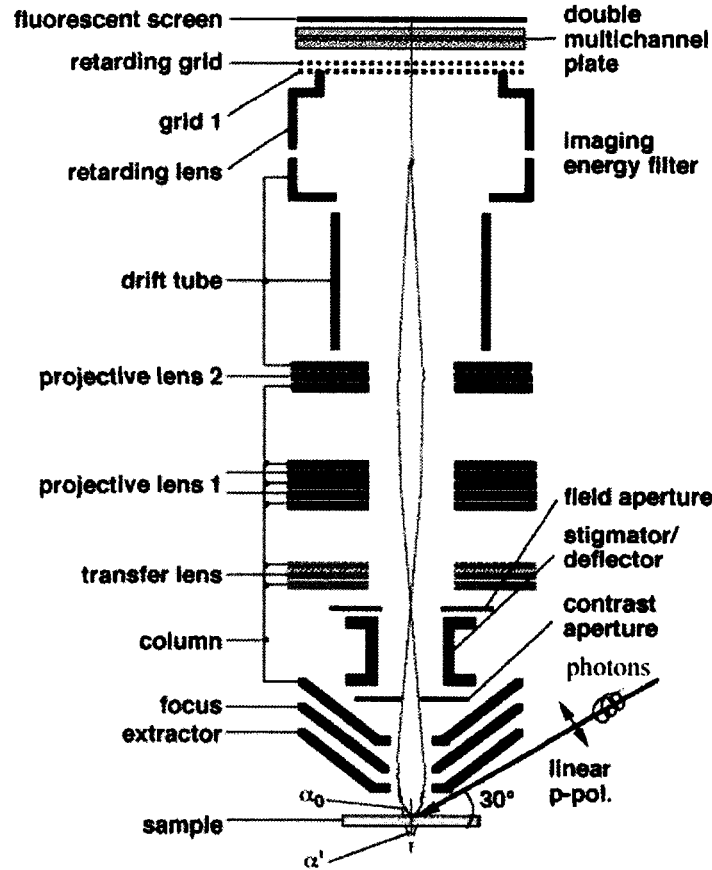


Figure 2.6 Diagram of major components of PEEM [7].

on the order of  $\sim 2$  nm. However, most PEEM instruments, including those used in this study, come nowhere near this best-case.

Two PEEM systems were used to conduct studies presented in this work. One is a modified Elmitec PEEM III with electromagnetic lenses at Ohio Univeristy, the other one is a modified Staib PEEM with electrostatic lenses at NIST. Photographs of these two systems are displayed in Figure 2.7. Both PEEM systems have a spatial resolution on the order of  $\sim 1$   $\mu\text{m}$  at the operation pressure of  $\sim 10^{-8}$  Torr with an accelerating electric

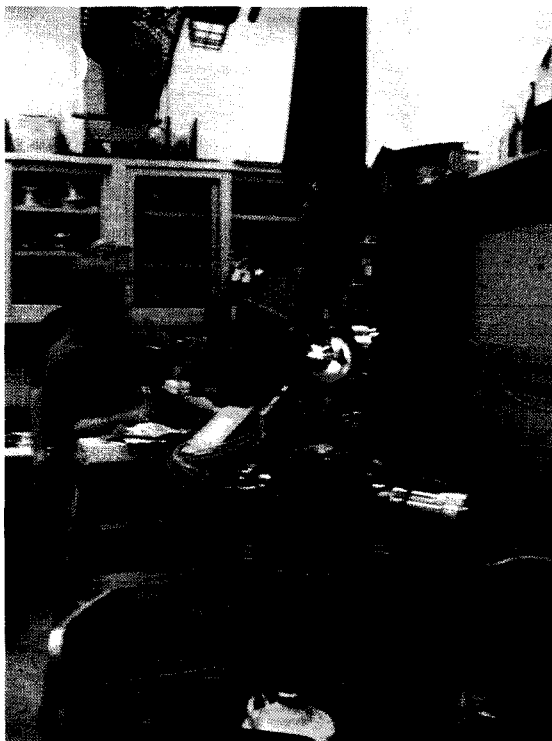
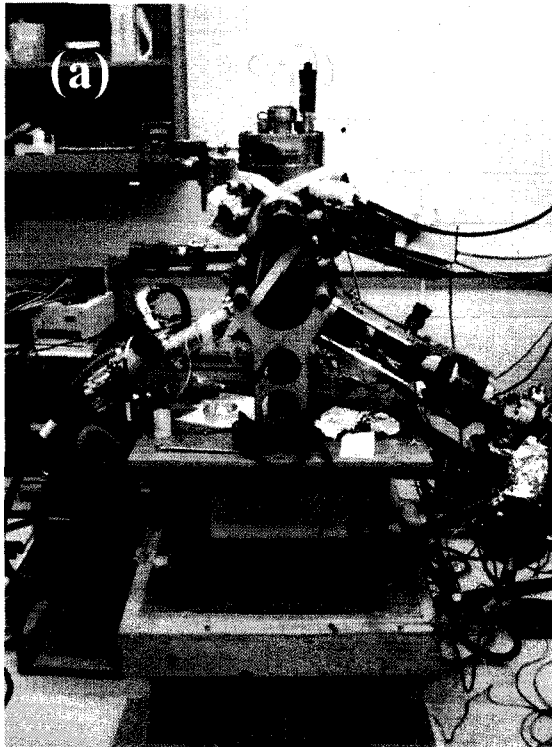


Figure 2.7 Pictures of applied PEEM systems. (a) A modified Elmitec PEEM III at Ohio University, (b) a modified Staib PEEM at NIST.



field of  $\sim 5$  V/ $\mu\text{m}$ . When these two PEEM systems work as FEEM, the spatial resolution is usually significantly degraded.

## 2.6 FIELD EMISSION MEASUREMENT

Field emission (FE) measurement is a characterization technique concentrating on the spatially average electrical properties of specimens. By measuring the emitted current from the specimen with respect to the applied field, comparative studies aimed at optimizing field emission performances of device-sized samples (0.1-10 mm) can be conducted.

FE measurement is conducted by applying an electric field between the sample and the anode and measures the current collected in the anode. FE test requires a high vacuum environment, usually with the pressure of the testing chamber on the order of  $1 \times 10^{-8}$  Torr or better, to minimize gas effects on the sample performance. Neutral and ionized residual gas molecules can strike the sample surface during the FE test, causing gas adsorption, changes of work function, and ion bombardment damage to the sample. Meanwhile, outgassing of the anode due to electron bombardment produces molecules or ions that may also affect the sample via adsorption and bombardment effects that degrade its field emission performance.

A FE test system normally consists of five major components, including ultra-high vacuum (UHV) testing chamber, sample holder assembly, high voltage power supply unit, current measurement unit, and PC-based data collection system. A schematic of the automated FE measurement system used in this work is presented in Figure 2.8. The sample is placed in an UHV vacuum test chamber equipped with an OSAKA

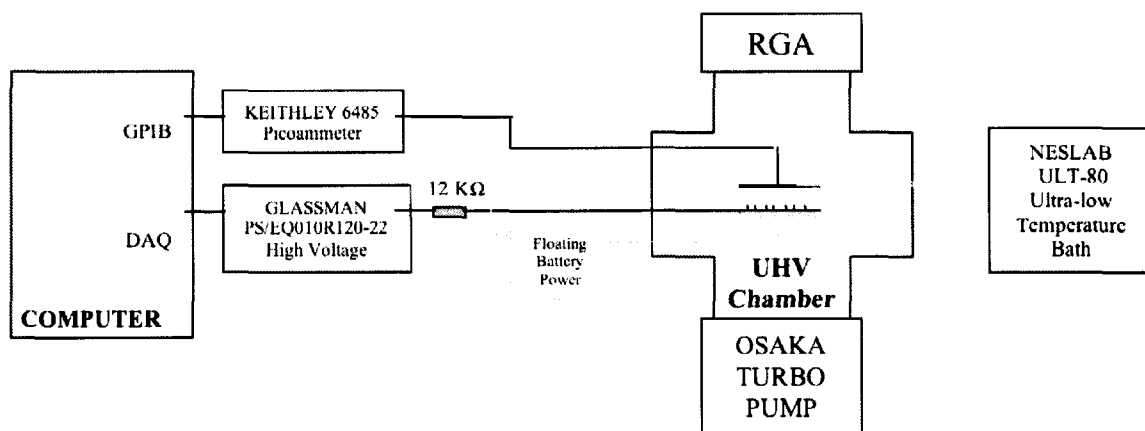


Figure 2.8 A schematic of the automated FE measurement system.

magnetically levitated 1000 l/s turbo molecular pump that gives a base pressure of  $\sim 1 \times 10^{-10}$  Torr. Vacuum compatible electric feedthroughs allow application of high voltage to the cathode and measurement of the current collected by the anode. The cathode and anode are part of the sample holder assembly that is cooled by a NESLAB ULT-80 ultra low temperature bath to dissipate the heat at the anode that is generated by the electron bombardment. A negative bias is supplied to the specimen (the cathode) by a Glassman PS/EQ010R120-22 high voltage power supply that can provide up to 10 kV at 1 A. The emitted current is measured by a Keithley 6485 Picoammeter that can measure down into the pA range. A 12 k $\Omega$  resistor is connected in series between the Glassman power supply and the specimen to protect the power supply and the picoammeter by limiting transient currents. In triode device tests, a floating, battery-driven power supply of up to 120 V is inserted into the circuit to supply a positive bias to the gate relative to the cathode. Data collection is automated by Labview PC programs. Twice each second,

the collecting system records the measured anode current ( $I$ ), applied voltage ( $V$ ), and applied electric field ( $F$ ) into a text file. The recorded anode current is an average over one hundred such measured anode currents. A picture of the FE test system is displayed in Figure 2.9.

The sample holder assembly is the core component of the FE test system, which usually consists of an anode, a cathode (the specimen under test), a sample stage, spacers, and other parts. Three kinds of sample holder assemblies were used in this work: a cartridge holder assembly, a diode holder assembly, and a 24-pin header assembly.

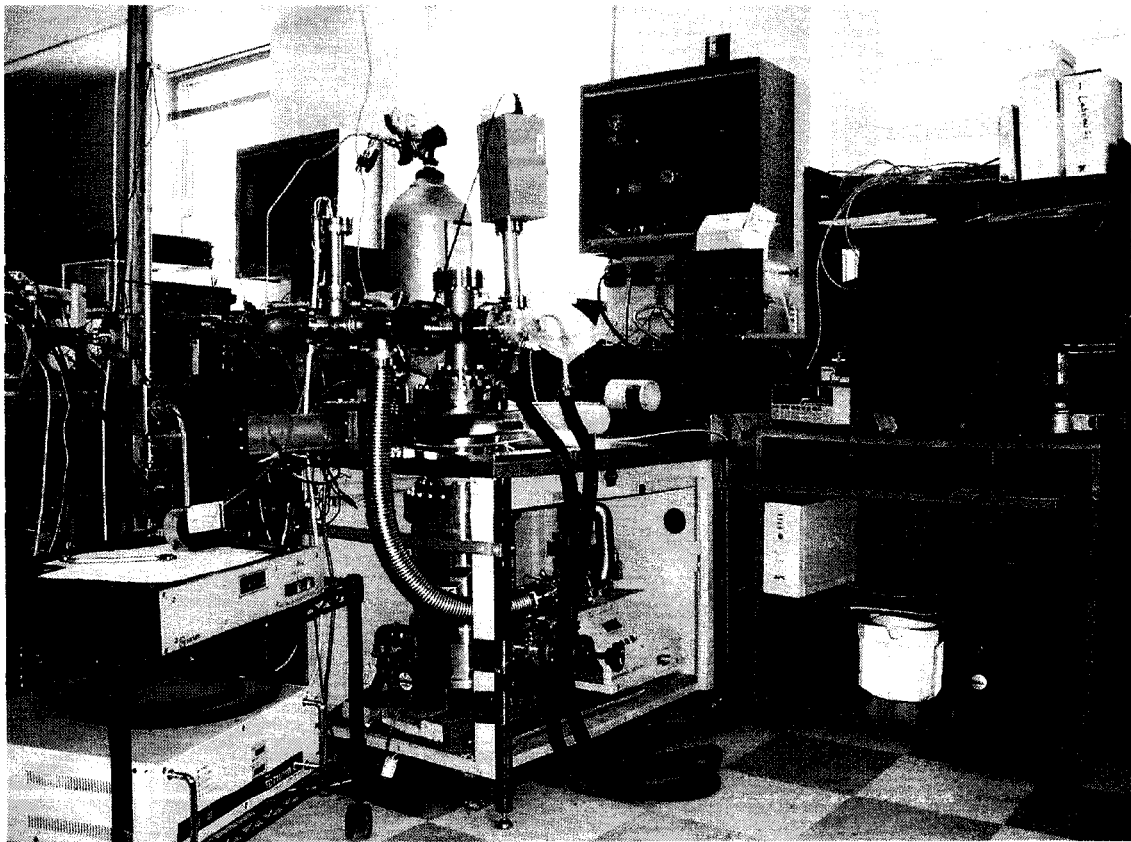


Figure 2.9 A picture of the automated FE test system.

The cartridge holder assembly was designed to accommodate the carousel of a Physical Electronic 590 surface analysis system. A schematic of the cartridge sample holder is shown in Figure 2.10. The specimen, usually carbon nanofibers deposited on TiW substrates, forms the cathode in the assembly. The cathode is insulated from the grounded stainless steel cartridge and a stainless steel plate by two  $\text{Al}_2\text{O}_3$  spacers that are each 125  $\mu\text{m}$  thick. The stainless steel plate anode is parallel to the cathode to construct a plane-to-plane diode testing configuration. Since the assembly is close packed, the gas conductance between the anode and the cathode is poor. As a result, arcing frequently occurs and damages the sample in the process of high current (over mA range) measurements.

The 24-pin header assembly was originally designed for the triode test of carbon nanostructure based field emission devices, but was also employed for diode test of samples. The device, or the sample, is placed on top of two 500  $\mu\text{m}$  Si rectangular

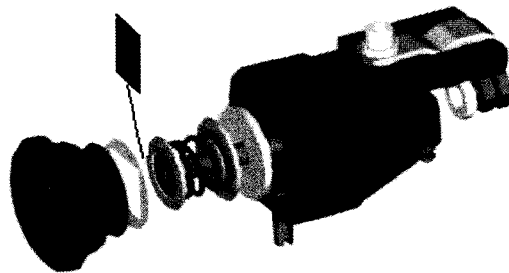


Figure 2.10 A schematic of the cartridge holder assembly.

spacers in the well of the 24-pin header, between which indium solder is located. When the temperature of the assembly is raised to  $\sim 160^{\circ}\text{C}$ , the stack is pressed until it joins the two spacers with melted indium. The device or the specimen is therefore firmly soldered to the well of the 24-pin header (Evergreen Semiconductor Materials, Part No. KD-78516-C). The cathode and gate of the device are connected to the specific pins of the 24 pin header by double wire bonding. A photograph of the 24 pin header assembly is displayed in Figure 2.11. In the case of diode test, no wire bonding is required. A tantalum plate anode is positioned over the well, parallel to the device, or the specimen, to form a plane-to-plane test configuration. The time-consuming hand-assembling procedures of the 24-pin header limit the number of tests that can be done. Moreover, the

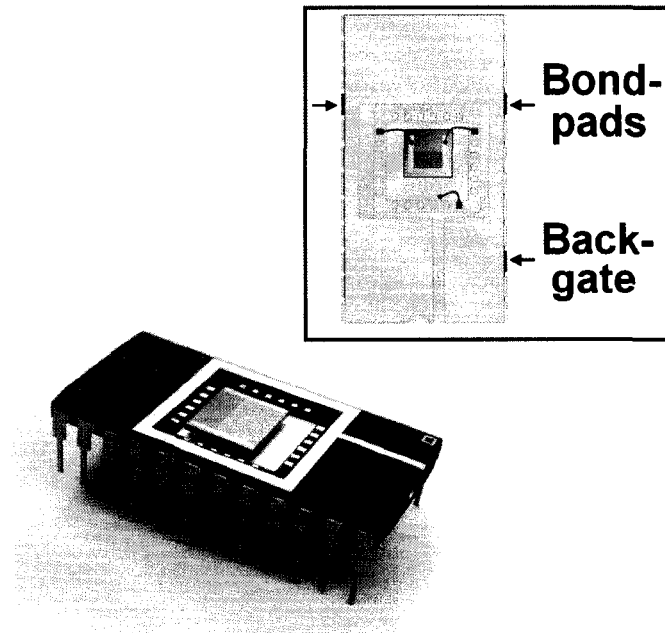
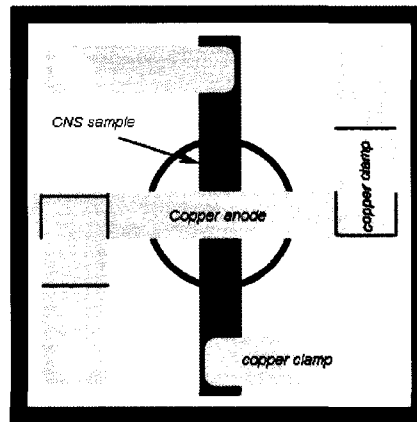


Figure 2.11 A photograph of the 24 pin header assembly [8].

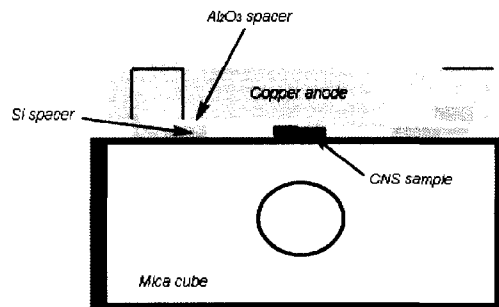
dielectric breakdown on the 24-pin header itself can occur when a high voltage ( $> 5000\text{V}$ ) is applied. Nevertheless, the 24-pin header assembly is the preferred sample holder assembly for triode tests.

The diode holder assembly was designed to maximize the gas conductance between the anode and the specimen during the diode test. A polyimide or mica cube,  $32\text{ cm}\times 32\text{ cm}\times 15\text{ cm}$  in size, is used as the sample stage in the assembly. The cube is machined to form a vacuum conductance hole with a diameter of 12 mm in the center of the stage. A top view schematic of the diode holder assembly is displayed in Figure 2.12(a). The specimen is laid over the central hole of the stage and held by two copper clamps. An electrically grounded copper bar,  $6\text{ mm}\times 32\text{ cm}\times 6\text{ mm}$ , is used as the anode, which is placed above two  $254\text{ }\mu\text{m}$   $\text{Al}_2\text{O}_3$  spacers on top of two  $500\text{ }\mu\text{m}$  Si rectangular spacers to generate an anode and cathode spacing of  $254\text{ }\mu\text{m}$ . The copper anode is laid across the specimen and also held by two copper clamps, as shown in Figure 2.12(b). To remove the heat generated in the test, especially during direct current lifetime tests, a 10 mm wide copper belt is mounted on the anode by tightening a bolt through a larger copper bar to ensure that the upper surface of the anode is completely and firmly contacted by the belt. Meanwhile, the other end of the belt is mounted onto a vacuum-compatible copper electric-feedthrough that is cooled by the ultra low temperature bath. A picture of the diode holder assembly mounted with the copper electric-feedthrough is shown in Figure 2.12(c). The open space between the anode and the cathode together with the cooling setup for the anode allow this assembly being employed for the high emission current measurement up to tens of milliamperes and for the direct current lifetime test at the current level of more than 1 mA for hundreds of hours.

(a)



(b)



(c)

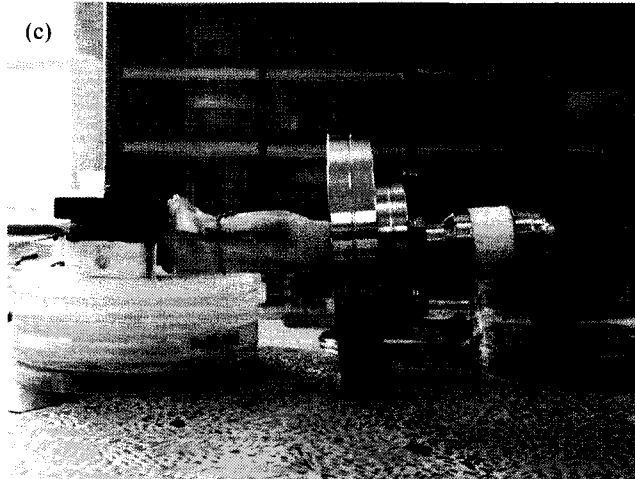


Figure 2.12 (a) The top view schematic of the diode holder assembly, (b) the cross-sectional view schematic of the diode holder assembly, (c) a picture of the diode holder assembly mounted with the copper electric-feedthrough.

## 2.7 Summary

In this work, a variety of materials characterization techniques have been employed to investigate the morphology, microstructure, composition, and functional properties of carbon nanostructures, including SEM, EDX, Raman, AES, PEEM/FEEM, and FE. An introduction to these characterization techniques together with their operational principles is briefly summarized here.

Since this thesis focuses on the field emission properties of carbon nanostructures, FE and SEM are the most frequently used methods to understand the relationship between the material morphology and its field emission properties. PEEM/FEEM are also applied to investigate the field emission uniformity of carbon nanostructures through the observation of emission site distributions. In addition, Raman provides microstructure information of carbon nanostructures. XRD and Auger is applied to investigate the surface component of coated carbon nanostructures.



## References for Chapter II

- [1] Goldstein JI, Newbury DE, Echlin P, Joy DC, A.D. Roming J, Lyman CE, Fiori C, Lifshin E. Scanning Electron Microscopy and X-ray Microanalysis: Plenum Press, New York 1992.
- [2] Ferraro JR, Nakamoto K, Brown CW. Introductory Raman Spectroscopy: Academic Press 2003.
- [3] Dresselhaus MS, Dresselhaus G, Saito R, Jorio A. Raman spectroscopy of carbon nanotubes. Physics Reports. 2005;409(2):47-99.
- [4] McCreery RL. Raman Spectroscopy for Chemical Analysis: John Wiley & Sons, Inc 2000.
- [5] Vickerman JC. Surface Analysis: The Principle Methods: John Wiley & Sons Inc. 1997.
- [6] Zhao X. Field emission study of carbon nanostructure: College of William and Mary; 2006.
- [7] [www.physik.fu-berlin.de/~ag-kuch/PEEM.html](http://www.physik.fu-berlin.de/~ag-kuch/PEEM.html). 2007.
- [8] Tyler T, Shenderova O, Ray M, Dalton J, Wang J, Outlaw R, Zhu M, Zhao X, McGuire G, Holloway BC. Back-gated milliamper-class field emission device based on carbon nanosheets. Journal of Vacuum Science & Technology B: Microelectronics and Nanometer Structures. 2006;24(5):2295-301.

## CHAPTER III

### FIELD EMISSION PROPERTIES OF CARBON NANOFIBERS

#### 3.1 INTRODUCTION

This chapter outlines the synthesis, structure, and field emission properties of carbon nanofibers (CNF) directly deposited on blank TiW substrates by direct current plasma enhanced chemical vapor deposition (DC PECVD), as well as the field emission performance of a CNF based back gate triode device. The mechanism of achieving aligned CNF by manipulation of the local electric field across the plasma sheath and the growth rate of CNF through the adjustment of input plasma power is also presented.

Carbon nanofibers (CNF) [1], also called bamboo-like carbon nanotubes, are distinguished from carbon nanotubes (CNT) by the orientation of graphene layers with respect to the cylinder axis. Unlike CNT whose graphene layers are parallel to the tube axis, a CNF has an orientation angle less than  $90^\circ$  between its graphene layers and its axis. Carbon nanofibers are typically synthesized using thermal chemical vapor deposition (TCVD), which is a process whereby a solid material is deposited from a vapor by a chemical reaction occurring on or in the vicinity of a substrate surface [2]. Conventional CVD solely relies on the thermal energy to activate the chemical reactions and requires a high substrate temperature of more than  $800^\circ\text{C}$  in the case of CNF and CNT deposition. However, such a high CNF deposition temperature is not compatible with field emission device processing that requires lower temperatures. A high substrate

temperature in the process of emissive material deposition on field emission devices can cause metal atoms to diffuse into the dielectric layer used to separate the cathode and the gate that is usually a SiO<sub>2</sub> film with a thickness of hundreds of nanometers, leading to the device failure in future tests. Therefore, a plasma enhanced chemical vapor deposition (PECVD) is employed for the CNF synthesis for field emission devices, in which a chemical reaction is activated by a plasma. Consequently, the deposition temperature is substantially decreased. Our group, as well as others, have successfully synthesized CNF on various substrates such as Si, Ti, W, Ta, and Au, using PECVD [3-6]. In general, a buffer layer has been required between the catalyst film and the substrates to prevent the catalyst from diffusing into the substrate. For example, buffers such as TiN and SiO<sub>2</sub> [7], have been commonly used. However, the introduction of these layers in field emission devices not only complicates device fabrication, but the high resistance of these layers also degrades performance.

Carbon nanofibers have been considered as an electron emissive material for vacuum electronic devices due to their unique combination of physical, electronic and thermal properties, as well as their high geometrical aspect ratio [8-10]. Traditional field emission triode devices have their gates situated between the anode and cathode, providing the field necessary to initiate electron emission at an applied voltage on the order of several hundreds volts [11]. However, some shortcomings of this type of device, such as the complicated processing steps and frequent failure from arcing and ion sputtering, are well known. Therefore, the use of a field emission device geometry called a back gate triode, where the perturbing gate field is generated by an electrode hidden behind the cathode rather than situated between the anode and the cathode as in

traditional triode devices have been proposed [12-16]. Such a back gate triode structure is able to protect the gate from catastrophic arcs and the influence of electron or ion bombardment, which improves the device robustness and reliability. Moreover, a carefully shaped cathode geometry combined with a layer of CNF along the central ridge of the cathode lines can overcome the high gate voltage required for device operation and the dielectric layer breakdown caused by charge-injection during the operation. Two-dimensional electrostatic modeling of the field above the cathode crest suggests that the highest electric field points are expected to concentrate on aligned CNF along the crest. Therefore, successful operation of back gate triode devices require the ability to directly synthesize aligned CNF on the top of the cathode crest without using a buffer layer.

### 3.2 DIRECT CURRENT PLASMA ENHANCED CHEMICAL VAPOR DEPOSITION (DC PECVD) APPARATUS

A plasma is a collection of free charged particles moving in random directions that is, on the average, electrically neutral [17]. The types of plasma employed together with CVD are microwave (MW), radio frequency (RF), and direct current (DC) according to the type of power coupled to the plasma. In this section, we describe a DC PECVD apparatus designed and constructed for the purpose of CNF deposition.

A schematic of the DC PECVD apparatus is displayed in Figure 3.1. The apparatus is built upon a stainless steel chamber equipped with a LEYBOLD turbo pump and an Edwards two-stage mechanical pump, which can offer a base pressure of  $\sim 2 \times 10^{-7}$  Torr. Two stainless steel plates parallel to each other are the cathode and the anode in the apparatus, respectively. One stainless steel plate fits with the sample holder that contains

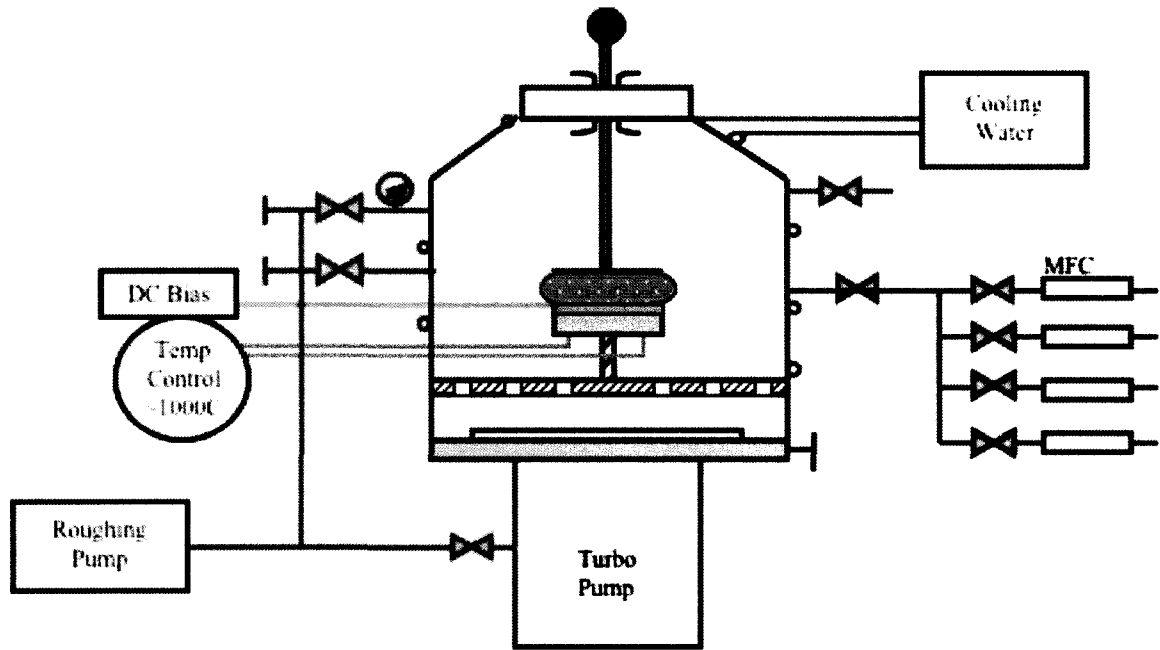


Figure 3.1 Schematics of DC PECVD apparatus.

a commercial four-inch GE ceramic heater, serving as the cathode. Another stainless steel plate of equal diameter functions as an electrically grounded, movable anode whose position can be adjusted to provide a plasma gap from 0 to 4 cm wide by adjusting a linear motion feedthrough. Gases, including Ar, NH<sub>3</sub>, C<sub>2</sub>H<sub>2</sub>, H<sub>2</sub>, and CH<sub>4</sub>, are introduced to the apparatus by separate mass flow controllers (MFC). A picture of the DC PECVD apparatus is displayed in Fig. 3.2.

Using a negative dc bias applied to the cathode, a dc glow discharge is generated between two electrodes. The generation of the dc glow discharge is as follows. When an electric field is applied to the gas species between the electrodes, a small number of initial charge carriers in the gas start moving towards the electrodes. Since ions are heavier than electrons, energy is transferred more rapidly to the electrons than the ions.

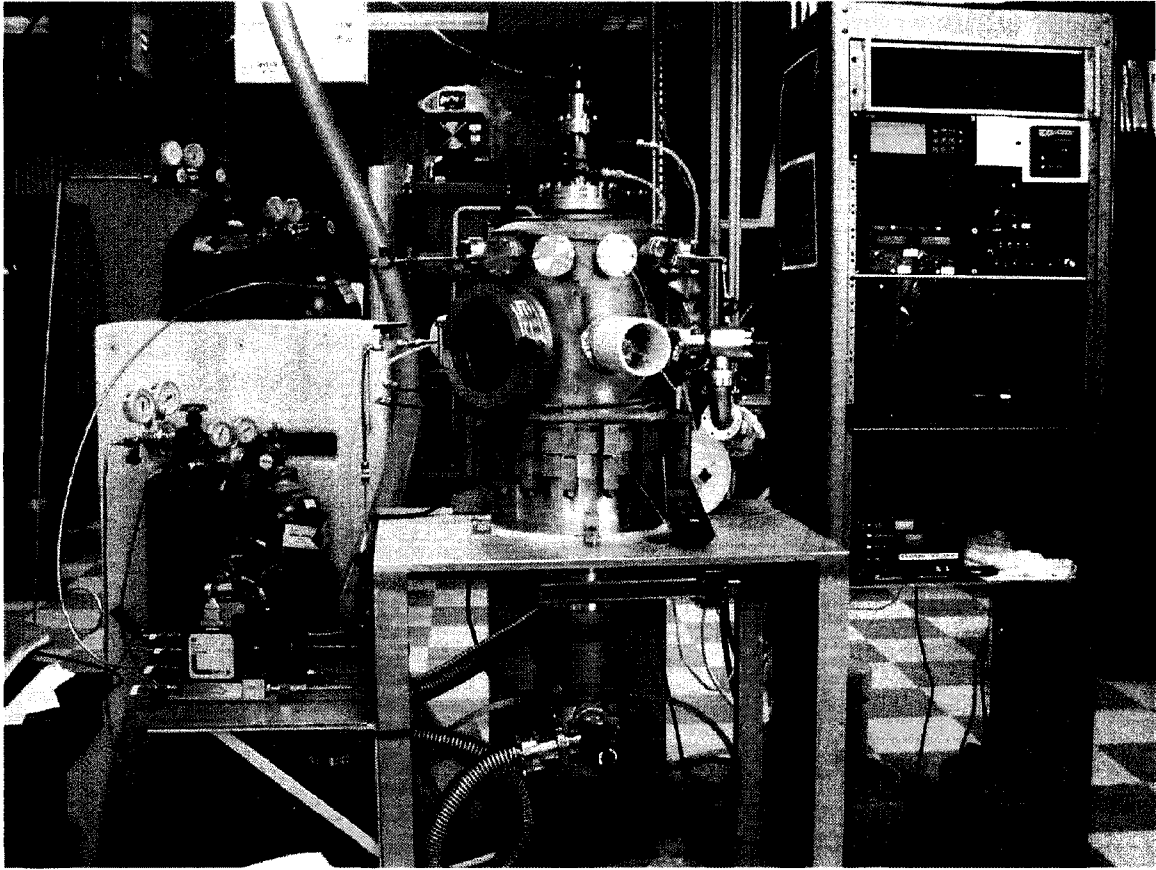


Figure 3.2 A picture of the DC PECVD apparatus.

Therefore, electrons can accumulate sufficient kinetic energy to have a high probability of producing excitation or ionization during collisions with neutral particles on their way to the electrodes. Meanwhile, the ions collide with the cathode to release secondary electrons. When enough of the electrons generated produce sufficient ions to regenerate the same amount of electrons consumed, the discharge becomes self-sustaining.

The electrons tend to flow from the plasma to adjacent electrodes at a faster rate than the ions. Consequently, a nonneutral potential region between the plasma and the cathode is formed, which is called as a cathode sheath. In the region of this sheath, most

of voltage drop occurs.

The electric field generated across the cathode sheath has been shown to provide carbon nanofiber alignment by inducing dipole moments preferentially along the axis of carbon nanofibers [18, 19]. These dipole moments act to align the fiber in the direction of the field and combat any randomizing effects during CNF growth. The sheath electric field can be estimated from the Child's Law, which gives the space-charge-limited current between two plane electrodes as a function of the potential difference between them with fixed spacing. Below we review the derivation of the sheath electric field given by Lieberman and Lichtenberg beginning with the Child's law [17]:

$$J_0 = \frac{4}{9} \epsilon_0 \left( \frac{2e}{M} \right)^{1/2} \frac{V_0^{3/2}}{s^2} \quad (3.1)$$

where  $J_0$  is the ion current density,  $M$  is the ion mass,  $V_0$  is the applied bias, and  $s$  is the sheath thickness. Since the bias applied to the cathode is highly negative with respect to the plasma-sheath edge, only ions are present in the cathode sheath [17]. Moreover, the ion flux conservation can be written in the form as

$$J_0 = en_0 u_B \quad (3.2)$$

where  $n_0$  is the ion density at the plasma-sheath edge, and  $u_B$  is the Bohm velocity defined by

$$u_B = \left( \frac{eT_e}{M} \right)^{1/2} \quad (3.3)$$

The sheath thickness,  $s$ , therefore can be obtained by substituting Eq. 3.3 into Eq. 3.2, and introducing the electron Debye length at the plasma-sheath edge in the form of

$$s = \frac{\sqrt{2}}{3} \lambda_{De} \left( \frac{2V_0}{T_e} \right)^{3/4} \quad (3.4)$$

where

$$\lambda_{De} = \left( \frac{\epsilon_0 T_e}{en_0} \right)^{1/2} \quad (3.5)$$

is the electron Debye length and  $T_e$  is the electron temperature. A typical glow discharge is characterized by  $T_e \approx 1 - 10V$  and  $n_0 \approx 10^8 - 10^{13} \text{ cm}^{-3}$  [17]. Hence, the cathode sheath can be of order of 100 Debye lengths in a glow discharge.

Typical deposition parameters applied for CNF synthesis in this chapter are 4.8 Torr chamber pressure, 635°C substrate temperature, and 400-600 V applied negative bias. By taking a representative ion energy about half of the bias voltage, the working plasma density ( $n_0$ ) is derived to be  $\sim 10^{10} \text{ cm}^{-3}$  from the plasma current density at -600 V bias, which is  $2.16 \text{ mA}\cdot\text{cm}^{-2}$ . The electron temperature ( $T_e$ ) here is taken as 1.5 eV [3]. Consequently, the cathode sheath is roughly estimated to be at least 1 mm in thickness, as visually observed during the deposition. Correspondingly, the electric field generated across the plasma sheath is several tenth volts per micron depending on the negative bias applied to the cathode.

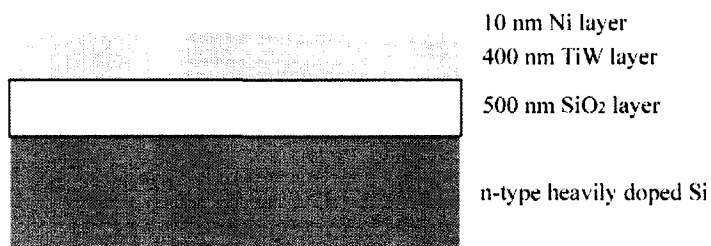
### 3.3 DEPOSITION OF CARBON NANOFIBERS

Two types of substrates are used for this study: blank TiW substrates and back gate triode field emission devices using TiW crests as the cathode, displayed in Fig. 3.3. In both cases, there are no buffer layers applied between the catalyst layer and TiW layer.

Blank TiW substrates were fabricated on heavily doped n-type Si wafer (resistivity of  $0.001 \sim 0.005 \text{ }\Omega\cdot\text{cm}$ ) with a  $0.5 \text{ }\mu\text{m}$   $\text{SiO}_2$  dielectric layer formed by thermal oxidation. Afterward, a 400 nm thick TiW film is sputtered over the  $\text{SiO}_2$  dielectric layer. Then a 10 nm Ni film is evaporated on the TiW film as catalysts for the CNF growth.



(a) blank TiW substrate



(b) back gate triode device

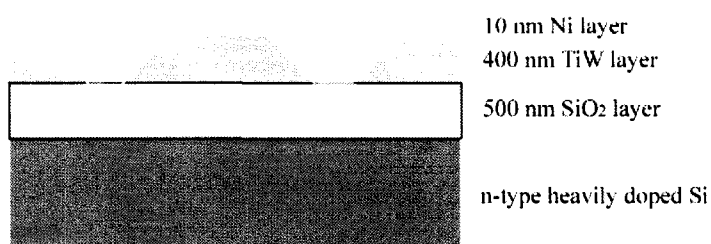


Figure 3.3 Schematics of blank TiW substrate and back gate triode device.

The fabrication process for the back gate triode field emission device is similar to that for the back-gated buried line device reported elsewhere [20, 21]. In this work, the sequence starts with a heavily doped n-type Si wafer with a 0.5  $\mu\text{m}$  SiO<sub>2</sub> dielectric layer formed by thermal oxidation. Subsequently, positive photo-resist is patterned to form a series of lines and streets having 4 $\mu\text{m}$  line widths and a 12  $\mu\text{m}$  center-to-center distance. After sputtering a 400 nm thick TiW layer and evaporating a 10 nm Ni film as a catalyst for CNF growth over the patterned resist, a lift-off process was used to remove the photoresist to complete the back gate triode fabrication.

To deposit CNF on both blank TiW substrates and back gate triode devices, the DC PECVD apparatus was initially pumped down to  $10^{-4}$  Torr. The substrates were placed on

the cathode of the apparatus and the distance between the anode and the cathode was held constant at 1 cm. The temperature of the substrate was maintained at 635°C. Acetylene ( $C_2H_2$ ) and ammonia ( $NH_3$ ) were used as the carbon source and the etchant gas, respectively. The carbon nanofiber synthesis was performed at a pressure of ~4.8 Torr.  $NH_3$  flow was first introduced to the chamber at 40 sccm, the plasma was then initiated by applying a negative dc bias to the sample holder. The desired plasma power in the range of 16-100W was achieved by varying the applied dc bias from 400 V to 600 V. Afterward, 10 sccm  $C_2H_2$  was immediately introduced to the chamber by a separate mass flow controller. The CNF deposition lasted 10 minutes.

In the case of CNF synthesis on back gate triode devices, co-deposited amorphous carbon on these devices was removed after the synthesis by soaking in a hydrofluoric solution for 5 minutes, followed by rinsing in de-ionized water, and then placed in an ultrasonic bath for 30 seconds.

### 3.4 CHARACTERIZATIONS OF CARBON NANOFIBERS

SEM images of carbon nanofibers are shown in Figure 3.4(a)-(d), which are synthesized on blank TiW substrates at ~635°C with plasma powers of 16W, 51W, 72W, and 100W, respectively. Only spaghetti-like (twisted) CNF are observed on TiW substrates at a plasma power of 16W. The bottom part of the spaghetti-like CNF is vertical to the TiW substrate; the top has a random orientation. At 51W and 72W of plasma power, both spaghetti-like and aligned CNF are observed on the TiW substrate. Interestingly, it can be seen that CNF grown at 72 W plasma are more aligned than those grown in a 51W plasma, a trend which continues until 100 W, where only aligned CNF

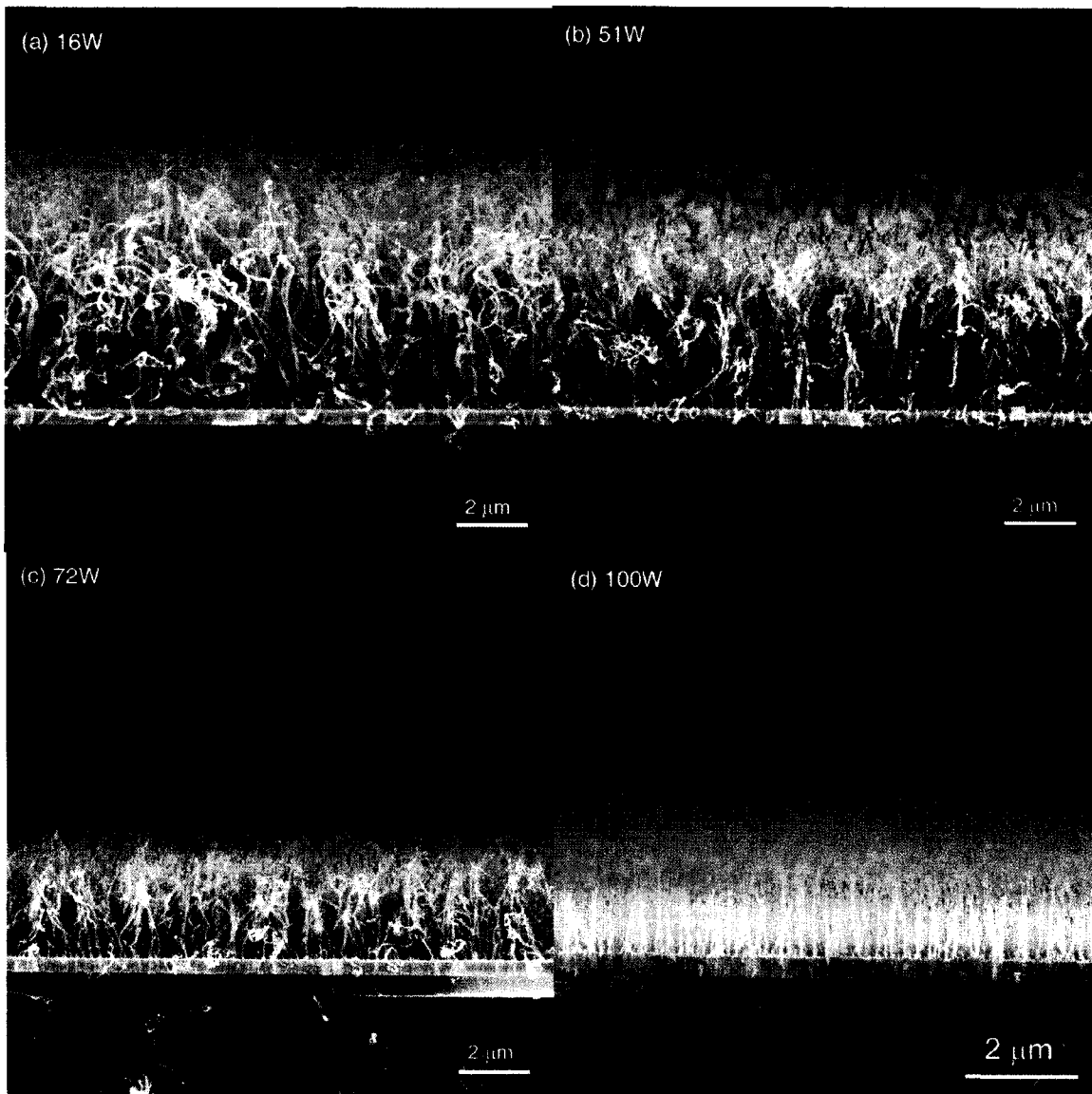


Figure 3.4 SEM images of carbon nanofibers synthesized on blank TiW substrates under different plasma powers, (a) 16W, (b) 51W, (c) 72W, (d) 100W.

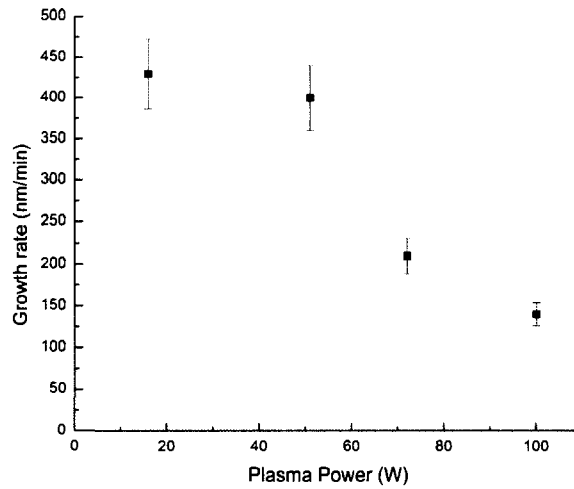


Figure 3.5 Average growth rate of CNF as a function of plasma power.

are observed. The growth rate of CNF can be calculated by dividing the average height of CNF as observed from the SEM image by the growth time, shown in Figure 3.5. The results reveal that the CNF growth rate declines with increasing plasma power. It is found that aligned CNF are fabricated when their average growth rate is lower than 150 nm/min.

The HRTEM image of a typical CNF grown on the TiW substrate is shown in Figure 3.6. It can be seen that CNF has a bamboo-like structure, in good agreement with the observations described elsewhere [1]. The graphene layers of the CNF are not perfectly aligned parallel to the fibers long axis and a thin amorphous carbon surface layer can also be seen in the image. The misalignment of graphene layers and the existence of the amorphous carbon layer indicate that CNF grown on the TiW substrate have more disorder compared with multi-walled carbon nanotubes presented in the

literature.

Raman spectra of CNF synthesized on blank TiW substrates under different plasma powers are displayed in Figure 3.7. Two peaks are presented in the spectra: one is located at  $\sim 1356\text{ cm}^{-1}$  representing a disorder-induced D-band, the other is located at  $\sim 1584\text{ cm}^{-1}$  and represents the tangential-mode G-band of well-ordered graphite. The ratio of the intensity of the D-band to the G-band has been widely used to determine the degree of disorder in carbon nanofibers and carbon nanotubes [22]. In this work, the intensities of D-band and G-band are calculated from the respective peak areas. The ratios of the intensity of D-band to G-band are 0.88, 1.00, 1.11, and 1.27 for plasma powers of 16W, 51W, 72W, and 100W, respectively. The increasing ratios of the intensity of the D-band to the G-band with increasing plasma power shows the higher the plasma power applied, the more disorder in the CNF structure.

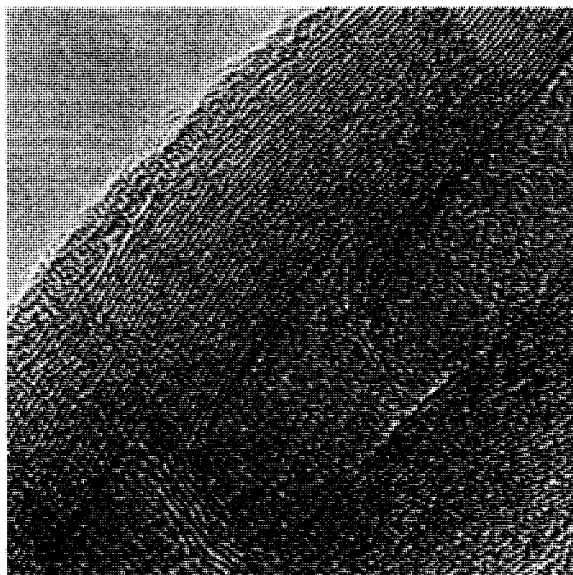


Figure 3.6 HRTEM image of a representative CNF grown on blank TiW substrate.

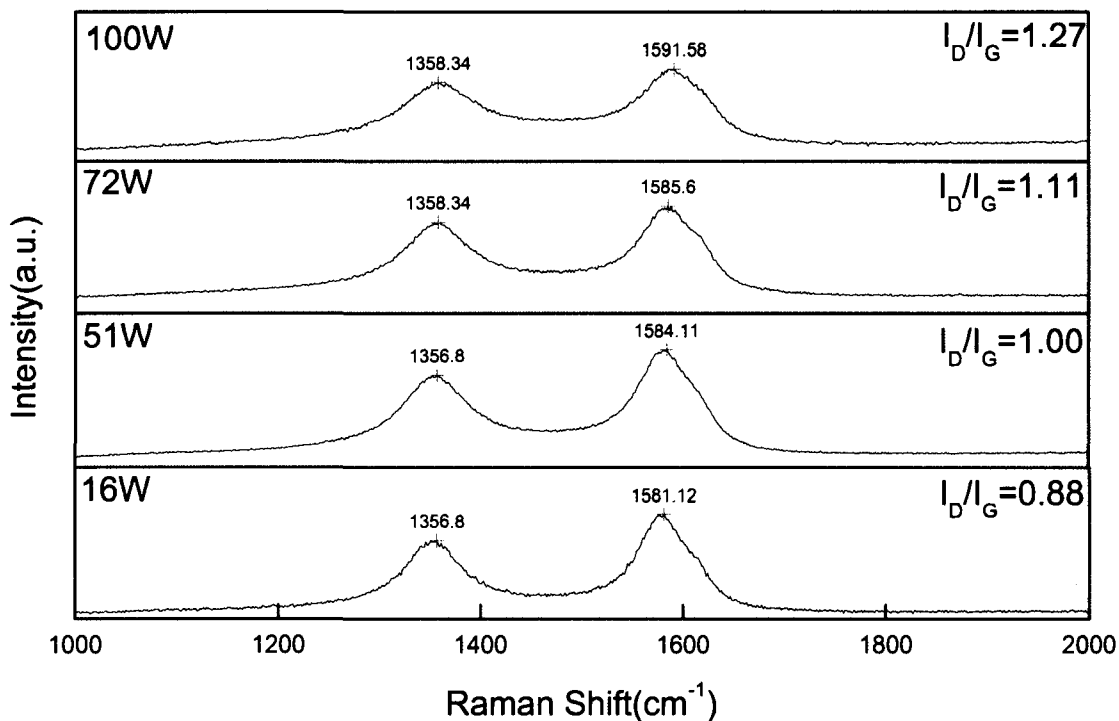


Figure 3.7 Raman spectra of CNF grown on blank TiW substrates with regarding to various plasma powers.

SEM images of spaghetti-like and aligned CNF based back gate triode devices grown at  $\sim 635^\circ\text{C}$  using a 75 mm-diameter cathode before and after post-treatment are displayed in Figure 3.8. Here, the back gate triodes were formed on  $4\ \mu\text{m}$  wide TiW lines having trapezoidal cross-sections separated by  $12\ \mu\text{m}$  streets. With this configuration the highest field points are expected to concentrate on carbon nanofibers present at the top of the cathode crests where the electrostatic screening effect on the nanofibers is reduced. Figs. 3.8(a) and 3.8(b) illustrate that both spaghetti-like and aligned CNF can be selectively grown on the top of TiW lines, decorated with a 10 nm thick Ni catalyst, using a 30W plasma and a 60W plasma, respectively. It is also observed that amorphous carbon

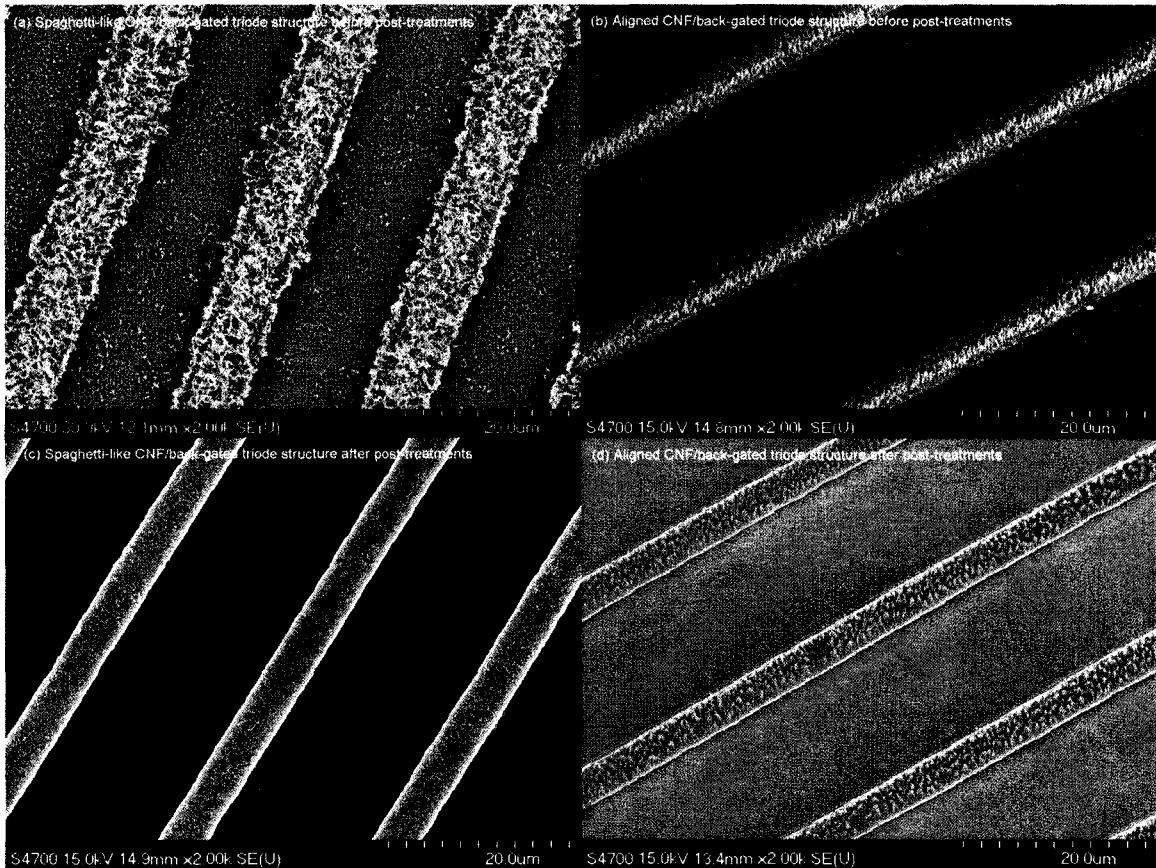


Figure 3.8 SEM images of spaghetti-like and aligned CNF based back gate triode device before and after post-treatments applied to clean the co-deposited amorphous carbon between two nearest TiW cathode crests. (a) spaghetti-like CNF based back gate triode device before post-treatments, (b) aligned CNF based back gate triode device before post-treatments, (c) spaghetti-like CNF based back gate triode device after post-treatments, (d) aligned CNF based back gate triode device after post-treatments.

is co-synthesized on the SiO<sub>2</sub> dielectric layer in the streets between the cathodes. The existence of the amorphous carbon on the dielectric layer not only can cause dielectric layer breakdown during the device operation, but also can significantly decrease the gate electric field penetration at the top of the cathode. Therefore, it is essential to remove the co-deposited amorphous carbon after the CNF growth. Figs. 3.8(c) and 3.8(d) show that soaking and ultra-sound cleaning steps successfully remove amorphous carbon. However, this post-processing procedure also can be seen to remove spaghetti-like CNF from the TiW back gate triode devices. Thus spaghetti-like CNF can not be used for such triode structures. Fortunately, although the density of aligned CNF is also diminished by the aggressive post-treatment, enough of the deposited aligned CNF survive to permit effective triode operation.

### 3.5 PLASMA DIAGNOSTICS

Generally speaking, carbon nanofibers are formed through a “solution-diffusion-precipitation” process with participation of various radicals generated by the plasma [1]. Knowledge of radicals in the plasma provides insight into not only understanding CNF formation, but also predicting morphology, structure, and property of CNF. Therefore, it is important to study radicals by plasma diagnostics. Optical emission spectroscopy (Ocean Optics USB2000) is employed here for this purpose. Emission peaks in the spectra allow us to identify corresponding radicals appearing in the plasma. A series of optical emission spectra of the working plasma were gathered with 10 sccm C<sub>2</sub>H<sub>2</sub> and 40 sccm NH<sub>3</sub> gas flow under 4.8 Torr at a substrate temperature of ~635°C under various plasma powers. All spectra are averaged over a minimum of three individual



measurements to improve the signal-to-noise ratio. To compare with the spectra obtained from the working plasma, spectra of pure acetylene and pure ammonia plasmas were also collected in the same pattern. The optical emission spectra of pure acetylene plasma, pure ammonia plasma, and the working plasma of CNF deposition with a power of 72W are displayed in Figure 3.9(a)-(c). The emission peaks are summarized in Table 3.1.

All emission peaks listed in Table 3.1 have been observed from spectra of the working plasma under various plasma powers. But only some of them could be observed from spectra of pure  $\text{NH}_3$  and pure  $\text{C}_2\text{H}_2$  plasma. Emission peaks of  $\text{N}_2$ ,  $\text{NH}$ ,  $\text{N}_2^+$ ,  $\text{H}_\alpha$ , and

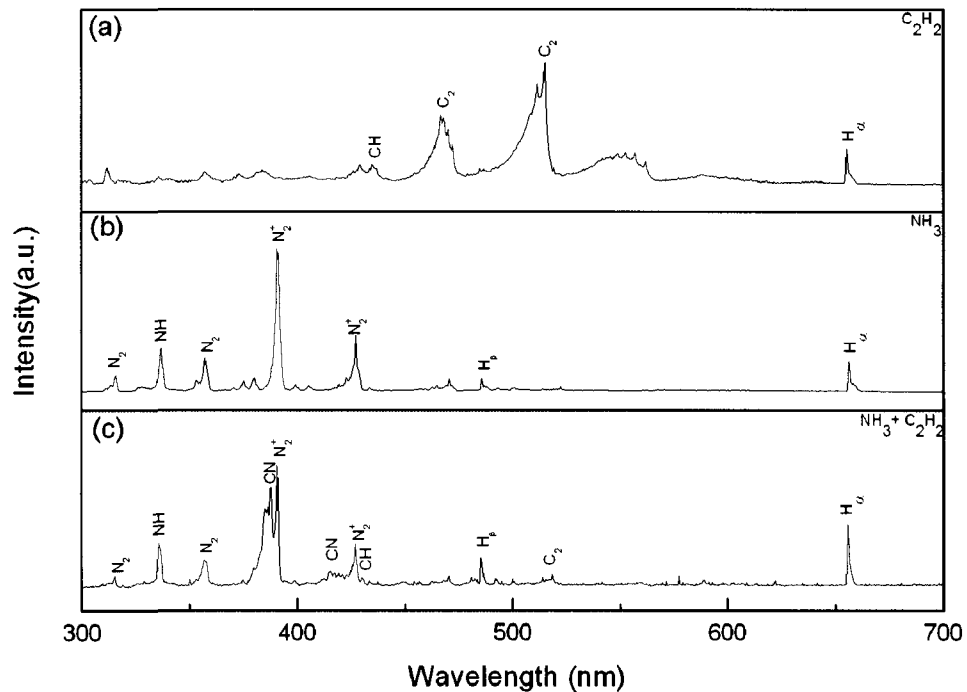


Figure 3.9 Optical emission spectra of (a) pure  $\text{C}_2\text{H}_2$  plasma, (b) pure  $\text{NH}_3$  plasma, and (c) a typical working plasma used for CNF synthesis on blank TiW substrates.

Table 3.1 Summary of emission peaks observed from the pure NH<sub>3</sub> plasma,  
the pure C<sub>2</sub>H<sub>2</sub> plasma, and the working plasma [21].

Emission Peak	Wavelength (nm)	System	Transition	Occurrence
N <sub>2</sub> <sup>+</sup>	391.4 427.8	First negative system	$B^2\Sigma_u^+ \rightarrow X^2\Sigma_g^+$	pure NH <sub>3</sub> plasma working plasma
CN	388.3 415.8	Violet system	$B^2\Sigma \rightarrow A^2\Pi$	working plasma
C <sub>2</sub>	516.5 473.7	Swan system	$A^3\Pi_g \rightarrow X^3\Pi_u$	pure C <sub>2</sub> H <sub>2</sub> plasma working plasma
N <sub>2</sub>	315.9 357.7	Second positive system	$C^3\Pi \rightarrow B^3\Pi$	pure NH <sub>3</sub> plasma working plasma
CH	431.0	4300 Å system	$A^2\Delta \rightarrow X^2\Pi$	pure C <sub>2</sub> H <sub>2</sub> plasma working plasma
NH	335.5	3360 Å system	$A^3\Pi \rightarrow X^3\Sigma$	pure NH <sub>3</sub> plasma working plasma
H <sub>α</sub>	656.3	Hydrogen atomic line		pure NH <sub>3</sub> plasma
H <sub>β</sub>	485.3			pure C <sub>2</sub> H <sub>2</sub> plasma working plasma

$H_{\beta}$  are observed in the spectrum of the pure  $NH_3$  plasma. Meanwhile, emission peaks of  $CH$ ,  $C_2$ ,  $H_{\alpha}$ , and  $H_{\beta}$  are found in the case of the pure  $C_2H_2$  plasma. The absence of emission peaks of CN violet system in both spectra of pure  $NH_3$  and pure  $C_2H_2$  plasma indicates that the CN radical must be formed through chemical reactions in the working plasma by consuming both nitrogen bearing and carbon bearing radicals generated from decomposed  $NH_3$  and  $C_2H_2$ .

The relative number density of radicals appearing in the plasma can be evaluated by the intensities of their corresponding emission peaks in spectra. Therefore, the intensities

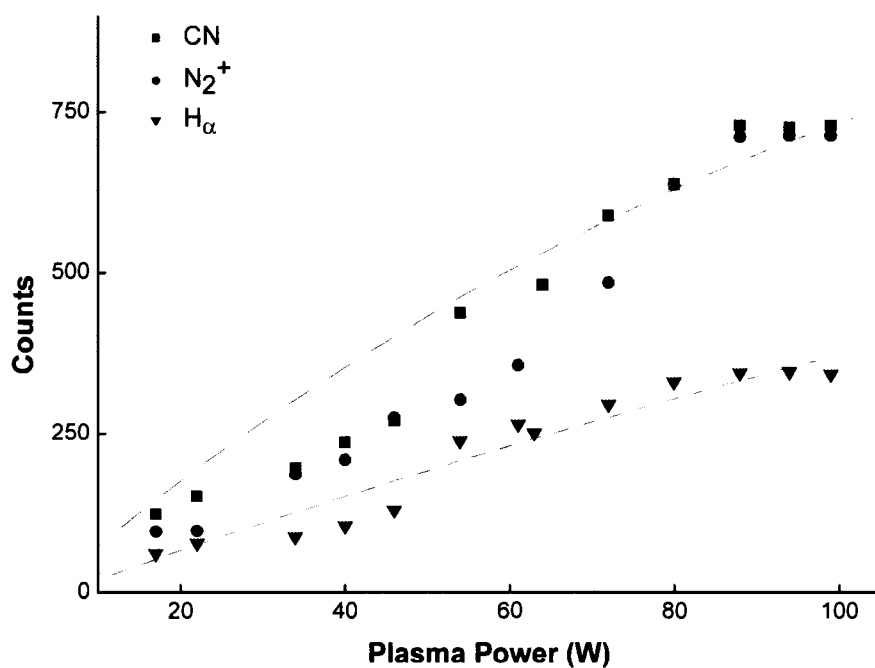


Figure 3.10 Intensities of CN violet system,  $N_2^+$  first negative system, and  $H_{\alpha}$  line detected from the working plasma as a function of plasma powers.

of CN violet system,  $N_2^+$  first negative system, and  $H_\alpha$  line representing the amount of CN radical,  $N_2^+$  radical, and H radical as a function of plasma powers are shown in Figure 3.10. It is found that all intensities increase with increasing plasma power from 16W to 88W, then stay roughly constant until the plasma power reaches the supply limit of 100W. The results are consistent with the observations of Hash et al [23], who found that the percentage of decomposed ammonia and acetylene increased rather than linearly in the working plasma as a function of the increasing DC plasma power in the low and medium plasma power range. Meanwhile, the percentage of decomposed ammonia and acetylene stayed constant in the high plasma power range. Hash et al found that almost 80% of the acetylene and 60% of the ammonia were decomposed at the highest plasma power.

Since the mass flow rate of  $C_2H_2$  and the chamber pressure were the same during all CNF depositions, the total amount of carbon remains unchanged under various plasma powers. However, it has been suggested that hydrocarbon radicals are more readily decomposed on Ni catalysts compared to cyanogens given that the C-N bond strength is 748 kJ/mol and C-H bond strength is only 338.4 kJ/mol [24]. Therefore, the increasing amount of cyanogen as a function of plasma power indicates a correspondingly reduced density of hydrocarbon radicals in the working plasma. As a result, the growth rate of CNF declines as a function of plasma power, consistent with the result shown in Fig. 3.5.

Fig. 3.10 also demonstrates that the amount of  $N_2^+$  and H increases with the plasma power, which is consistent with the higher decomposition rate of ammonia and acetylene at high plasma power. The increasing amount of  $N_2^+$  and H are likely to affect CNF

crystallinity. The atomic hydrogen plays an important role in removing co-deposited amorphous carbon from CNF, but can also lead to undesirable etching of nanofibers when a large amount of the atomic hydrogen is generated in the working plasma. Teo et al [24] pointed out that this undesirable etching causes nanofibers to be slightly undercut, which may generate nanoscale disorders in nanofibers. Further, when  $N_2^+$  ions travel through the cathode sheath, they gain substantial kinetic energy on the order of hundreds of eV. Even though collisions occur in the sheath, some fraction of energetic  $N_2^+$  ions can lead to damage in nanofibers. As more  $N_2^+$  ions are generated in the working plasma, a more intense ion bombardment occurs on nanofibers, consistent with our observation of ion current increasing from 40 mA at 16W plasma to 170 mA at 100W plasma. Therefore, much higher nanoscale disorder is expected to be observed from aligned CNF synthesized in an 100W plasma. This explains the increasing ratio of the D-band to the G-band with increasing plasma powers in Raman spectra, Fig. 3.7.

### 3.6 ALIGNMENT OF CARBON NANOFIBERS

We expect that the electric field generated in the plasma sheath and the growth rate of CNF play a significant role in determining the morphology of CNF synthesized by DC PECVD. The sheath width of the dc plasma used in this work is estimated to be at least on the order of 1mm, while carbon nanofibers are only a few micrometers in length. A strong electrostatic force acts on the nanofibers due to the induced polarization in the direction of the nanofiber axis. This electrostatic force creates a uniform tensile stress along the catalyst particle-nanofiber interface for the entire duration of CNF growth leading to a well-aligned vertical growth of CNF [19].

But vertical growth of CNF can not be maintained if there is a fluctuation in the tensile stress. This tensile stress fluctuation is thought to originate from the non-uniform carbon precipitation around the perimeter of the catalyst particle [25], causing nanofibers to bend and lose their alignment.

When the growth rate of CNF is fast, the electrostatic force acting on nanofibers is not large enough to overcome the misalignment caused by the tensile stress fluctuation before defects are locked into nanofibers by addition of more atoms. Then, spaghetti-like CNF is expected to synthesize on the substrate, as seen in cases of CNF grown on TiW substrates at plasma powers of 16W, 51W and 72W. On the other hand, when the growth rate of CNF is slow, the electrostatic force can overcome the tensile stress fluctuation. Thus, aligned CNF are expected to grow on TiW substrates, as seen in the case of CNF grown at the plasma power of 100W.

### 3.7 FIELD EMISSION OF CNF ON BLANK TiW SUBSTRATES

Field emission tests were conducted with a diode configuration in an UHV chamber. Samples were mounted into the cartridge holder assembly acting as the cathode. An electrically-grounded stainless steel plate, separated from the cartridge sample holder by a 300  $\mu\text{m}$  thick aluminum oxide spacers, serves as the anode. During the test, the cathode was biased by a high-voltage power supply (Glassman PS/EQ010R120-22)

Figure 3.11 shows the emission current as a function of the applied electric field and the corresponding Fowler-Nordheim (F-N) plot (inset) for the CNF grown on blank TiW substrates at different plasma powers. The turn-on field of CNF is defined here as the applied field required for an emission current of 1  $\mu\text{A}$ . The observed turn-on fields of

CNF samples grown at plasma powers of 16W, 51W, 72W, and 100W are 3.20 V/ $\mu\text{m}$ , 5.40 V/ $\mu\text{m}$ , 8.15 V/ $\mu\text{m}$ , and 12.10 V/ $\mu\text{m}$ , respectively. The results indicate the turn-on field of CNF increases with increasing plasma powers. The corresponding F-N plots presented in the inset show the approximate linear relationship in the measurement range. Thus the observed field dependence of the emission current is most likely non-linear consistent with a tunneling mechanism. The increasing turn-on field with increasing plasma power might be caused by a change of the field enhancement factor  $\beta$  of the nanofiber thin film. Here, the field enhancement factor  $\beta$  refers to the average geometric enhancement factor of the nanofiber thin film by averaging aspect ratios through all nanofibers and taking into account the screening effects from neighboring

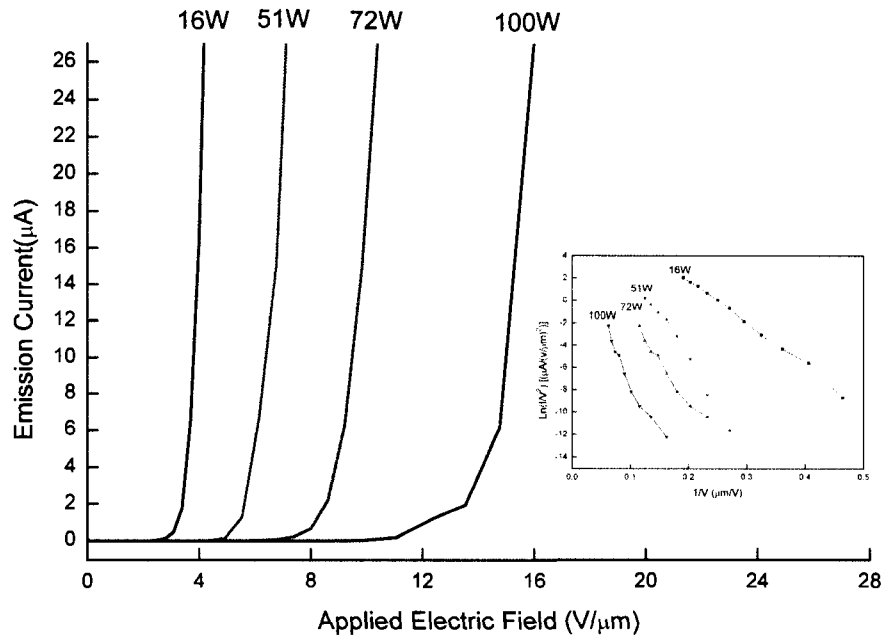


Figure 3.11 Emission currents as a function of the applied electric field and corresponding F-N plots (the insert).

nanofibers (See Sec. 4.6). The field enhancement factor  $\beta$  can be estimated from the slope of the F-N plot according to the normal expression of Fowler-Nordheim (FN) equation [26] defined as

$$I = \frac{1.54 \times 10^{-6} A \beta^2 V^2}{\Phi} \exp\left(\frac{-6.83 \times 10^7 \Phi^{3/2}}{\beta V}\right), \quad (3.6)$$

where  $A$  is the emission area and  $\beta$  is the field enhancement factor. Therefore, the slope of the F-N plot is equal to  $\frac{-6.83 \times 10^7 \Phi^{3/2}}{\beta}$ . If we assume that regardless of the

morphology, and independence of the degree of disorder, the average work function for these CNF materials is equal to that of bulk graphite ( $\sim 5$  eV) [27, 28], then the computed equivalent field enhancement beta factors would be 1938, 1164, 905 and 658 for CNF synthesized at plasma powers 16W, 51W, 72W and 100W, respectively. It seems more likely that the lower field enhancement factor can be attributed to the change in the average length of nanofibers that leads to the change in the aspect ratio of CNF and in the screening effect from neighboring nanofibers. We will discuss this in detail in a later chapter.

### 3.8 LIFETIME IN A DC MODE

The emission lifetime and current stability of CNF grown on blank TiW substrates was studied using the diode sample assembly. The 6 mm wide copper anode, electrically grounded and cooled by a chiller with a fixed temperature of  $-3.5^\circ\text{C}$ , was laid orthogonally above the long axis of the CNF sample in the assembly. The aligned CNF thin film was prepared on a blank TiW substrate under the CNF synthesis parameters introduced in Sec. 3.3 with a width of 6.8 mm. The test was conducted for twenty-two



hours by continuously applying a constant -2800V to the sample. The emission current versus time was recorded and shown in Figure 3.12. The emission current drops very dramatically from 4.6 mA to 0.7 mA in the first four hours. Then the emission current decreases at a lower rate from 0.7 mA to 0.3 mA in the next ten hours. Thereafter, the emission current remained around 0.3 mA for the rest of the test period. A drop in current of ~96.5% occurred during the total testing period.

The emission lifetime is defined here as the operation period within which an emission current of more than 1 mA is sustained. Consequently, the lifetime of CNF grown on blank TiW substrates is only ~3.1 hours, which is insufficient for device operation. Moreover, random data points and spikes observed in the figure are suspected

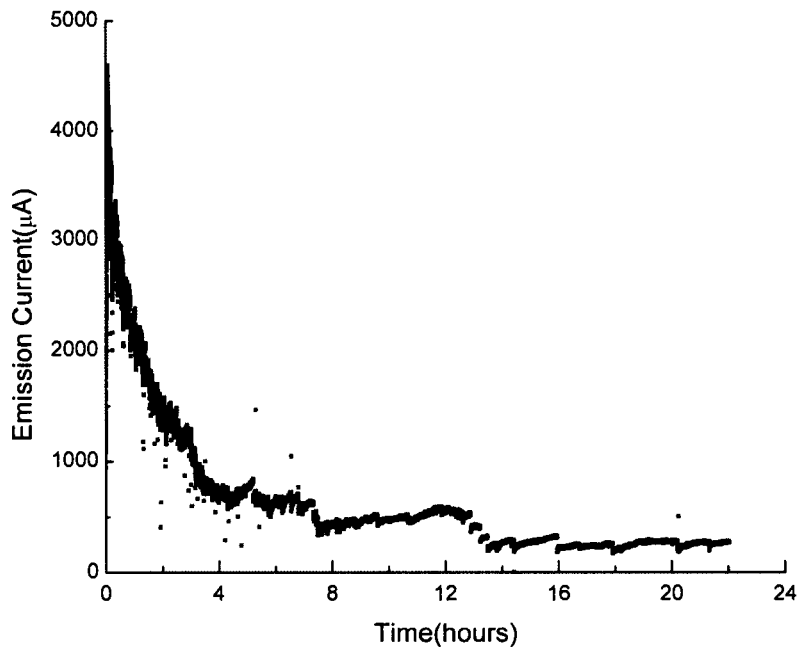


Figure 3.12 Emission current of CNF grown on blank TiW substrates as a function of time operated in a dc mode.

to be caused by arcing that occurred on the surface of the sample.

### 3.9 FIELD EMISSION OF CNF BASED BACK GATE TRIODE DEVICES

To test the validation of back gate triode devices, they were measured in a diode and a triode mode by using the 24-pin header assembly. Representative I-V characteristics of an aligned CNF-based back-gated triode device are demonstrated in Figure 3.13. A  $2.3\text{mm} \times 2.7\text{mm}$  area of the part of the device was measured in a diode configuration, and the same region was then tested in a triode configuration. The diode test result shown in Fig. 3.13(a) indicates that the turn-on field of aligned CNF synthesized on TiW crests in the back-gated triode structure is  $7.45\text{ V}/\mu\text{m}$ , which is much lower than that measured using aligned CNF grown on blank TiW substrates. We believe that the pronounced decrease in turn-on field can be attributed to the profile of the TiW lines which yield a reduced electrostatic screening by neighboring CNF on those that remain on the tops of the well-separated lines. In the diode configuration a total emission current of  $81\ \mu\text{A}$  was measured at  $10\text{ V}/\mu\text{m}$ . To test the device in the triode configuration, a  $7.3\text{ V}/\mu\text{m}$  electric field was applied between the anode and the cathode, slightly lower than the turn-on field of CNF measured in the diode configuration. At this applied field, the aligned CNF yield only  $0.8\ \mu\text{A}$  of emission current when no back gate voltage is applied, see Fig. 3.13(b). When the back gate voltage increases from  $0\text{V}$  to  $+80\text{V}$ , the measured emission current in the triode configuration increases non-linearly. At a back gate voltage  $80\text{V}$ , an observed emission current of  $267\ \mu\text{A}$  was obtained for a diode field of  $7.3\text{ V}/\mu\text{m}$ . Therefore, the validation of the back-gated triode device has been confirmed by the test above.

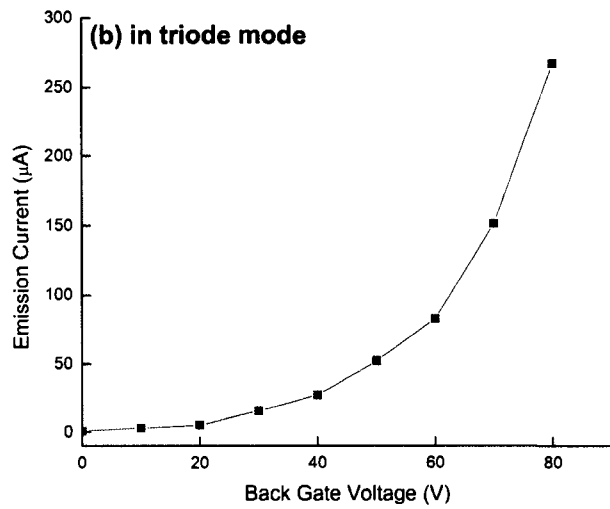
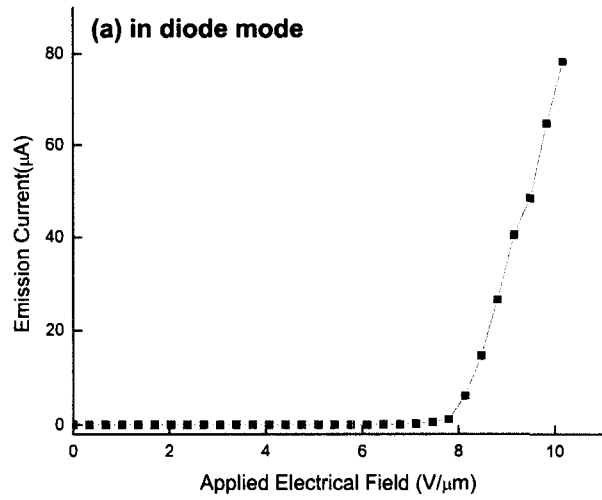


Figure 3.13  $I$ - $V$  characteristics of aligned CNF based back gate device, (a) in a diode mode, (b) in a triode mode.

### 3.10 SUMMARY

We have directly synthesized spaghetti-like and aligned CNF directly on blank TiW substrates without using a buffer layer by DC PECVD. We are able to control the degree of alignment of the resulting CNF by variation of plasma power, with spaghetti-like CNF, having a high degree of nanoscale graphitic ordering growing at lower power, and aligned CNF, having a higher degree of nanoscale disorder, growing at higher plasma powers. The morphology of CNF synthesized on blank TiW substrates is determined by the electric field generated in the plasma sheath and the growth rate of CNF, which can be tuned by the plasma power. The field emission properties of carbon nanofibers grown on blank TiW substrates are also measured using the cartridge holder assembly.

We have also described a process to fabricate both spaghetti-like and aligned CNF on TiW lines of controlled cross-sectional profiles to create back gate field emission triodes. However, only aligned CNF based back gate triode device survive our present post-processing wet-cleaning steps that are necessary to remove amorphous carbon from the dielectric layer. Devices using under-dense coatings of aligned CNF as cathodes in back gate triode device were tested for diode and triode field-emission operation indicating that back gate triode operation yield greatly enhanced performance.

### References for Chapter III

- [1] Melechko AV, Merkulov VI, McKnight TE, Guillorn MA, Klein KL, Lowndes DH, Simpson ML. Vertically aligned carbon nanofibers and related structures: Controlled synthesis and directed assembly. *Journal of Applied Physics*. 2005;97(4):041301-39.
- [2] Sherman A. *Chemical Vapor Deposition for Microelectronics*. Park Ridge: Noyes Publications 1988.
- [3] Chhowalla M, Teo KBK, Ducati C, Rupesinghe NL, Amaratunga GAJ, Ferrari AC, Roy D, Robertson J, Milne WI. Growth process conditions of vertically aligned carbon nanotubes using plasma enhanced chemical vapor deposition. *Journal of Applied Physics*. 2001;90(10):5308-17.
- [4] Mauger M, Binh VT, Levesque A, Guillot D. Freestanding vertically aligned arrays of individual carbon nanotubes on metallic substrates for field emission cathodes. *Applied Physics Letters*. 2004;85(2):305-7.
- [5] Cao A, Ci L, Li D, Wei B, Xu C, Liang J, Wu D. Vertical aligned carbon nanotubes grown on Au film and reduction of threshold field in field emission. *Chemical Physics Letters*. 2001;335(3-4):150-4.
- [6] Zhu M, Wang J, Outlaw RA, Hou K, Manos DM, Holloway BC. Synthesis of carbon nanosheets and carbon nanotubes by radio frequency plasma enhanced chemical vapor deposition. *Diamond and Related Materials*. In Press, Corrected Proof.
- [7] Rao AM, Jacques D, Haddon RC, Zhu W, Bower C, Jin S. In situ-grown carbon nanotube array with excellent field emission characteristics. *Applied Physics Letters*. 2000;76(25):3813-5.
- [8] Saito Y, Uemura S. Field emission from carbon nanotubes and its application to electron sources. *Carbon*. 2000;38(2):169-82.
- [9] Bonard J-M, Croci M, Klinke C, Kurt R, Noury O, Weiss N. Carbon nanotube films as electron field emitters. *Carbon*. 2002;40(10):1715-28.
- [10] Baughman RH, Zakhidov AA, de Heer WA. Carbon Nanotubes--the Route Toward Applications. *Science*, 2002;297(5582):787-92.
- [11] Temple D. Recent progress in field emitter array development for high performance applications. *Materials Science and Engineering: R: Reports*. 1999;24(5):185-239.
- [12] Tyler T, Shenderova OA, McGuire GE. Vacuum microelectronic devices and vacuum requirements. 2005: AVS; 2005. p. 1260-6.
- [13] Yu S, Yi W, Lee J, Jeong T, Jin S, Heo J, Kang JH, Choi YS, Lee CS, Yoo JB, Kim JM. Energy distribution for undergate-type triode carbon nanotube field emitters. *Applied Physics Letters*. 2002;80(21):4036-8.
- [14] Mammana VP, Fonseca LRC. Reduction of the number of electrons emitted backwards in back-gated devices for field emission: A theoretical study. *Applied Physics Letters*. 2004;85(5):834-6.
- [15] Choi YS, Kang JH, Park YJ, Choi WB, Lee CJ, Jo SH, Lee CG, You JH, Jung JE, Lee NS, Kim JM. An under-gate triode structure field emission display with carbon nanotube emitters. *Diamond and Related Materials*. 2001;10(9-10):1705-8.
- [16] Mammana VP, Jaeger D, Shenderova O, McGuire GE. Field emission device with back gated structure. *Journal of Vacuum Science & Technology A: Vacuum, Surfaces, and Films*. 2004;22(4):1455-60.

- [17] Lieberman MA, Lichtenberg AJ. Principles of plasma discharges and materials processing. 1st ed. NY: Wiley-Interscience 1994.
- [18] Bower C, Zhu W, Jin S, Zhou O. Plasma-induced alignment of carbon nanotubes. *Applied Physics Letters*. 2000;77(6):830-2.
- [19] Merkulov VI, Melechko AV, Guillorn MA, Lowndes DH, Simpson ML. Alignment mechanism of carbon nanofibers produced by plasma-enhanced chemical-vapor deposition. *Applied Physics Letters*. 2001;79(18):2970-2.
- [20] Wang S, Wang J, Miraldo P, Zhu M, Outlaw R, Hou K, Zhao X, Holloway BC, Manos D, Talmage T, Shenderova O, Mark R, Dalton J, McGuire G. High field emission reproducibility and stability of carbon nanosheets and nanosheet-based backgated triode emission devices. *Applied Physics Letters*. 2006;89(18):183103-3.
- [21] Tyler T, Shenderova O, Ray M, Dalton J, Wang J, Outlaw R, Zhu M, Zhao X, McGuire G, Holloway BC. Back-gated milliamper-class field emission device based on carbon nanosheets. *Journal of Vacuum Science & Technology B: Microelectronics and Nanometer Structures*. 2006;24(5):2295-301.
- [22] Dresselhaus MS, Dresselhaus G, Saito R, Jorio A. Raman spectroscopy of carbon nanotubes. *Physics Reports*. 2005;409(2):47-99.
- [23] David BH, Martin SB, Kenneth BKT, Brett AC, William IM, Meyyappan M. An investigation of plasma chemistry for dc plasma enhanced chemical vapour deposition of carbon nanotubes and nanofibres. *Nanotechnology*. 2005;16(6):925.
- [24] Teo KBK, Hash DB, Lacerda RG, Rupesinghe NL, Bell MS, Dalal SH, Bose D, Govindan TR, Cruden BA, Chhowalla M, Amaratunga GAJ, Meyyappan M, Milne WI. The Significance of Plasma Heating in Carbon Nanotube and Nanofiber Growth. *Nano Lett*. 2004;4(5):921-6.
- [25] Helveg S, Lopez-Cartes C, Sehested J, Hansen PL, Clausen BS, Rostrup-Nielsen JR, Abild-Pedersen F, Norskov JK. Atomic-scale imaging of carbon nanofibre growth. *Nature*. 2004;427(6973):426-9.
- [26] Fowler RH, Nordheim LW. *Proc R Soc London, Ser A*. 1928:119-73.
- [27] Nilsson L, Groening O, Groening P, Kuettel O, Schlapbach L. Characterization of thin film electron emitters by scanning anode field emission microscopy. *Journal of Applied Physics*. 2001;90(2):768-80.
- [28] Groning O, Kuttel OM, Emmenegger C, Groning P, Schlapbach L. Field emission properties of carbon nanotubes. *Journal of Vacuum Science & Technology B: Microelectronics and Nanometer Structures*. 2000;18(2):665-78.

## CHAPTER IV

### FIELD EMISSION PROPERTIES OF CARBON NANOSHEETS

#### 4.1 INTRODUCTION

This chapter presents the synthesis, structure, and field emission properties of carbon nanosheets (CNS) grown on Si substrates by radio frequency plasma enhanced chemical vapor deposition (RF PECVD), and their applications in back gate triode devices. A detailed study on the field emission behavior of CNS is also presented.

Two-dimensional carbon nanostructures, consisting of several graphene layers, are usually hundreds of nanometers in height and length, but only a few nanometers in thickness. The synthesis of graphitic sheets can be traced back to the beginning of this century. However, it was not until 1997 when Ando et al [1] reported the existence of petal-like graphitic sheets in the soot of carbon nanotubes prepared by arc discharge that the synthesis of graphitic sheets started being studied. Since then, many methods to fabricate graphitic sheets have been developed by various research groups.

Shang et al [2] reported that the synthesis of carbon nanoflakes that are 10-20 nm in thickness could be achieved by hot filament plasma enhanced chemical vapor deposition (HFCVD). They also presented the field emission performance of these nanoflakes, indicating that the turn-on field is 17 V/ $\mu\text{m}$ . Wang et al [3] deposited nano-carbon films with about 10 nm in thickness on Si substrates by microwave plasma assisted chemical vapor deposition (MPCVD). From these films, they obtained a current density of

20 mA/cm<sup>2</sup> at an applied electric field of 10 V/μm, but the field emission characteristic of these films did not follow the linear relationship predicted by the Fowler-Nordheim theory.

Chen et al [4], and Shang et al [5] also fabricated carbon nanoflakes and nanowalls using MPCVD while Hiramatsu et al [6] synthesized carbon nanowalls by capacitively coupled radio frequency plasma enhanced chemical vapor deposition (RFCVD) assisted by hydrogen radical injection. Kurita et al [7] were the first to grow carbon nanowalls by direct current plasma enhanced chemical vapor deposition (DC PECVD). All these graphitic sheets were vertically oriented relative to their substrates and were hundreds of nanometers in thickness. No evidence of these graphitic sheets thinner than 5 nm were presented.

Novoselov et al [8, 9] and Zhang et al [10] fabricated atomically thin carbon films by mechanical exfoliation, and Berger et al [11, 12] synthesized ultrathin epitaxial graphite films on SiC substrates through thermal decomposition in vacuum. Berger et al also studied electronic properties of these graphitic sheets. Their measurements indicate that a current density of  $\sim 10^8$  A/cm<sup>2</sup>, roughly two orders of magnitude greater than copper, can be carried by these graphitic sheets. Chemical stability, inertness, and crystallinity of graphitic sheets under ambient conditions have also been confirmed in their works. Instead of standing vertically on the substrates, these atomically thin carbon films lie down on the substrate surface.

Our group has presented a way to prepare graphitic sheets, called carbon nanosheets, by inductively coupled radio frequency plasma enhanced chemical vapor deposition [13-21]. Our nanosheets are less than 4 nm in thickness, free of catalysts, and



free-standing (on edge) approximately normal to the growth surface. We have succeeded in regularly depositing CNS on four-inch substrates, a substrate size compatible with conventional device processing techniques used in semiconductor industries. Therefore, the application of carbon nanosheets may expand to a variety of devices. Among them, CNS based field emission devices have been developed by our group in last few years.

The CNS is a promising candidate as the electron source in the application of field emission devices due to its atomic scale edge structure, high purity, and uniform height distribution [15, 19]. Previous field emission tests on CNS show that their field emission properties are at least equivalent to, or better than, the field emission properties of carbon nanotubes and nanofibers. This chapter presents a systematic study of the field emission properties of CNS by examining various characteristics, including turn-on field and threshold field, maximum total current, current density, lifetime in a slow pulse mode, lifetime in a dc mode, and emission uniformity. These test results have lead to an advanced understanding of the field emission behavior of CNS.

## 4.2 RADIO FREQUENCY PLASMA ENHANCED CHEMICAL VAPOR DEPOSITION (RFCVD) APPARATUS

Here, we describe the radio frequency plasma enhanced chemical vapor deposition (RFCVD) apparatus used for CNS synthesis. Unlike the DC PECVD apparatus used for CNF synthesis in Sec. 3.2, the plasma in a RFCVD is generated by applying the rf power to a planar coil and coupling the power through a dielectric window. Depending on the mechanism of power coupling, RFCVD is able to operate under two modes, the capacitively coupled mode or the inductively coupled mode. The plasma density of

inductively coupled plasma is usually in the order of  $10^{11} \text{ cm}^{-3}$ , 10 times higher than that of capacitively coupled plasma. In this work, we used inductively coupled plasma to synthesize carbon nanosheets. Principles followed to design our RFCVD apparatus can be found elsewhere [22].

A schematic of the RFCVD apparatus is displayed in Figure 4.1. The apparatus is built upon a grounded stainless steel chamber equipped with a mechanical pump and a turbo molecular pump, creating a base pressure of  $\sim 10^{-6}$  Torr. A quartz window polished on both faces, with a thickness of 1.27 cm, lies on top of the chamber. This window works as a dielectric medium for the power transfer from the rf coil antenna to the plasma.

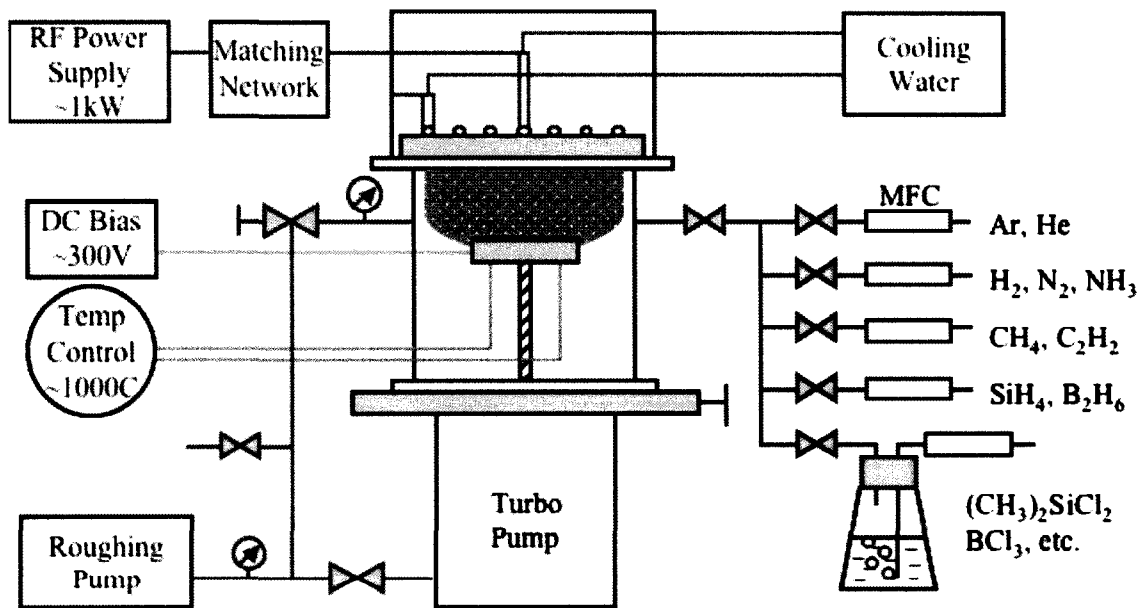


Figure 4.1 Schematics of RFCVD apparatus.

A 13.56 MHz RF power up to 1100W is coupled into the RFCVD apparatus through a 3-turn planar-coil antenna above the window housed in an aluminum top-hat used to prevent RF radiation leaks. A matching box containing two variable vacuum capacitors is connected between the RF power supply and the antenna in order to tune the operation mode of the plasma.

A commercial four-inch GE ceramic heater serves as the sample stage, whose distance to the quartz window can be adjusted from 3 cm to 10 cm. The heater allows the substrate temperature to reach  $\sim 1200$  °C, higher than the temperature required for CNS deposition. Gases, including Ar, He, N<sub>2</sub>, NH<sub>3</sub>, H<sub>2</sub>, CH<sub>4</sub>, and C<sub>2</sub>H<sub>2</sub>, are introduced into the chamber by separate mass flow controllers. A photograph of the RFCVD apparatus is shown in Figure 4.2.

#### 4.3 DEPOSITION OF CARBON NANOSHEETS

By using the RFCVD apparatus, carbon nanosheets have been successfully deposited on a variety of substrates including Si, Al<sub>2</sub>O<sub>3</sub>, SiO<sub>2</sub>, Ni, Ti, W, TiW, Mo, Cu, Au, Pt, Zr, Hf, Nb, Ta, Cr, 304 stainless steel, and graphite. Results of the parametric studies on CNS deposition can be found elsewhere [22]. Here, we briefly describe the standard CNS deposition conditions used in this chapter.

A four-inch, heavily-doped Si wafer (resistivity of 0.003-0.005  $\Omega\cdot\text{cm}$ ) is loaded on the sample stage (the four-inch heater) before the RFCVD apparatus is pumped down to  $\sim 1$  mTorr. H<sub>2</sub> is first introduced into the system at 6 sccm while the substrate is heated up to  $\sim 700$  °C, where it is held for at least 30 minutes to ensure uniform heating. Then, CH<sub>4</sub> is added to the chamber at 4 sccm and the apparatus pressure is stabilized at  $\sim 100$  mTorr,

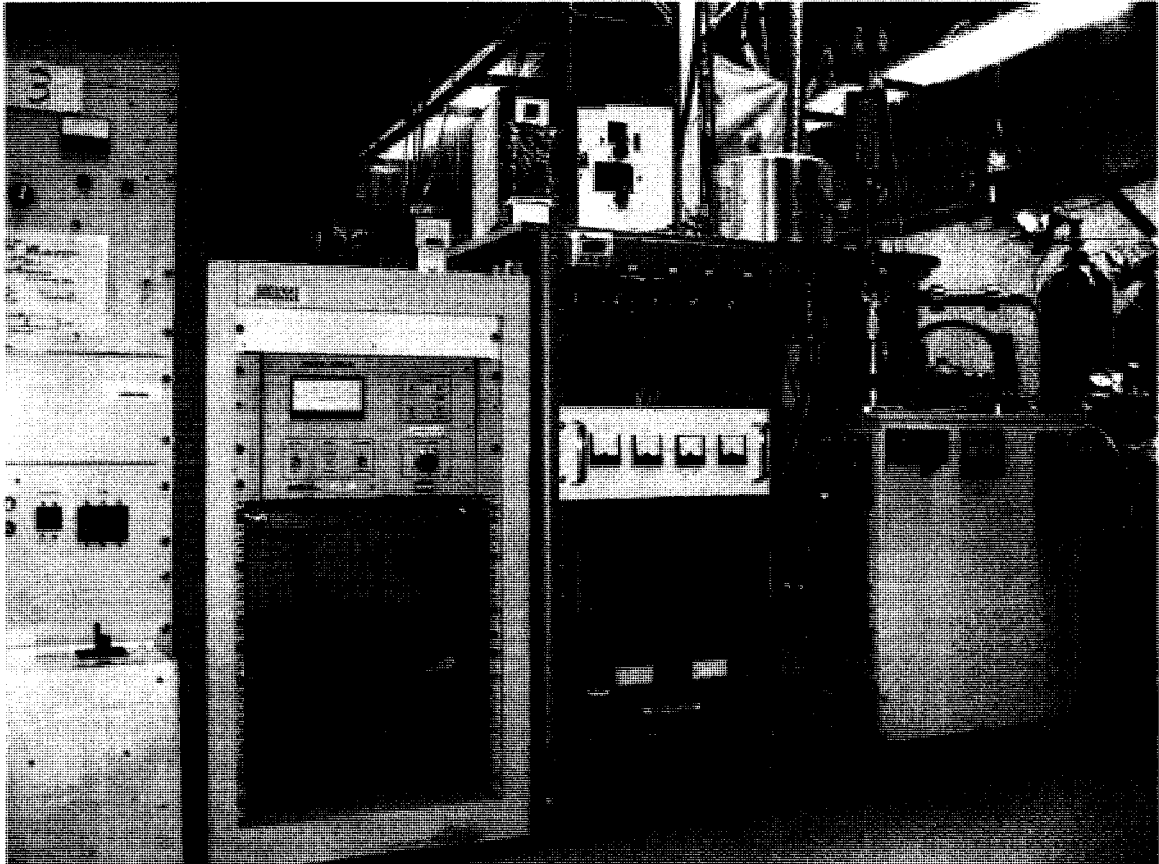


Figure 4.2 A picture of the RFCVD apparatus.

An RF plasma is ignited and tuned as the power is increased to 900W over the course of about one minute. Thereafter, the deposition is conducted for twenty minutes. The apparatus is cooled down for at least 30 minutes in a hydrogen atmosphere before the sample is taken out.

#### 4.4 CHARACTERIZATION OF CARBON NANOSHEETS

Carbon nanosheets have been measured by our group using a variety of materials characterization methods, including scanning electron microscopy (SEM), transmission

electron microscopy (TEM), Auger electron spectroscopy (AES), X-ray photoelectron spectroscopy (XPS), particle induced X-ray emission (PIXE), elastic recoil detection analysis (ERDA), thermal desorption spectrometry (TDS), Raman spectroscopy, Fourier transform infrared (FTIR) spectrometer, X-ray diffraction (XRD), and Brunauer-Emmett-Teller (BET) surface area measurements. The results have been described elsewhere in detail [22]. Below we summarize some of these observations.

AES and XPS measurements of CNS detect only C. Since no catalysts are used, there is no source of contamination except possible sputtering from the chamber wall of the window, which appears not to occur. PIXE, ERDA, and TDS further confirm that carbon nanosheets are catalyst free and contamination free except for the presence of hydrogen. XRD results prove that CNS are crystalline graphitic structures with some defects. BET measurements suggest that the specific area of typical CNS is  $1086 \pm 194$   $\text{m}^2/\text{g}$ , consistent with the theoretical calculation of the surface area of double- and triple-layered graphite sheets. SEM, TEM, and Raman measurements will be more thoroughly discussed below.

SEM images of typical CNS grown under standard deposition conditions are shown in Figure 4.3. The top view image, Fig. 4.3(a), shows the representative CNS is less than 4 nm thick and  $\sim 1000$  nm long with a smooth surface topology and a corrugated nature, standing roughly vertical to the substrate. The high magnification image, Fig. 4.3(b), indicates the thickness of an individual CNS edge is  $\sim 1$  nm, and may be even thinner (limited by the SEM resolution). The cross-section image, Fig. 4.3(c), shows that the average height of CNS is  $\sim 800$  nm, corresponding to a growth rate of 40 nm/min. Moreover, the standard deviation in the height for the whole sample surface, in Fig.

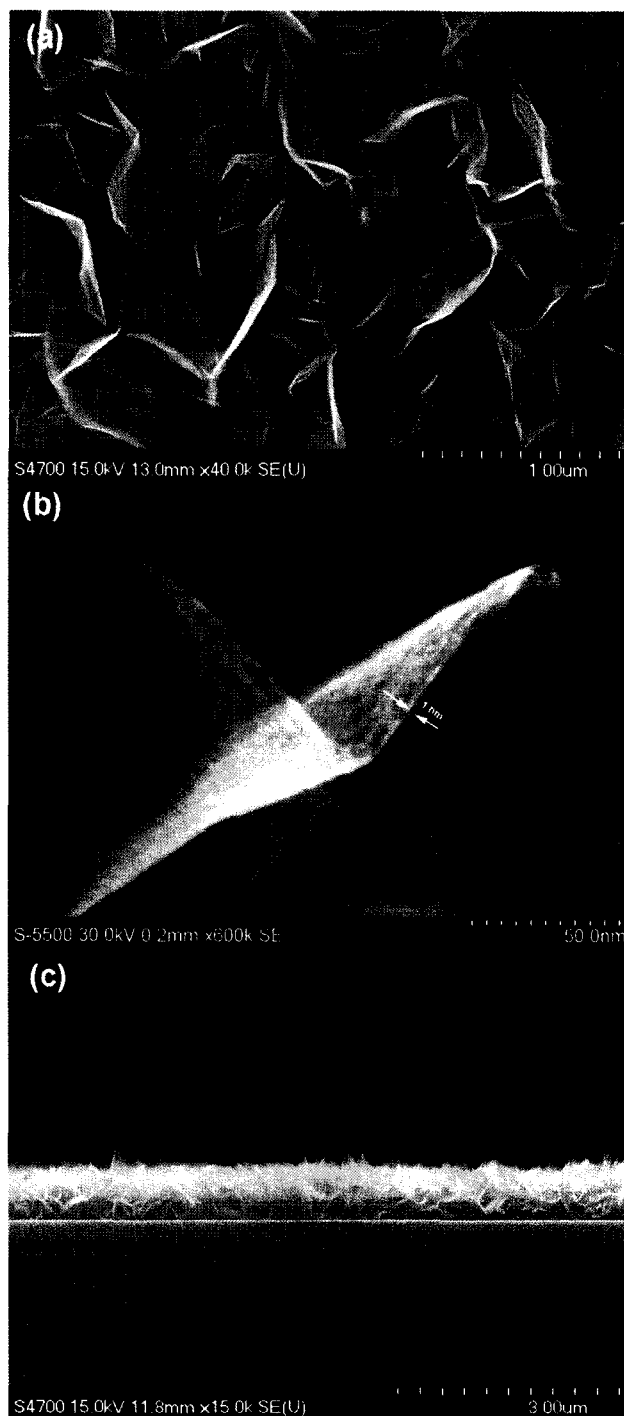


Figure 4.3 SEM images of representative nanosheets fabricated with the standard CNS deposition conditions. (a) Top-view image, (b) high magnification image, (c) cross-section view image.

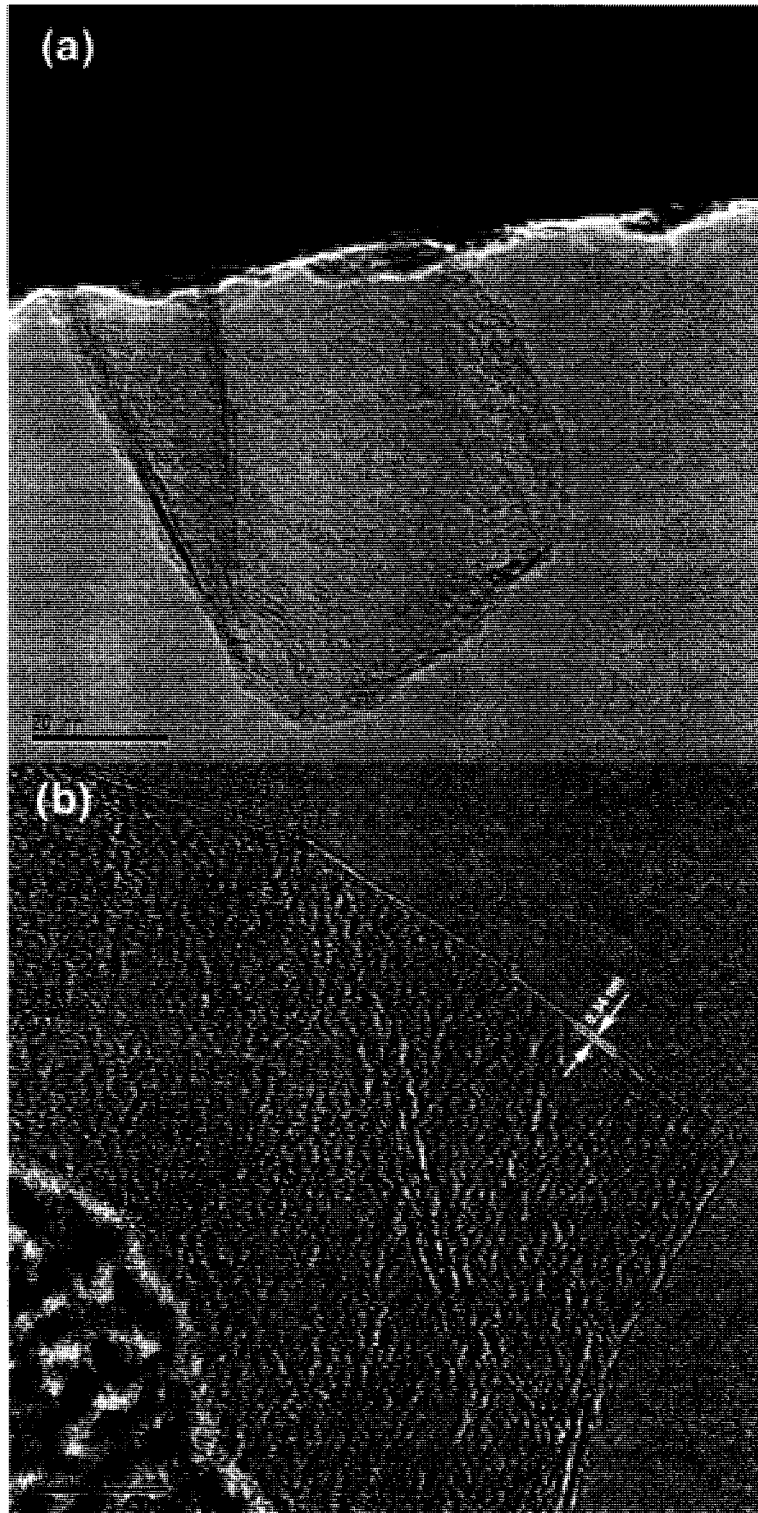


Figure 4.4 (a) TEM image of CNS grown on a grid, (b) HRTEM image of a piece of CNS.

4.3(c), is less than 10%. Therefore, the aspect ratio of CNS edges, defined by dividing the height of a CNS to its thickness, is on the order of  $\sim 800$ .

HRTEM images of representative CNS deposited directly on a Ni TEM grid under standard deposition conditions are displayed in Figure 4.4. The low magnification image shown in Fig. 4.4(a) reveals CNS growth vertical to the grid surface. The HRTEM image in Fig. 4.4(b) displays the cross section of a portion of the planar nanosheet that has rolled back over itself. Two parallel fringes (marked by arrows) with a distance of 0.34 nm are found at the edge of this nanosheet. The spacing between these two fringes is close to the (002) spacing of graphite, 0.335 nm, so we can see that this CNS consists of only two graphene layers. Nanosheets having one or two graphene layers at their edges have been routinely observed.

Raman spectrum of nanosheets is presented in Figure 4.5. Four major peaks are found in the spectrum: one peak is located at  $1350\text{ cm}^{-1}$  representing a disorder-induced D peak, the second peak is located at  $1580\text{ cm}^{-1}$  and indicates a tangential-mode G peak of superfine graphite, the third peak is located at  $1620\text{ cm}^{-1}$  representing a D' shoulder frequently seen in microcrystalline graphite, and the fourth peak is located at  $2700\text{ cm}^{-1}$  and represents overtone of the D peak [23, 24]. Second order Raman peaks, including the overtone of D' band and the combination of D and G band, are also observed in the range of  $2000\text{-}3500\text{ cm}^{-1}$ . Further, peaks representing radial breathing modes were found in the range of  $220\text{ to }360\text{ cm}^{-1}$  [16]. The sharp D and G peaks indicate the defective, crystalline nature of carbon nanosheets. The defects may include vacancies, "grain" boundaries, and distortions in graphene sheets that cause the nonuniformity, corrugation, and twisting of nanosheets. The intensity ratio of the D peak to the G peak,  $I_D/I_G$ , is used to evaluate the



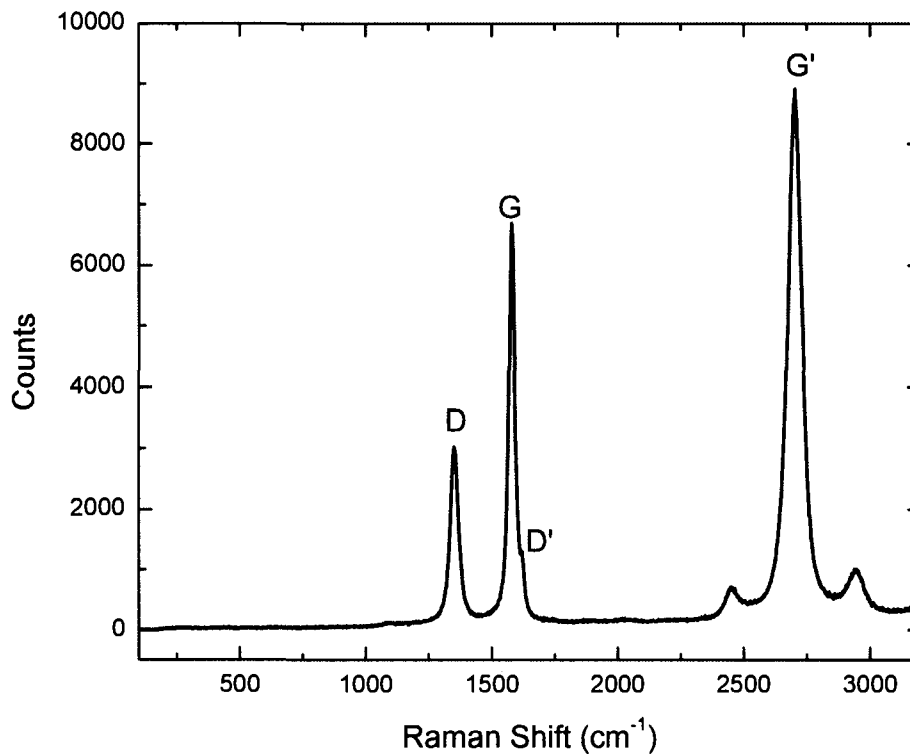


Figure 4.5 Raman spectrum of a typical CNS sample using a 514 nm excitation laser wavelength.

degree of disorder in nanosheets. The method used to calculate the intensity ratio of the D peak to the G peak follows the principle applied in Sec. 3.4, which uses the respective peak areas for calculating. In the case of the spectrum displayed here,  $I_D/I_G$  is  $\sim 0.6$ . This intensity ratio is quite representative of CNS.

#### 4.5 FIELD EMISSION PROPERTIES OF CARBON NANOSHEETS

Even though CNS have the same sharp atomic edge as CNF or CNT, the field emission properties of CNS have not yet been fully studied. Some key questions affecting

the field emission performance of CNS have not been answered, in particular, how uniform their emission is, how stable it is over time, and what physical attributes govern these properties. In order to further improve the engineering performance, the field emission behavior of CNS must be examined from various perspectives, including turn-on field, maximum total current, emission lifetime, and emission uniformity.

Field emission properties of CNS are measured in an UHV chamber with a base pressure of  $\sim 1 \times 10^{-10}$  Torr. The diode holder assembly is used through all tests presented in the following sections. A CNS sample is used as the cathode in the assembly and separated from a 6 mm wide copper anode with a distance of 254  $\mu\text{m}$ . The long axis of the copper anode is laid orthogonally above the long axis of the CNS sample. The anode is cooled to less than 0 °C throughout the measurements. The CNS sample is biased by a programmable high voltage power supply and the emission current is automatically collected using a picoammeter.

#### 4.5.1 TURN-ON FIELD AND THRESHOLD FIELD

Both turn-on field and threshold field represent the applied electric field required to initiate electron emission from emitters. Lower values of turn-on and threshold field yield better emission performances of emitters. The turn-on and threshold field are arbitrarily defined values on the basis of the specific application. In this section, the turn-on field is defined as the applied electric field at which a total emission current of 10 nA is obtained. The threshold field is the applied electric field at which a current density of 10  $\mu\text{A}/\text{cm}^2$  is measured. Many factors, such as the test method used, details of the test apparatus and sample holder, sample manipulation, and sample size, affect these test results, so

statistical averages of large numbers of tests are required. Since the sample size has a great impact on the measured emission current and the threshold field of CNS is defined in a way to minimize the effect of the sample size on the test results, we suggest here that the threshold field is a more accurate parameter to determine the field emission characteristics of CNS than the turn-on field. Turn-on and threshold field of CNS were recorded as soon as nanosheets first time emitted electrons in this work so that temporal variation of the material was minimized.

Twenty-six pairs of turn-on field and threshold field of CNS were collected from 26 individual experiments using CNS samples made in 10 separate runs of CNS deposition.

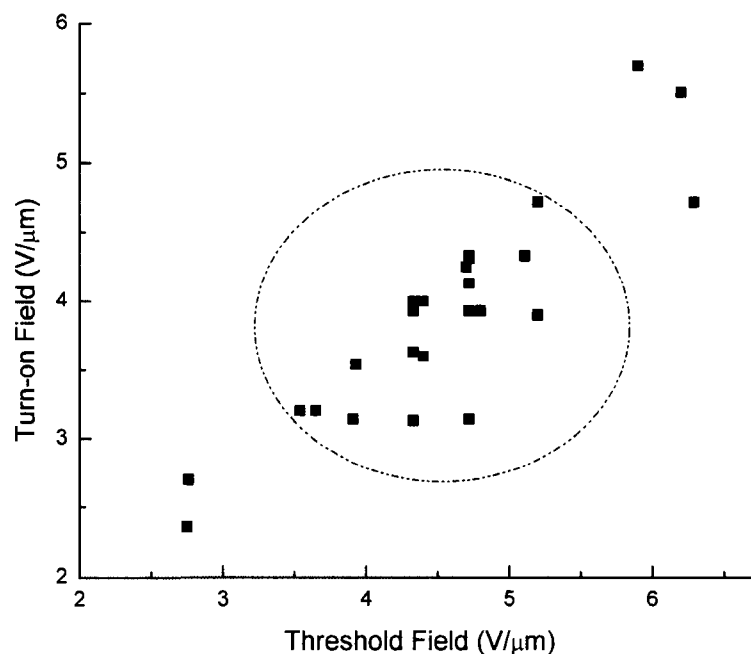


Figure 4.6 Turn-on fields of CNS samples as a function of their threshold fields, revealing that the turn-on and threshold field of a typical nanosheet lie in the range from 3 to 4.7 V/μm and 3.5 to 5.2 V/μm, respectively.

A plot of turn-on field vs threshold field is shown in Figure 4.6. Two CNS samples had turn-on and threshold fields below 3 V/ $\mu\text{m}$ . Three CNS samples had turn-on fields larger than 4.7 V/ $\mu\text{m}$  and threshold fields larger than 5.7 V/ $\mu\text{m}$ . The rest had turn-on fields ranging from 3 V/ $\mu\text{m}$  to 4.7 V/ $\mu\text{m}$  and threshold fields varying from 3.5 V/ $\mu\text{m}$  to 5.2 V/ $\mu\text{m}$  (circled in the figure).

To compare CNS with other dimensional carbon materials, we summarize the test data of the threshold field of SWNT, MWNT, and diamond from the literature and the test data of CNS in Table 4.1. The comparison suggests that CNS have the same level of threshold field as 1-D carbon nanotubes and 3-D diamond.

#### 4.5.2 TOTAL CURRENT AND CURRENT DENSITY

Total current and current density are two relevant specifics to evaluate field emission properties of electron emissive materials. The average current density is determined by dividing the total current by the test area. Depending on test techniques,

Table 4.1 Threshold fields of carbon materials.

Dimensions	Carbon material	Threshold field (V/ $\mu\text{m}$ )
1-D	SWNT	0.9-4 [25]
	MWNT	3-21 [26]
2-D	CNS (this work)	3.5-5.2
3-D	Diamond	5-20 [27]

the test area can be calculated using either the cathode area or the anode area. For instance, Zhu et al [28] used an anode consisting of a molybdenum probe with a radius of  $\sim 250 \mu\text{m}$  to measure the emission current of single-walled carbon nanotubes thin film deposited on Si substrates in an UHV chamber. They calculated the effective test area on the basis of the radius of the anode probe to report their current density. Their number,  $4 \text{ A/cm}^2$ , is likely the highest current density ever detected from CNT or CNF thin film in the literature, but must be used with caution to project to device applications since the total current does not increase linearly with increasing sample area. Phenomena, such as field screening effect, outgassing induced arcing, and thermal effects, significantly degrade the total current so total currents over  $\sim 10 \text{ mA}$  are rarely found in the literature for CNT or CNF thin film cathodes. In this work, we calculate the current density by dividing the total current by the cathode area. Moreover, we emphasize the total current rather than the current density because the total current is the key parameter that determines device applications so long as the current density is high enough for a given application.

With the newly designed diode holder assembly and the cooling system added to the anode, total currents of more than  $20 \text{ mA}$  were achieved routinely from  $\sim 30 \text{ mm}^2$  test area of CNS samples while maintaining a useful current density of  $\sim 0.1 \text{ A/cm}^2$ . The peak current (highest total current) achieved in this work is shown in the data of Fig. 4.7(a) below, which plots emission current as a function of the applied electric field. At an applied field of  $26.8 \text{ V}/\mu\text{m}$ , a peak current of  $33 \text{ mA}$  was measured on a sample that had been intensively conditioned by repetitively ramping the voltage. The corresponding F-N plot is displayed in Figure 4.7(b), showing that this sample very closely follows the

prediction of the form of Fowler-Nordheim equation [29]. This relationship also suggests that the field emission of CNS is not saturated at this field value, but is limited by our test apparatus. Although the current density for this sample was only  $0.103 \text{ A/cm}^2$ , this material has achieved a current density of  $0.28 \text{ A/cm}^2$  when a small anode is used. Thus, although the current density limits of the material have not been rigorously established, and the physics of the limitation are as yet undetermined, the total current from CNS is still quite promising for device applications.

#### 4.5.3 LIFETIME IN A SLOW PULSE MODE

The emission stability and lifetime of emissive material is critical for device applications. Device operations require emitters producing high current for thousands of hours without significant current degradation. However, it is difficult for nanotubes and diamonds to achieve stable electron emission when the current level is in the milliamperere range.

The emission stability and lifetime of CNS can be studied in a slow pulse mode by applying a series of identical voltage ramps over a long time period. Our previous results revealed that carbon nanosheets could operate at a maximum emission current of  $\sim 1.3 \text{ mA}$  with a duty factor of 14.9% for at least 200 hours in a slow pulse mode [15]. In this section, we present our latest measurements taken in this mode.

The CNS sample used here is 5.7 mm wide and fabricated by standard CNS deposition conditions as described in Sec. 4.3. The test is conducted with 23,379 voltage ramps over 200 hours, which yield a series of time-varying electric fields from 0 to  $23 \text{ V}/\mu\text{m}$ . As a result, the peak current of around 13 mA in one ramp is achieved at an

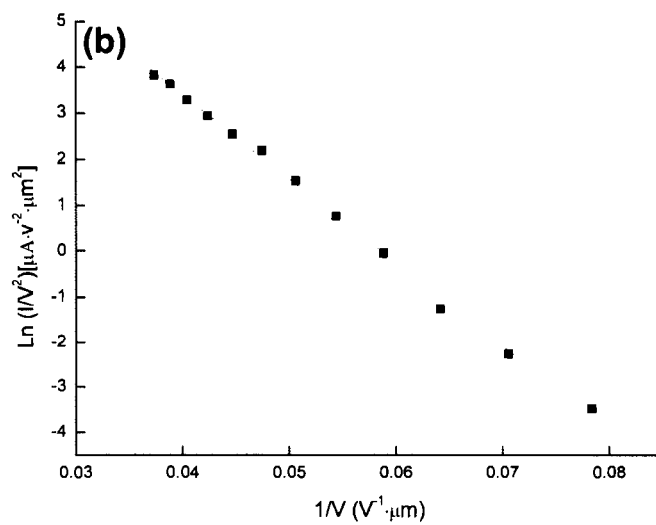
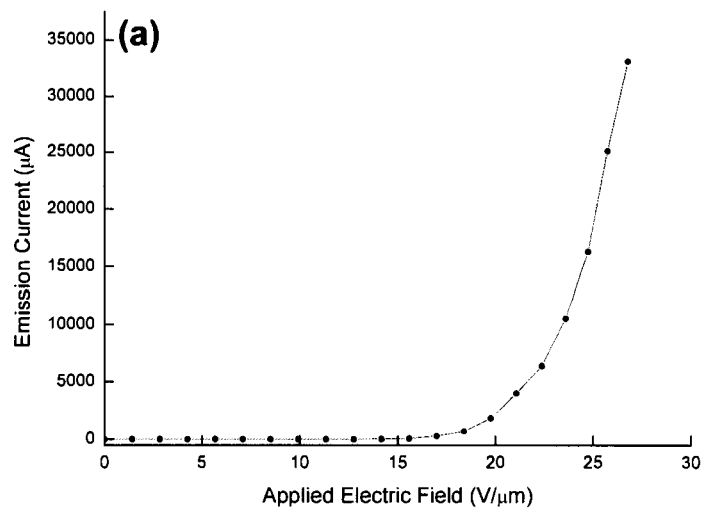


Figure 4.7 (a) Field emission current of a CNS sample as a function of the applied electric field, (b) its corresponding  $F$ - $N$  plot.

applied electric field of  $23 \text{ V}/\mu\text{m}$ . An illustration of two consecutive voltage ramps versus time is displayed in Figure 4.8, showing that each voltage ramp lasts 14 seconds followed by a 15 second rest (cooling off) period during which no bias is applied. The duration within which the emission current is larger than  $1 \mu\text{A}$  is 6.3 seconds in each voltage ramp. Consequently, the duty factor, defined as the ratio of the electron field emission time ( $>1 \mu\text{A}$ ) to the total duration of a testing sweep, is 21% in this case.

Field emission devices often do not need to operate with a duty factor of 100%. For instance, devices like field emission displays and microwave tubes operate with a 0.5% [30] and a 5% [31] duty factor, respectively. The test above was designed to satisfy such a practical device need.

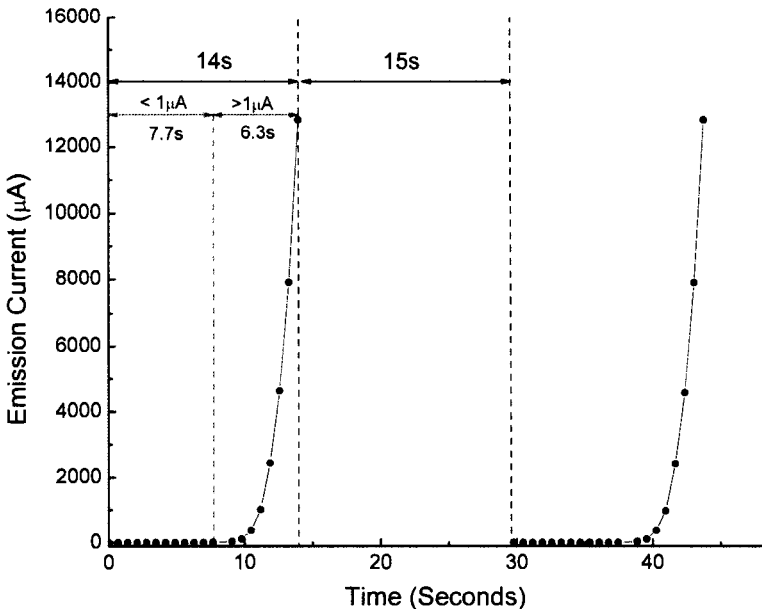


Figure 4.8 Two consecutive ramps versus time.



The peak current as a function of time in the first 98 hours is shown in Figure 4.9. The peak current is 18.46 mA in the first ramp, then rapidly decreases to 13.27 mA in the following half an hour, which is defined as the conditioning period. After conditioning, the peak current stabilizes at  $\sim 13$  mA for the remaining experiment period. During the stable emitting period, no significant current degradation is discovered and the standard deviation of the peak current is less than 2.1%. Although the emission is highly stable, we observed many current spikes that we attribute to the unstable ac line voltage in our building during the numerous electrical storms that occurred during these tests. Future tests will attempt to provide more stable filtered ac power.

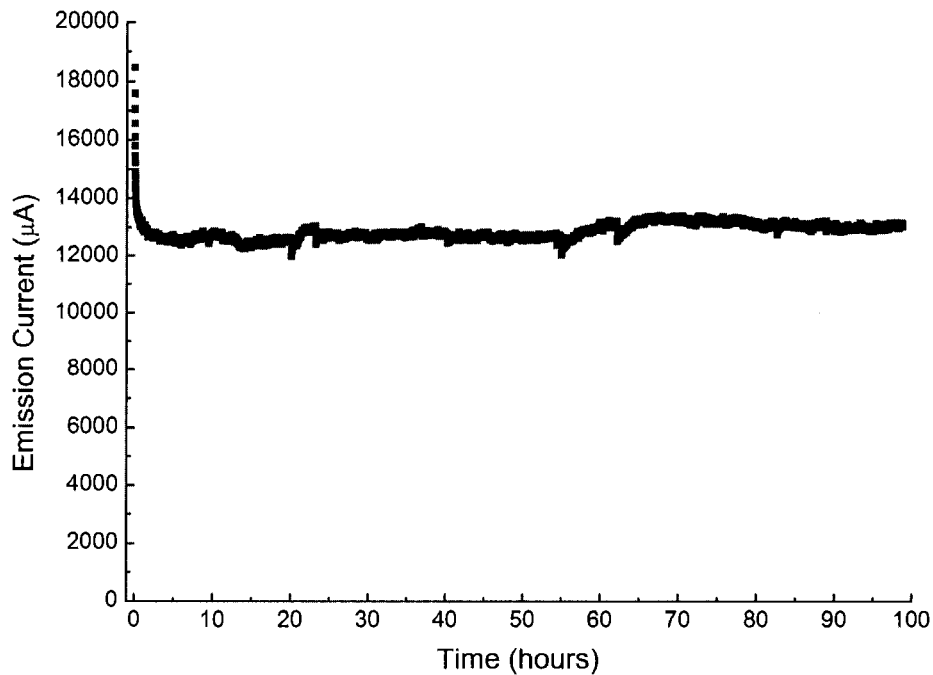


Figure 4.9 Peak current as a function of time in a slow pulse mode.

Characteristics of the emission current ( $I$ ) versus the applied electric field ( $V$ ) of the CNS sample are illustrated in Figure 4. 10. Eleven  $I$ - $V$  curves are recorded in Fig. 4.10(a) with their corresponding  $F$ - $N$  plots demonstrated in Fig. 4.10(b). These eleven  $I$ - $V$  curves were recorded every ten hours during the stable emission period with the first ramp measured after the CNS sample went through the conditioning period. The field required to generate a predetermined current does not significantly vary between each individual  $I$ - $V$  curve, indicating excellent emission stability and reproducibility of the CNS sample. The approximately linear relationship of corresponding  $F$ - $N$  plots indicates that CNS field emission properties follow the Fowler-Nordheim mechanism and the overlapping portions of the  $F$ - $N$  plots also indicate excellent emission stability and reproducibility of CNS.

The lifetime tests suggest that CNS can operate at more than 10 mA with a duty factor of 21% for a very long time.

#### 4.5.4 LIFETIME IN A DC MODE

We also investigated the emission stability and lifetime of CNS under dc operation by applying a continuous negative bias to the CNS sample. Thermal effects from dc operation often limit field emitters to operate at or below 1 mA, so such results are seldom reported in the literature.

For these tests, a CNS sample with a width of 5.3 mm was measured using the diode holder assembly and subjected to a constant negative 3400 V bias, which generated an applied electric field of 13.3 V/ $\mu$ m between the anode and the cathode. In order to mimic device operation environment, we did not bake the test apparatus before we started

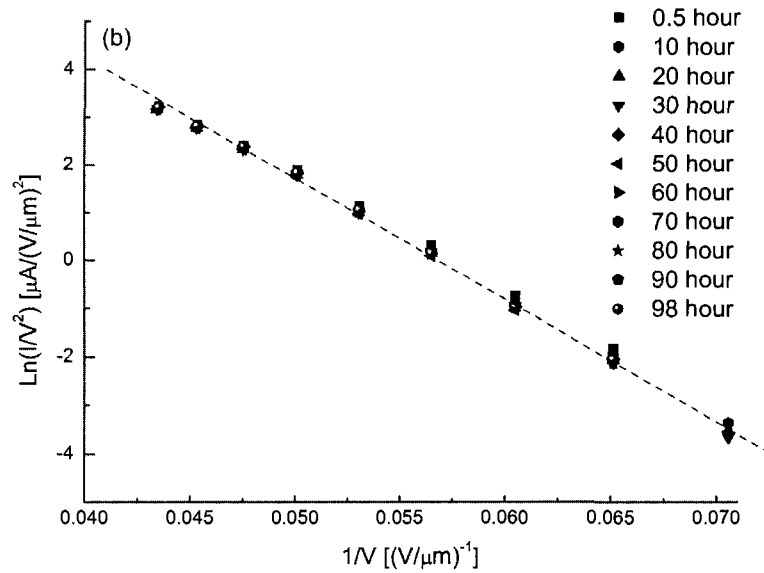
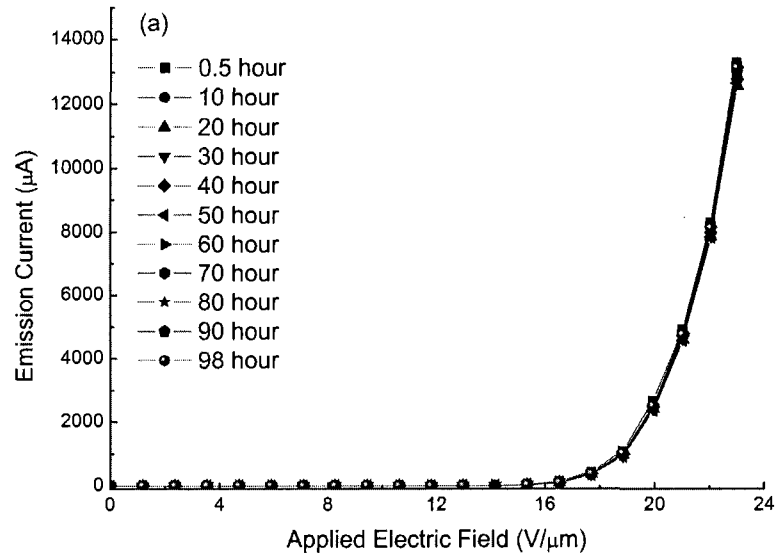


Figure 4.10 (a) Field emission currents recorded every ten hours in the stable emission period as a function of the applied electric field, (b) their corresponding  $F-N$  plots.

the test. For 203 hours, the emission current was collected and recorded every half a second by a picoammeter. In total, over one million current data points were collected during this test.

The emission current as a function of time is presented in Figure 4.11. The emission current started at 5.8 mA and quickly dropped to  $\sim 1.5$  mA during the conditioning period. Then, the emission current reached the stable emission period and maintained at  $\sim 1.5$  mA without significant degradation over the following 200 hours. Meanwhile, the chamber pressure increased from  $2 \times 10^{-7}$  Torr to  $2.3 \times 10^{-6}$  Torr as soon as the test started, then gradually decreased to  $6.5 \times 10^{-8}$  Torr at the end of the test. A statistical analysis of the

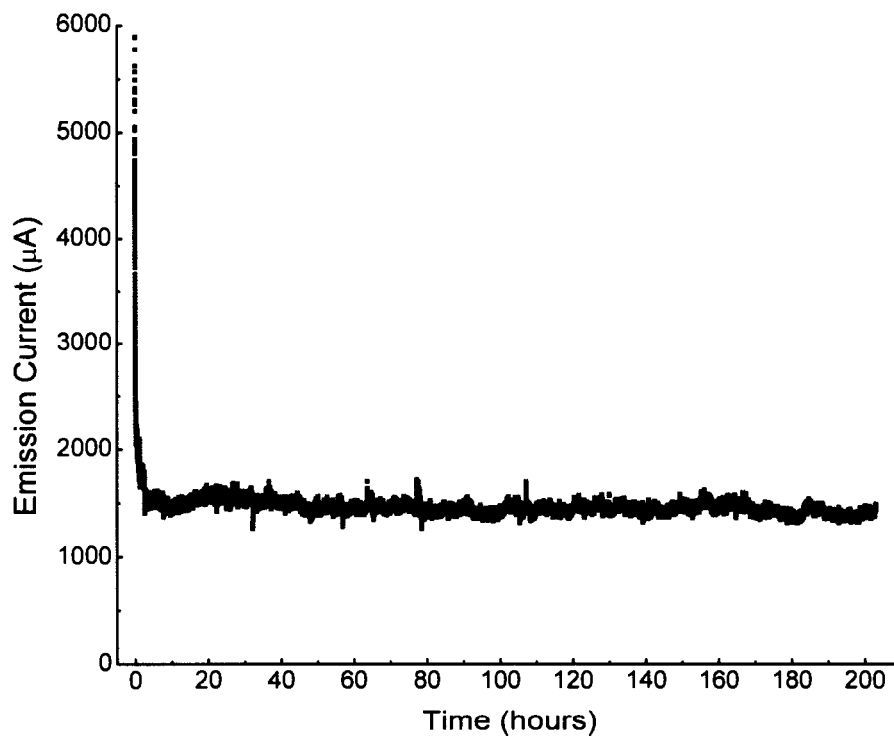


Figure 4.11 Field emission current as a function of time in dc mode.

200 hours of stable emission result reveals a mean emission current of 1.49 mA with a standard deviation of less than 3.6%. Two additional CNS samples have been tested above 1 mA in dc mode, also yielding similar stability.

These tests indicate that, unlike CNF samples that appear to last only a few hours at current near 1 mA, CNS is stable for a much longer time.

#### 4.6 STUDY ON FIELD EMISSION BEHAVIOR OF CNS

The study on field emission behavior of CNS is conducted by using  $I$ - $V$  curves and their corresponding  $F$ - $N$  plots collected immediately before and after the 203 hours dc lifetime test. Figure 4.12 illustrates these  $I$ - $V$  curves and corresponding  $F$ - $N$  plots. The  $I$ - $V$  curves, shown in Fig. 4.12(a), were recorded in nine consecutive sweeps by varying the applied negative bias from 0 to 3400 V to yield a time-varying series of applied electric field from 0 to 13.3 V/ $\mu$ m. Results reveal that  $I$ - $V$  curves after the lifetime test are as reproducible as those before the test. The peak currents measured at an applied electric field of 13.3 V/ $\mu$ m are 5.8 mA and 3.56 mA before and after the lifetime test, respectively. This peak current drop is consistent with the general observation of the emission current decrease during the conditioning process in Sec. 4.5.3 and 4.5.4. In addition, the threshold field increases from 6.9 V/ $\mu$ m to 8.1 V/ $\mu$ m after the lifetime test. The corresponding  $F$ - $N$  plots over the field emission range of these  $I$ - $V$  curves is shown in Fig. 4.12(b), displaying a linear relationship in close accord with the form of the Fowler-Nordheim equation. The slopes of  $F$ - $N$  plots before and after the lifetime test are -102.826 and -134.819, respectively.

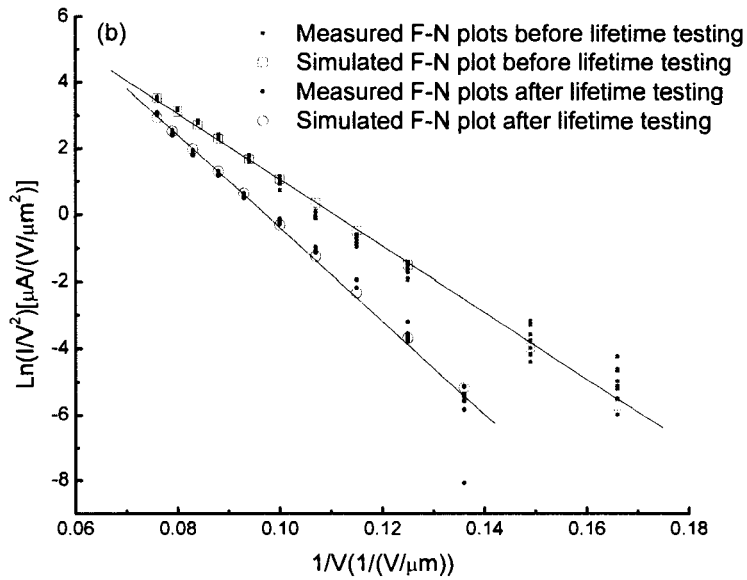
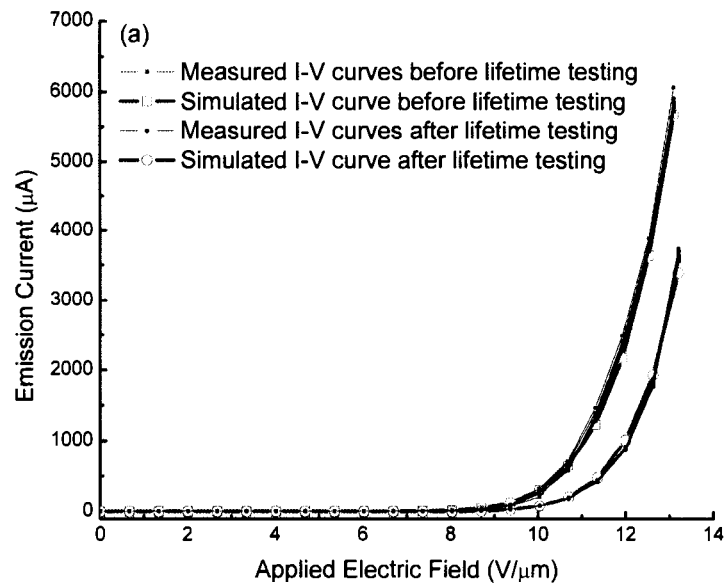


Figure 4. 12 (a)  $I$ - $V$  curves collected immediately before and after the dc lifetime test together with corresponding calculated  $I$ - $V$  curves, (b) their corresponding  $F$ - $N$  plots measured and calculated.

The Fowler-Nordheim equation is applied here to study the field emission behavior change of the CNS sample before and after the dc lifetime test,

$$I = \frac{1.54 \times 10^{-6} A \beta^2 V^2}{\Phi} \exp\left(\frac{-6.83 \times 10^7 \Phi^{3/2}}{\beta V}\right), \quad (4.1)$$

where  $A$  is the emission area ( $\text{cm}^2$ ),  $\beta$  is the field enhancement factor,  $\Phi$  is the work function (eV),  $I$  is the emission current (A), and  $V$  is the applied electric field (V/cm). In Eq. 4.1, elliptical functions are taken to be unity, corresponding to a triangular surface potential barrier [32]. The Fowler-Nordheim equation has been successfully used to predict the field emission behavior of a single metal tip with its known field enhancement factor and emission area [33, 34]. In order to accurately and fully study the field emission behavior of CNS through measured  $I$ - $V$  curves and corresponding  $F$ - $N$  plots, the Fowler-Nordheim equation would have to be applied to each individual emitter in the CNS sample. Such an application of the Fowler-Nordheim equation to CNS is very challenging since there are thousands of emitters with different values of field enhancement factors, emission areas, and work functions in a CNS sample.

Some assumptions have to be made before the Fowler-Nordheim equation is used to study the field emission performance of CNS that have an ensemble of emissive structures randomly distributed on the surface. First, the emission current from each of the emitting sites follows the Fowler-Nordheim equation. Second, all emitters have the same work function, which presumes that all emitters have the same composition and microstructure. Third, the emission area of each emitter is the same since the edges of CNS have the same dimensions.

Rewriting Eq. 4.1, we arrive at

$$\ln\left(\frac{I}{V^2}\right) = \ln\left(\frac{1.54 \times 10^{-6} A \beta^2}{\Phi}\right) - \frac{6.83 \times 10^7 \Phi^{3/2}}{\beta} \cdot \frac{1}{V} \quad (4.2)$$

The slope ( $k$ ) of the  $F$ - $N$  plot is therefore equal to  $\frac{-6830\Phi^{3/2}}{\beta}$  where the current is in  $\mu\text{A}$ ,

the field is in  $\text{V}/\mu\text{m}$ , and  $A$  is in  $\mu\text{m}^2$ . Meanwhile, the intercept ( $s$ ) of the  $F$ - $N$  plot with

$\ln\left(\frac{I}{V^2}\right)$  axis equals  $\ln\left(\frac{1.54 A \beta^2}{\Phi}\right)$  in these units. Therefore, the field enhancement factor  $\beta$

of the CNS sample before and after the lifetime test may be calculated from the

corresponding slopes of  $F$ - $N$  plots indicated by Eq. 4.3 if the work function of carbon

nanosheets were known:

$$\beta = \frac{-6830\Phi^{3/2}}{k} \quad (4.3)$$

Moreover, with an assumed work function  $\Phi$  and the calculated field enhancement factor

$\beta$  before and after the lifetime test using Eq. 4.3, the corresponding emission area may be

estimated from

$$A = \frac{\Phi e^s}{1.54 \beta^2} \quad (4.4)$$

For these purpose, we assume that the work function of CNS before the lifetime test is

4.8 eV, a value that is close to the middle of the range of graphite [35]. During the dc

lifetime test, the work function of CNS may change due to severe gas desorption and re-

absorption. Because of the lack of experimental evidences, the work function of CNS

after the lifetime test can not be clearly defined in this work. However, it is reasonable to

believe that the work function can fall in the range from 4.3 eV to 5.6 eV, which covers

work function values of the tips reported in the literature for carbon nanotubes [35-39].

Table 4.2 presents the field enhancement factor  $\beta$ , the emission area  $A$ , and



effective current density of the emission area  $J_{eff}$ , calculated from the  $F-N$  plots before and after the lifetime test. The field enhancement factor, the emission area, and the effective current density before the lifetime test are 700,  $0.528 \mu\text{m}^2$ , and  $1.1 \times 10^6 \text{ A/cm}^2$  by substituting the assumed work function of CNS 4.8 eV into Fowler-Nordheim equation. The field enhancement factor after the lifetime test ranges from 451 to 671 corresponding to work function changes from 4.3 to 5.6 eV. Meanwhile, the emission area varies from  $8.01$  to  $4.72 \mu\text{m}^2$ . The effective current density changes from  $4.4 \times 10^4$  to  $7.5 \times 10^4 \text{ A/cm}^2$ , which is only 4-6.8% of the effective current density before the lifetime test. To verify the accuracy of the field enhancement factor and emission area calculated from the work function of CNS,  $I-V$  curves and  $F-N$  plots before and after the lifetime test are simulated by substituting the work function, the corresponding field enhancement factor, and the corresponding emission area into Fowler-Nordheim equation. Here, the simulated  $I-V$  curve and  $F-N$  plot after the lifetime test are generated by using a work function of 4.8 eV, a field enhancement factor of 533, and an emission area of  $6.43 \mu\text{m}^2$ . The simulated  $I-V$  curves and  $F-N$  plots are plotted in red in Fig. 4.12, fitting the original data very well.

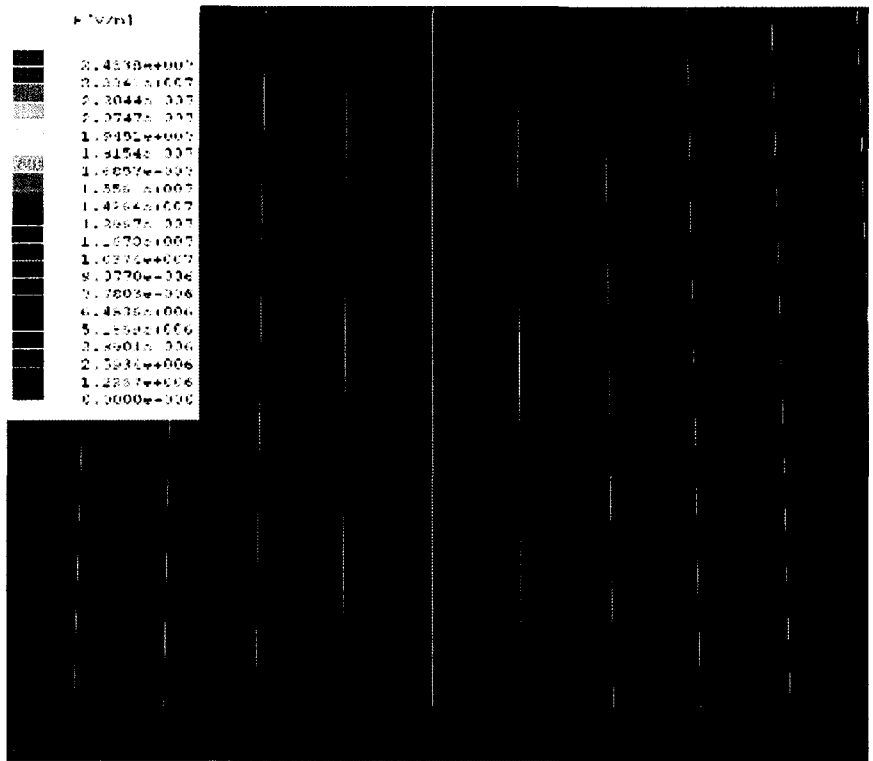
The calculated smaller emission areas and measured larger current before the lifetime test suggest that there are some emitters in the CNS sample carrying a larger amount of measured current before the lifetime test. We define these emitters as “hot runners” in the CNS sample, which have extremely high field enhancement factors and contribute most emission current measured. In the case of carbon nanosheets, there may be mainly two possible types of hot runners co-existed in the sample. One represents an extremely high nanosheet; the other one represents an extremely thin nanosheet.

Table 4.2 Calculated field enhancement factor  $\beta$ , the emission area  $A$ , and the effective current density of the emission area  $J_{eff}$  from the  $F-N$  plots before and after the lifetime test by substituting the work function into Fowler-Nordheim equation.

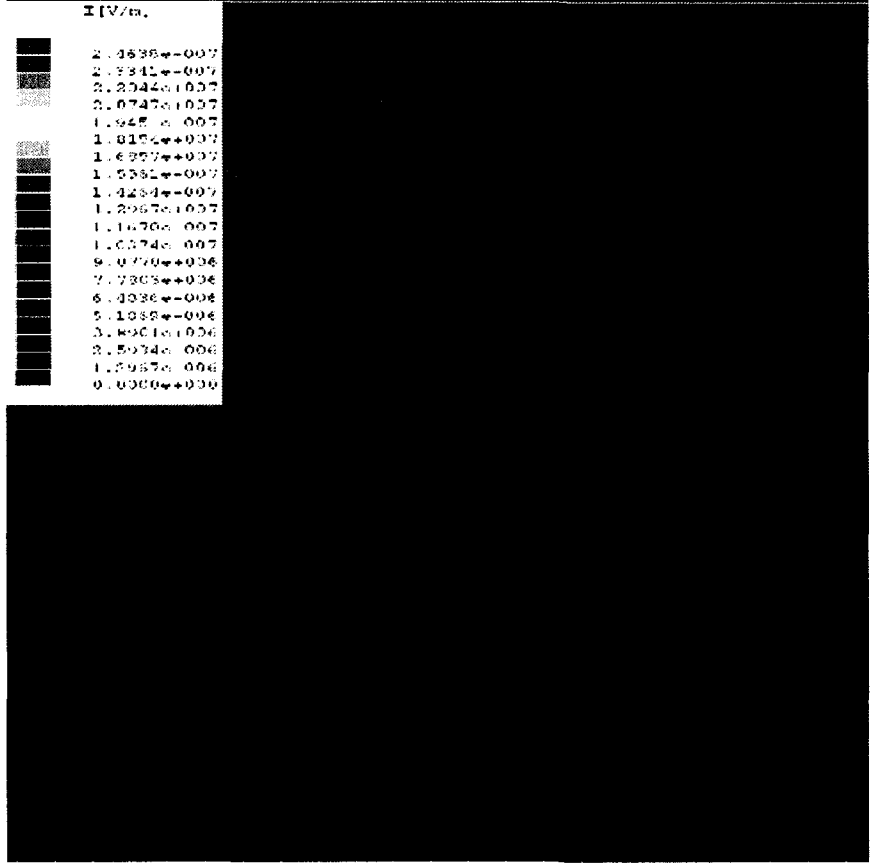
	Work function (eV)	$\beta$	$A$ ( $\mu\text{m}^2$ )	$J_{eff}$ ( $\text{A}/\text{cm}^2$ )
Before lifetime test	4.8	700	0.53	$1.1 \times 10^6$
After lifetime test	4.3	451	8.01	$4.4 \times 10^4$
	4.4	468	7.65	$4.7 \times 10^4$
	4.5	484	7.31	$4.9 \times 10^4$
	4.6	500	7.00	$5.1 \times 10^4$
	4.7	516	6.71	$5.3 \times 10^4$
	4.8	533	6.43	$5.5 \times 10^4$
	4.9	549	6.17	$5.8 \times 10^4$
	5.0	566	5.92	$6.0 \times 10^4$
	5.1	583	5.69	$6.3 \times 10^4$
	5.2	601	5.48	$6.5 \times 10^4$
	5.3	618	5.23	$6.8 \times 10^4$
	5.4	636	5.08	$7.0 \times 10^4$
	5.5	653	4.90	$7.3 \times 10^4$
	5.6	671	4.72	$7.5 \times 10^4$

The effects of hot runners on the field emission behavior of the CNS sample is primarily studied using Maxwell SV (Ansoft) software to visualize 2D electrostatic field at the tips of nanosheet emitters when a negative bias is applied. We assumed nanosheets were 800 nm in height with a tip thickness of 10 nm and separated from each other by 1.5  $\mu\text{m}$ . The substrate used for this simulation is Si with a relative permittivity of 11.9 and assigned to the same potential as nanosheet emitters. Meanwhile, a grounded copper bar is placed 254  $\mu\text{m}$  above the Si substrate to mimic the real test environment of the diode sample holder assembly. The negative bias applied to nanosheet emitters and the Si substrate is 4000 V in this case. The field emission current from emitters is not taken into account by this simulation.

Figure 4.13(a) shows the 2D electrostatic electric field generated at tips of identical carbon nanosheet emitters. Here, identical emitters refer to those nanosheets with same height, tip thickness, and inter-sheet distance. The result reveals that each tip of these identical nanosheet emitters is equally exposed to the electrostatic field ( $\sim 18 \text{ V}/\mu\text{m}$ ). As a result, a spatially uniform emission would be expected from these identical nanosheets. Moreover, this result is consistent with simulation results on carbon nanotube films proposed by Nilsson et al [40]. They pointed out that an electrostatic screening effect exists, from the proximity of neighboring emitters, causing the degraded field emission performance when the density of carbon nanotubes is high. However, they have not studied the shielding effect that hot runners may enact on their neighboring emitters. When there is one high nanosheet emitter (hot runner) among identical emitters, the 2D electrostatic field generated at tips of emitters is shown in Fig. 4.13(b). Here, the high nanosheet emitter is 1600 nm in height (twice as high as its neighbors), but still identical 10 nm in thickness. The inter-sheet distance of emitters is maintained at 1.5  $\mu\text{m}$ . The result indicates that the hot runner is exposed to a high electric field (about  $18 \text{ V}/\mu\text{m}$ ) but its neighboring emitters see a much lower electric field (less than  $1 \text{ V}/\mu\text{m}$ ), too low to turn on emitters. So hot runners shield their neighboring emitters from the electric field and suppress their neighbors' contributions to the emission current. We refer to this as the "shielding effect" in this work. It is only after hot runners are damaged or have disappeared that their neighboring emitters will start emitting electrons. A second independent case might involve one thin nanosheet emitters of a height equal to all other thicker emitters.



2.4538e+007  
 2.2044e+007  
 2.0747e+007  
 1.9451e+007  
 1.8154e+007  
 1.6857e+007  
 1.5561e+007  
 1.4264e+007  
 1.2967e+007  
 1.1670e+007  
 1.0374e+007  
 9.0770e+006  
 7.7803e+006  
 6.4836e+006  
 5.1869e+006  
 3.8901e+006  
 2.5934e+006  
 1.2967e+006  
 0.0000e+000



2.4538e-007  
 2.2044e-007  
 2.0747e-007  
 1.9451e-007  
 1.8154e-007  
 1.6857e-007  
 1.5561e-007  
 1.4264e-007  
 1.2967e-007  
 1.1670e-007  
 1.0374e-007  
 9.0770e-008  
 7.7803e-008  
 6.4836e-008  
 5.1869e-008  
 3.8901e-008  
 2.5934e-008  
 1.2967e-008  
 0.0000e+000

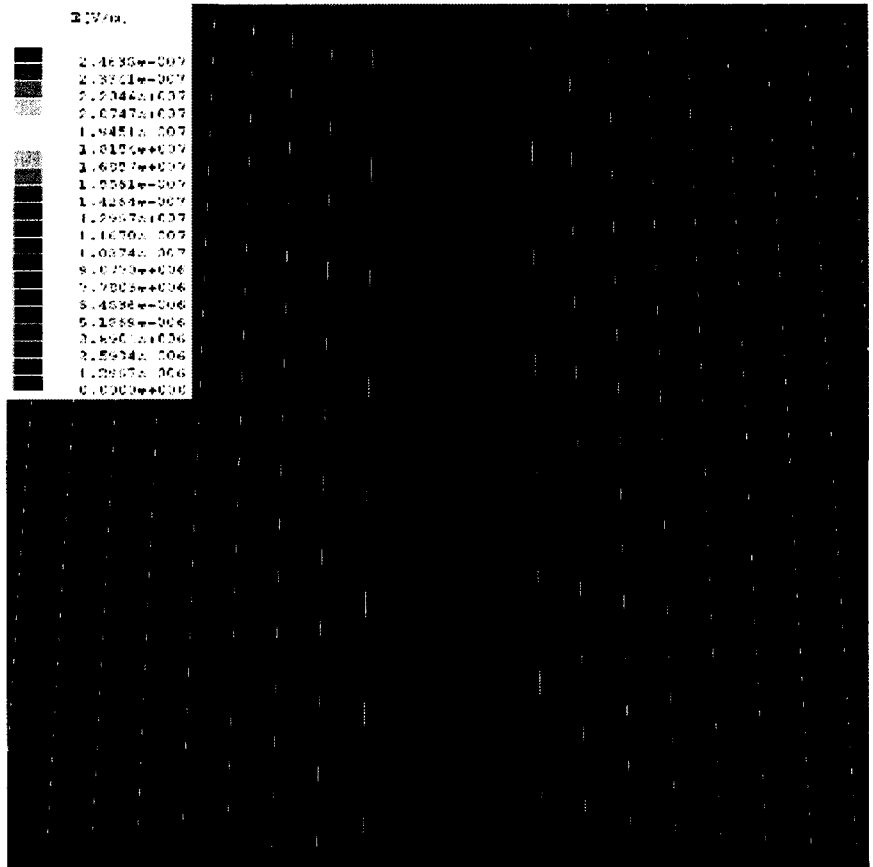


Figure 4.13 2D electrostatic electric field simulation conducted by Maxwell SV at tips of (a) identical emitters, (b) one high hot runner, (c) one thin hot runner.

Fig. 4.13(c) shows the 2D electrostatic field in this case for a 5 nm thick and 800 nm high hot runner in a field of emitters taken to be 800 nm high and 10 nm thick. The resulting field reveals a less severe shielding effect than the high nanosheet emitter. Only the nearest neighbors are completely suppressed. In general, “hot runners” shield their neighboring emitters and thereby cause spatially non-uniform emission from a CNS

sample.

As presented in Table 4.2, we calculated the effective current density of  $1.1 \times 10^6$  A/cm<sup>2</sup> before the lifetime test associated with a very small effective emission area. The local current density of a hot runner indeed may be much higher than  $1.1 \times 10^6$  A/cm<sup>2</sup>. Purcell et al pointed out that the equilibrium temperature at the tip of a multi-walled carbon nanotube could be as high as 2000 K when the current density at the tip was on the order of  $\sim 8.5 \times 10^4$  A/cm<sup>2</sup> [41]. Huang et al pointed out that the self-heating process of a nanotube can lead to a cathode initiated vacuum breakdown process [42]. When the apex temperature of a nanotube is over the equilibrium temperature, a thermal runaway, such as subliming and melting, will occur on nanotubes. The critical current density for a nanotube to start thermal runaway was found to be on the order of  $\sim 10^6$  A/cm<sup>2</sup>. Therefore, thermal runaway may have been occurring on nanosheet hot runners at the beginning of our dc lifetime test. This is supported by our observations of light emission from nanosheets during the test and by traces of carbon deposited on the anode after the test. "Conditioning", then, is likely to be the removal process of hot runners [43], leaving a larger number of neighboring emitters having a much lower  $\beta$  expose to the electric field, which turn on sequentially. This accounts for the apparent increase in the effective emission area (about an order of magnitude after the dc lifetime test) extracted in our calculation. Our calculation also indicates these emitters with a lower effective  $\beta$  factor later turned on. Consequently, the threshold field of the CNS sample increases, as observed in Fig. 4.12. Once hot runners are efficiently removed and the surface is stabilized, no further current drop was observed in the dc lifetime test, as indicated in Fig. 4.11. This, too, is consistent with our proposed explanation.

SEM images of the test area of the CNS sample before and after the dc lifetime test are displayed in Figure 4.14. Images of the CNS sample taken in a top view, shown in Figs. 4.14(a)-(b), reveal no evident morphology changes. The average CNS thickness is almost the same before and after the lifetime test. However, SEM images taken in the cross-section of the CNS sample, Figs. 4.14(c)-(d), show that the average height of CNS falls from 1.8  $\mu\text{m}$  at the beginning of the test to 1.46  $\mu\text{m}$  in the end. This is a substantial change on average, which may be a consequence of the thermal processes during the conditioning process.

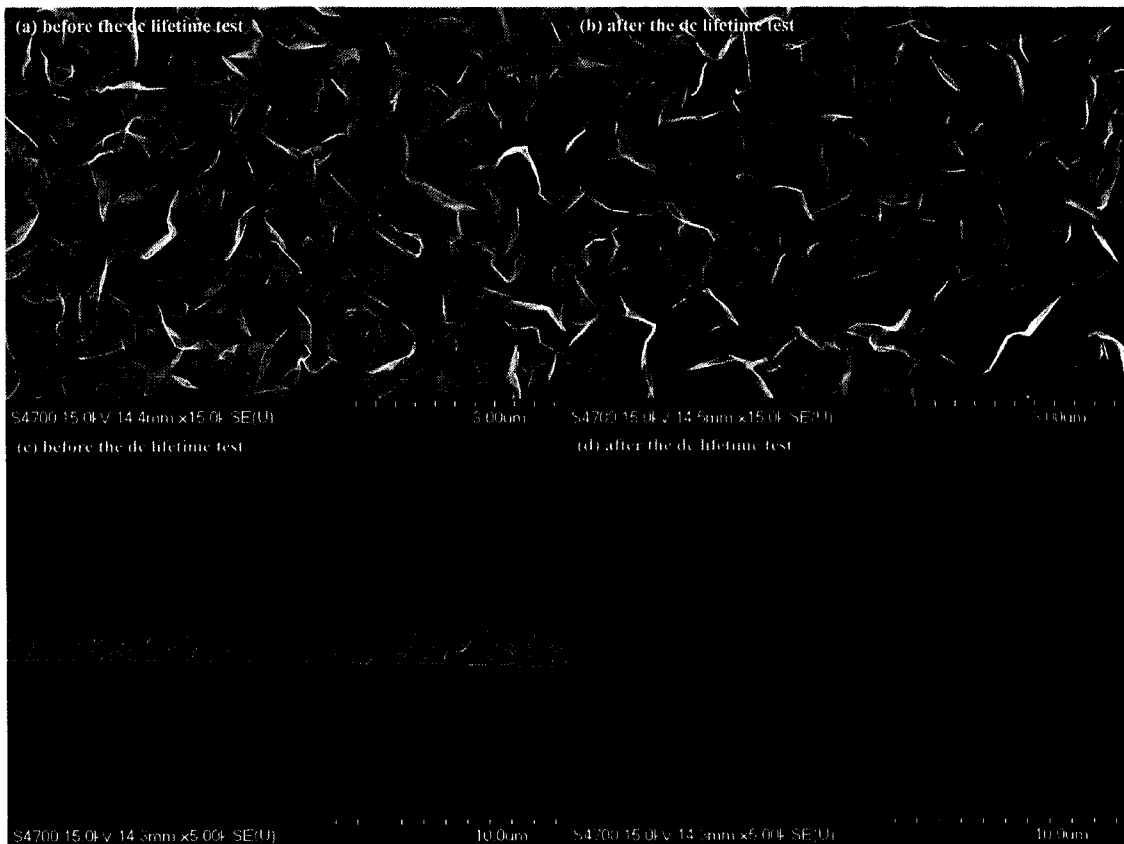


Figure 4.14 SEM images of the CNS sample before and after the dc lifetime test.

(a) top view image before the dc lifetime test, (b) top view image after the dc lifetime test, (c) cross-section view image before the dc lifetime test, (d) cross-section view image after the dc lifetime test.

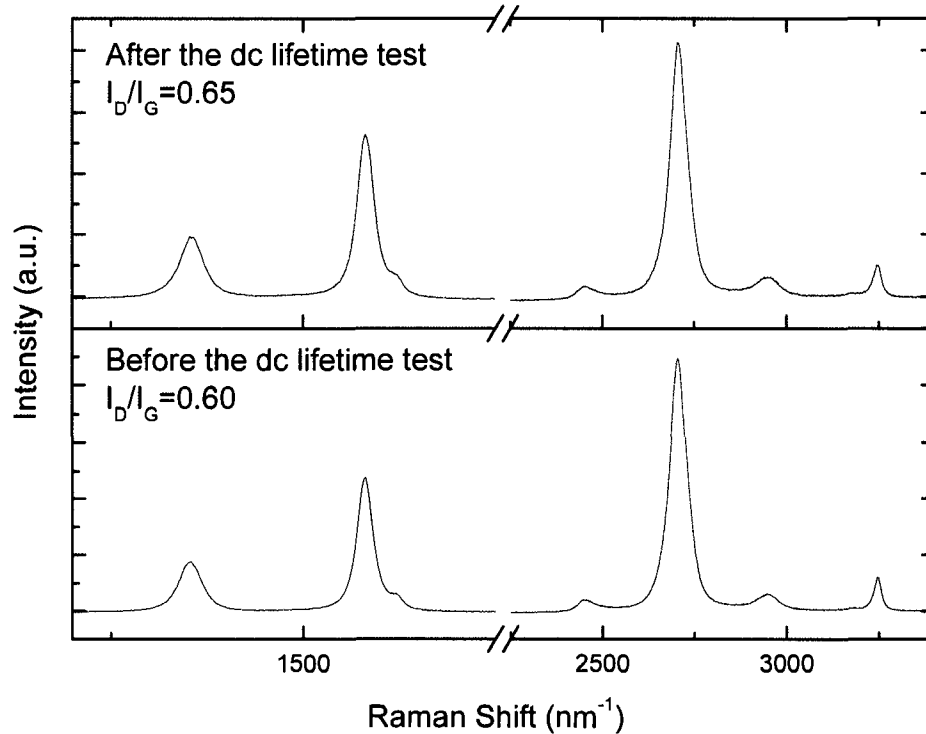


Figure 4.15 Raman spectra of the CNS sample before and after the dc lifetime test.

Raman spectra of the CNS sample before and after the dc lifetime test are shown in Figure 4.15. The ratio of the intensity of the D peak to the G peak increases only a small amount from 0.60 at the beginning of the test to 0.68 in the end. Moreover, the D and G peaks are similar in detail before and after the dc lifetime test, suggesting that the microstructure of the CNS sample does not change dramatically.

In summary, we studied the field emission behavior of CNS by calculating  $I-V$  curves before and after the dc lifetime test. The results indicate that hot runners having high field enhancement factor are present initially, which dominate the initial emission current. During the conditioning, these hot runners are removed, most likely through a



thermal runaway mechanism. With the elimination of hot runners in the CNS sample, emitters with lower field enhancement factors start turning on and sustain a steady and stable emission for a long period. Moreover, the spatially non-uniform emission can be expected from CNS until hot runners have been conditioned away.

#### 4.7 PEEM AND FEEM OBSERVATION ON CNS

To date, all field emission studies on CNS were conducted by recording the emission current versus the applied electric field or test time. Although a persuasive case can be made for the existence of hot runners in our CNS by the Fowler-Nordheim equation, the actual observation of hot runners on carbon nanostructure emitters has never been done. Therefore, a direct, real time, in-situ field emission study of hot runners is required. Here, we present our study on hot runners in CNS samples using PEEM.

As introduced in Sec. 2.5, photoelectron emission microscopy (PEEM) is a non-destructive microscopic surface analysis technique that impinges photons on a surface and creates images of the surface by collecting ejected photoelectrons using electron optic lenses. When the photon source is absent during the observation, field emission electrons can be used to form images. Thus, a PEEM apparatus provides a second form of microscope called a field emission electron microscope (FEEM). Moreover, the multi-channel plate with a central hole, used in the modified Elmitec PEEM III at Ohio University, allows in-situ measuring I-V curves of the CNS sample. Therefore, PEEM observation can provide real-time in-situ information about the field emission characterization of CNS. The presence and field emission behavior of hot runners in CNS can be studied directly.

A pair of PEEM and FEEM images is displayed in Figure 4.16. The pair of images is captured in the same area of the CNS sample with an applied electric field of  $3.9 \text{ V}/\mu\text{m}$ . Only one bright spot is found in the field of view that has a diameter of  $300 \mu\text{m}$  from both PEEM and FEEM images. Only emitters located within the bright spot in the images are emitting electrons. Since the applied electric field is the same everywhere within the field of view and the work functions of material over so small an area is most likely to be the same, the bright spot must be a direct observation of hot runners with high  $\beta$  factors in that region of the CNS sample. This also confirms that the emission uniformity of non-conditioned CNS samples is poor. Although we can not precisely count the exact number of emitters in the bright spot due to the limited spatial resolution of PEEM apparatus, we propose that the bright spot is most likely to originate from just one emitter.

The  $I$ - $V$  characteristic of this hot runner was measured using a Faraday cup installed right behind the central hole of the multi-channel plate and illustrated in Figure 4.17. The hot runner starts emitting electrons at an applied electric field of  $3.4 \text{ V}/\mu\text{m}$ , yielding a current of  $0.2 \text{ pA}$  and becoming clearly visible in PEEM and FEEM images. The emission current of this hot runner gradually increases to  $1.5 \text{ pA}$  as the applied electric field increases to  $3.9 \text{ V}/\mu\text{m}$ . When the applied electric field increases to  $4.1 \text{ V}/\mu\text{m}$ , the maximum field generated in PEEM, the emission current abruptly jumps to  $580 \text{ pA}$ . The non-exponential  $I$ - $V$  behavior of this hot runner disobeys the Fowler-Nordheim theory, but the thermal runaway is not expected to behave in any events according to the Fowler-Nordheim mechanism. Similar behavior was observed for another hot runner on a different CNS sample.

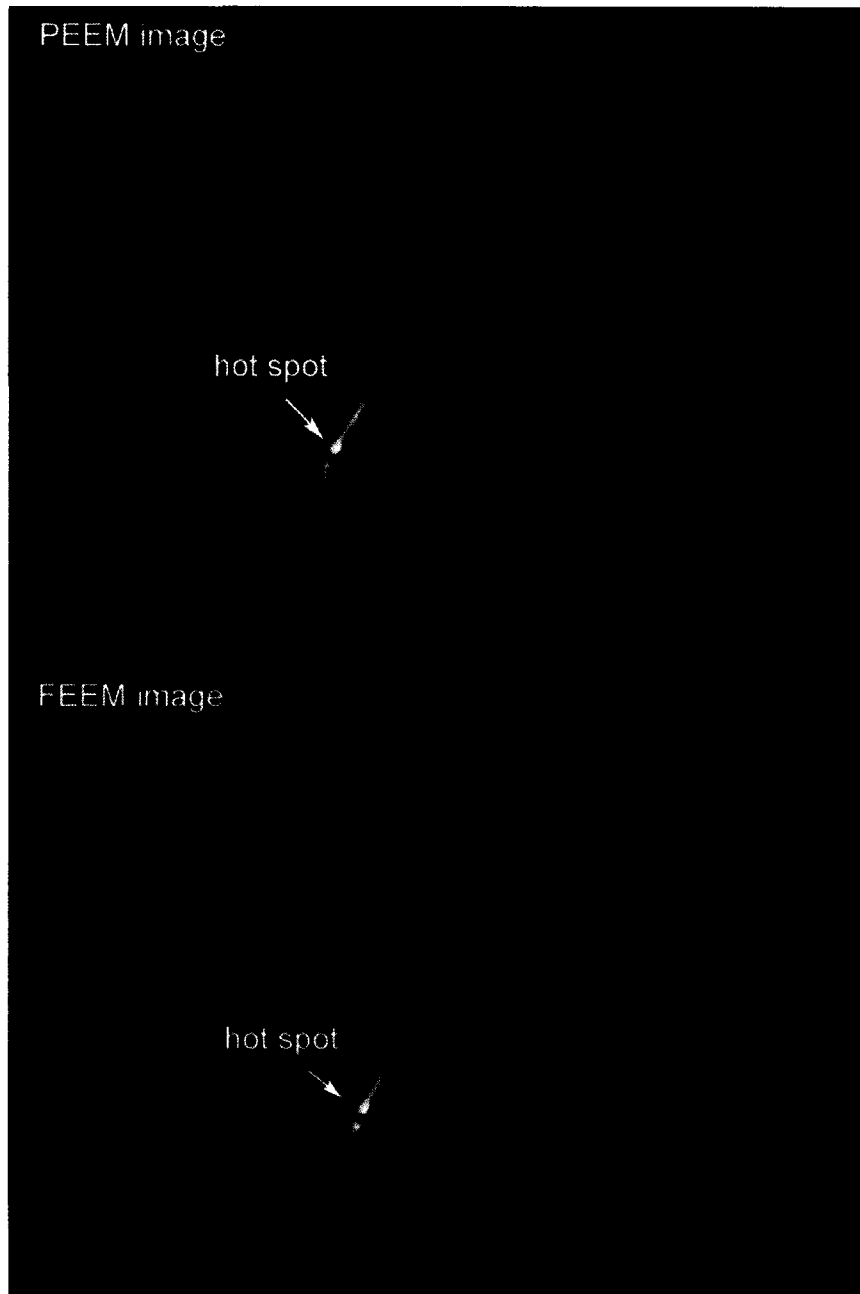


Figure 4.16 PEEM and FEEM images captured in the same test area in a typical CNS sample. Only one bright spot is found in the field of view. This bright spot reveals the existence of hot runners in CNS. (a) PEEM image, (b) FEEM image.

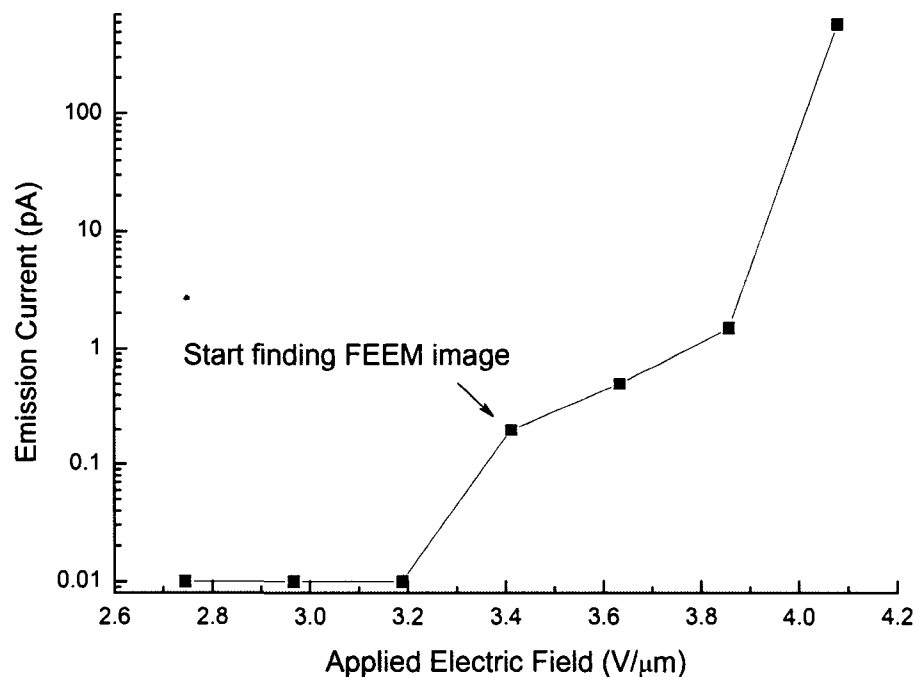


Figure 4.17 Field emission current of the hot runner as a function of the applied electric field.

The emission stability of the hot runner was studied through a short term dc lifetime test. A constant negative bias of 7000 V was applied to the CNS sample to generate an applied electric field of 3.5 V/μm between the sample (the cathode) and the extractor (the anode) of the PEEM apparatus. The current was measured from the hot runner in the field view of FEEM image and manually recorded from a Keithley picoammeter every twenty seconds for the span of an hour. The emission current as a function of time is presented in Figure 4.18. The result reveals that the emission current from this hot runner varies quite abruptly in time, spanning three orders of magnitude (from 0.007 nA to 20 nA) during this test period. In previous sections, we observed stable emission having a standard

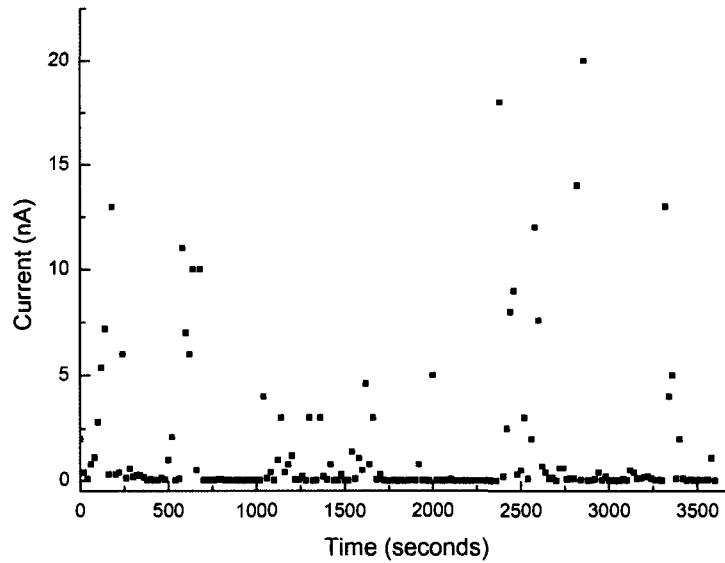


Figure 4.18 Emission current of the hot runner as a function of time in a dc mode.

deviation in current of less than 4% in the absence of hot runners. However, no periods of stable emission were observed in the presence of a hot runner.

Because of their unpredictable and unstable emission nature, hot runners must be eliminated by conditioning CNS samples. The lifetime test results suggest that the gradual electrical conditioning can efficiently remove hot runners from CNS samples to yield stable and uniform emission.

#### 4.8 FIELD EMISSION OF CNS BASED BACK GATE TRIODE DEVICES

Because of their excellent high current performance, robustness, and compatibility with standard semiconductor processing techniques, CNS were tested for field emission applications in back-gated triode devices.

The back-gated devices described here have an improved “buried-line” configuration. This configuration can reduce dielectric breakdown caused by the high electric field generated at the edge of trapezoid-shape cathodes in previous back-gated devices, as discussed in detail in Ref. 19. The fabrication of back-gated triode device starts with a 4-inch n-type heavily doped Si wafer with a 1  $\mu\text{m}$  thermal oxide. Positive photoresist is then applied to develop the pattern for the cathode lines. 0.5  $\mu\text{m}$  deep trenches are formed by isotropic etch. Afterward, thin Cu/Au plating base is evaporated into the trenches. The bare buried-line back-gated device is produced after the removal of the photoresist.

The CNS deposition on bare buried-line back-gated device is performed using standard CNS deposition conditions described in Sec. 4.3. The CNS is then patterned and etched so that the material only remains in the center of the cathode lines. A SEM image of CNS based back-gated device is show in Figure 4. 19.

For testing, the CNS based back-gated devices are mounted into the well of the 24-pin ceramic header [19]. A diode electric field of 9  $\text{V}/\mu\text{m}$  is applied between the anode and cathode lines of CNS based back-gated device. An emission current of  $\sim 12 \mu\text{A}$  is first measured at a back gate voltage of zero volts. Then, with the back gate voltage increased to 120 V, an emission current of  $\sim 220 \mu\text{A}$  was repeatedly achieved. This is almost an eighteen fold increase in the emission current. The emission currents as a function of the back gate voltage are shown in Figure 4.20.

The result confirms the effectiveness of the “buried-line” triode geometry for CNS based back-gated device. Moreover,  $\sim 1.3 \text{ mA}$  emission current has been measured from our CNS back-gated device at a back gate voltage of 180 V, which is an increase in

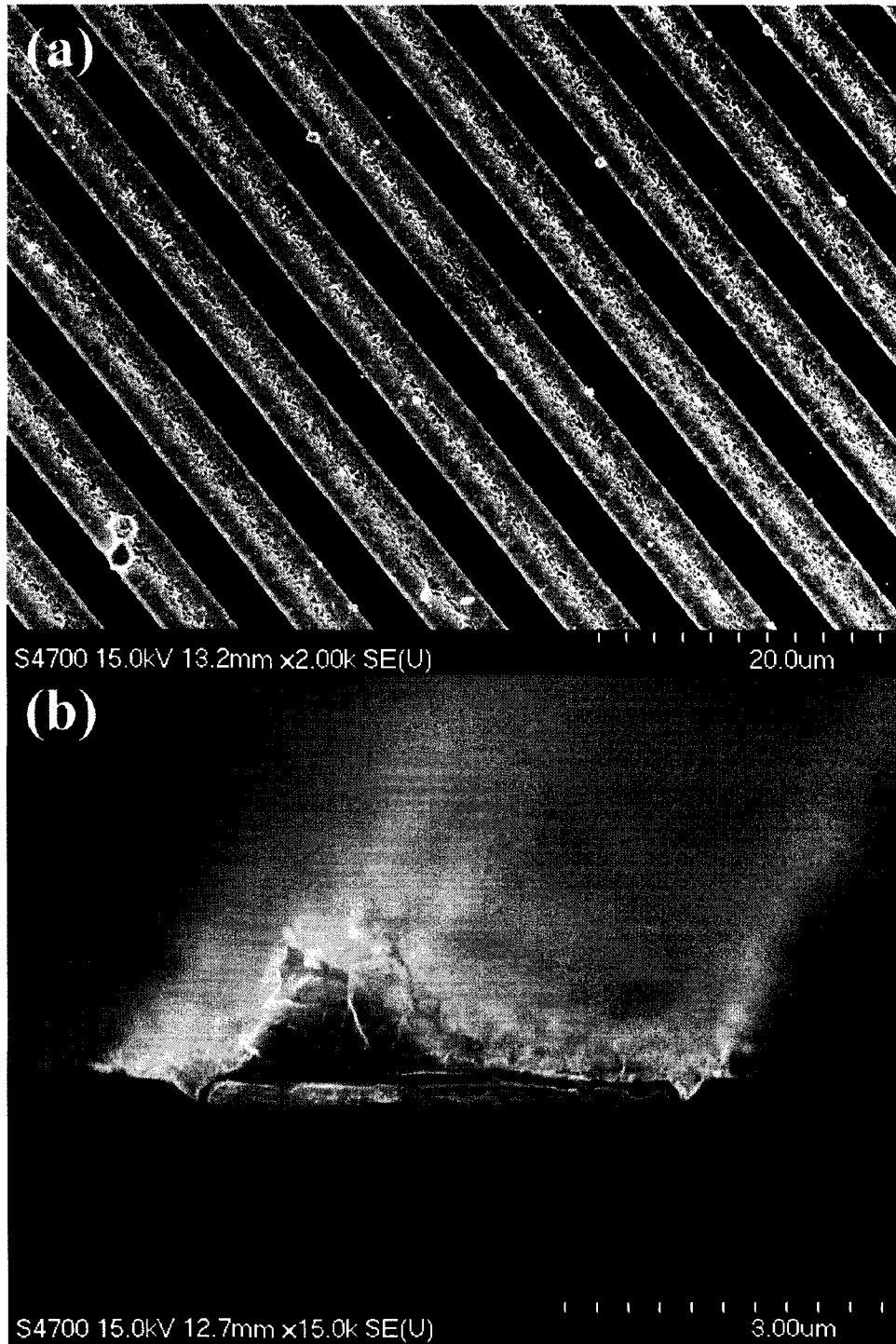


Figure 4.19 SEM images of CNS based “buried-line” back-gated triode device.

(a) top view image, (b) cross-section view image.

emission current of almost three orders of magnitude compared with the emission current without the back gate voltage [15]. To date, short-term failures of CNS based back-gated device have been associated with the dielectric layer ( $0.5 \mu\text{m SiO}_2$ ) breakdown between the cathode lines and the back gate during field emission tests. This is possible to eliminate using a thicker or more stable dielectric layer in future generations of back-gated devices.

#### 4.9 SUMMARY

We have synthesized a novel two-dimensional carbon nanostructure, carbon nanosheets, by radio frequency plasma enhanced chemical vapor deposition. Typical CNS are synthesized on four-inch Si wafer without the need for catalysts in inductively

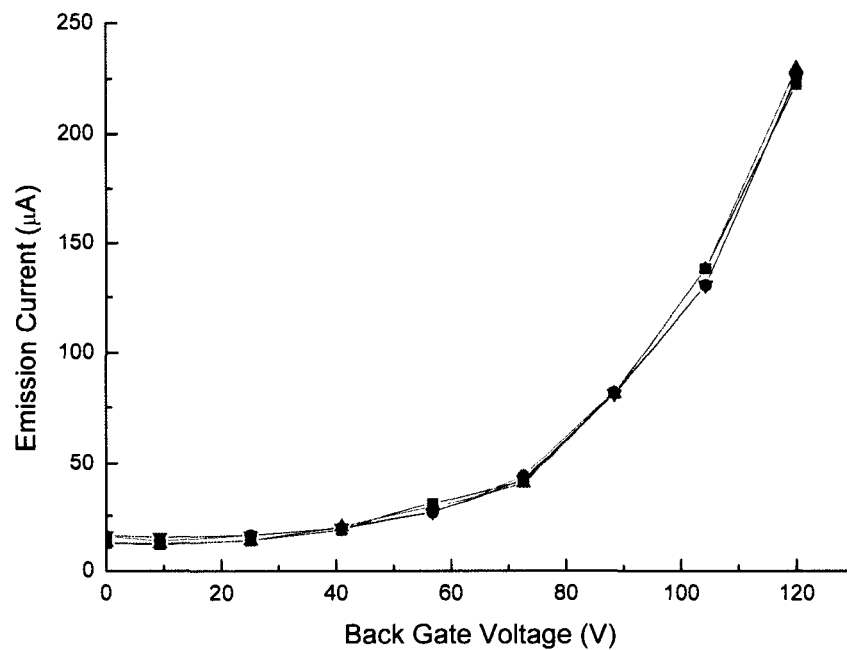


Figure 4.20 Emission current as a function of back gate voltage.



coupled plasma using 40% CH<sub>4</sub> in H<sub>2</sub> atmosphere, at a substrate temperature of 700 °C, a total gas pressure of 100 mTorr, and an input RF power of 900 W. Materials characterization methods, including SEM, TEM, AES, XPS, PIXE, ERDA, TDS, Raman, FTIR, XRD, and BET, have been applied to study the morphology, composition, and structure of CNS. The results indicate that CNS are hundreds of nanometers in length and height, but only <1-4 nm in thickness, which are vertically oriented with respect to the growth surface. The results confirm a honeycomb like morphology, graphitic structure, and atomic thickness of CNS synthesized on a variety of substrates.

We have investigated the field emission properties of carbon nanosheets from various perspectives, including turn-on and threshold field, maximum total current, lifetime in a slow pulse mode, and lifetime in a dc mode. In summary, the turn-on and threshold field of typical CNS lie in the range from 3 to 4.7 V/μm and 3.5 to 5.2 V/μm, respectively. To date, the maximum peak current of a typical CNS sample with a testing area of 32 mm<sup>2</sup> is 33 mA measured at an applied electric field of 26.8 V/μm. The lifetime test in a slow pulse mode suggests that typical CNS can operate at an emission current of ~13 mA with a duty factor of 21% for more than 200 hours after they are initially conditioned for approximately half an hour. Furthermore, typical CNS can continuously emit ~1.5 mA current for more than 200 hours in a dc mode after 3 hours conditioning process. These test results reveal that carbon nanosheets have at least the same level of field emission performance as cathode materials currently in the market.

The study on field emission behavior of CNS has been carried out by applying Fowler-Nordheim equation to field emission characteristics (*I-V* curves) of typical CNS collected immediately before and after the dc lifetime test. The slope of *F-N* plots

originated from  $I$ - $V$  curves and the intercept of  $F$ - $N$  plots with  $\ln(\frac{I}{V^2})$  axis are used to determine the field enhancement factor  $\beta$  and emission area  $A$  with substituting an estimate of the work function of CNS into the Fowler-Nordheim equation. The results suggest the existence of hot runners with high field enhancement factors. However, these hot runners are removed most likely through a thermal runaway process during the conditioning process, leading to a large number of neighboring emitters with low field enhancement factors turning on thereafter. As a result, a stable field emission in a current level of more than 1 mA can be achieved from typical CNS. PEEM and FEEM observations directly confirm the existence of hot runners in CNS. The in-situ  $I$ - $V$  measurements of the hot runner in carbon nanostructure samples are reported for the first time. The result confirms the unpredictable and unstable emission nature of hot runners.

The validation and effectiveness of CNS based back gate device has also been studied.

## References for Chapter IV

- [1] Ando Y, Zhao X, Ohkohchi M. Production of petal-like graphite sheets by hydrogen arc discharge. *Carbon*. 1997;35(1):153-8.
- [2] Shang NG, Au FCK, Meng XM, Lee CS, Bello I, Lee ST. Uniform carbon nanoflake films and their field emissions. *Chemical Physics Letters*. 2002;358(3-4):187-91.
- [3] Wang J, Ito T. High-current-density electron emissions from nano-carbon films fabricated by high-power microwave-plasma chemical vapour deposition. *Diamond and Related Materials*. 2005;14(9):1469-73.
- [4] Chen C-C, Chen C-F, Lee IH, Lin C-L. Fabrication of high surface area graphitic nanoflakes on carbon nanotubes templates. *Diamond and Related Materials*. 2005;14(11-12):1897-900.
- [5] Shang NG, Staedler T, Jiang X. Radial textured carbon nanoflake spherules. *Applied Physics Letters*. 2006;89(10):103112-3.
- [6] Hiramatsu M, Shiji K, Amano H, Hori M. Fabrication of vertically aligned carbon nanowalls using capacitively coupled plasma-enhanced chemical vapor deposition assisted by hydrogen radical injection. *Applied Physics Letters*. 2004;84(23):4708-10.
- [7] Kurita S, Yoshimura A, Kawamoto H, Uchida T, Kojima K, Tachibana M, Molina-Morales P, Nakai H. Raman spectra of carbon nanowalls grown by plasma-enhanced chemical vapor deposition. *Journal of Applied Physics*. 2005;97(10):104320-5.
- [8] Novoselov KS, Geim AK, Morozov SV, Jiang D, Katsnelson MI, Grigorieva IV, Dubonos SV, Firsov AA. Two-dimensional gas of massless Dirac fermions in graphene. *Nature*. 2005;438(7065):197-200.
- [9] Novoselov KS, Geim AK, Morozov SV, Jiang D, Zhang Y, Dubonos SV, Grigorieva IV, Firsov AA. Electric Field Effect in Atomically Thin Carbon Films. *Science*. 2004;306(5696):666-9.
- [10] Zhang Y, Tan Y-W, Stormer HL, Kim P. Experimental observation of the quantum Hall effect and Berry's phase in graphene. *Nature*. 2005;438(7065):201-4.
- [11] Berger C, Song ZM, Li X, Wu X, Brown N, Naud C, Mayou D, Li T, Hass J, Marchenkov AN, Conrad EH, First PN, de Heer WA. Electronic Confinement and Coherence in Patterned Epitaxial Graphene. *Science*. 2006;312(5777):1191-6.
- [12] Berger C, Song ZM, Li TB, Li XB, Ogbazghi AY, Feng R, Dai ZT, Marchenkov AN, Conrad EH, First PN, de Heer WA. Ultrathin epitaxial graphite: 2D electron gas properties and a route toward graphene-based nanoelectronics. *Journal of Physical Chemistry B*. 2004;108(52):19912-6.
- [13] Zhu M, Wang J, Outlaw RA, Hou K, Manos DM, Holloway BC. Synthesis of carbon nanosheets and carbon nanotubes by radio frequency plasma enhanced chemical vapor deposition. *Diamond and Related Materials*. 2007;16(2):196-201.
- [14] Zhao X, Outlaw RA, Wang JJ, Zhu MY, Smith GD, Holloway BC. Thermal desorption of hydrogen from carbon nanosheets. *The Journal of Chemical Physics*. 2006;124(19):194704-6.
- [15] Wang S, Wang J, Miraldo P, Zhu M, Outlaw R, Hou K, Zhao X, Holloway BC, Manos D, Talmage T, Shenderova O, Mark R, Dalton J, McGuire G. High field emission reproducibility and stability of carbon nanosheets and nanosheet-based backgated triode emission devices. *Applied Physics Letters*. 2006;89(18):183103-3.

- [16] Wang JJ, Zhu MY, Outlaw RA, Zhao X, Manos DM, Holloway BC, Mammana VP. Free-standing subnanometer graphite sheets. *Applied Physics Letters*. 2004;85(7):1265-7.
- [17] Wang J, Zhu M, Zhao X, Outlaw RA, Manos DM, Holloway BC, Park C, Anderson T, Mammana VP. Synthesis and field-emission testing of carbon nanoflake edge emitters. *Journal of Vacuum Science & Technology B: Microelectronics and Nanometer Structures*. 2004;22(3):1269-72.
- [18] Wang J, Zhu M, Outlaw RA, Zhao X, Manos DM, Holloway BC. Synthesis of carbon nanosheets by inductively coupled radio-frequency plasma enhanced chemical vapor deposition. *Carbon*. 2004;42(14):2867-72.
- [19] Tyler T, Shenderova O, Ray M, Dalton J, Wang J, Outlaw R, Zhu M, Zhao X, McGuire G, Holloway BC. Back-gated milliamper-class field emission device based on carbon nanosheets. *Journal of Vacuum Science & Technology B: Microelectronics and Nanometer Structures*. 2006;24(5):2295-301.
- [20] French BL, Wang JJ, Zhu MY, Holloway BC. Evolution of structure and morphology during plasma-enhanced chemical vapor deposition of carbon nanosheets. *Thin Solid Films*. 2006;494(1-2):105-9.
- [21] French BL, Wang JJ, Zhu MY, Holloway BC. Structural characterization of carbon nanosheets via x-ray scattering. *Journal of Applied Physics*. 2005;97(11):114317-8.
- [22] Zhu M. Carbon nanosheets and carbon nanotubes by RF PECVD: College of William and Mary; 2006.
- [23] Tuinstra F, Koenig JL. Raman Spectrum of Graphite. *The Journal of Chemical Physics*. 1970;53(3):1126-30.
- [24] Nemanich RJ, Solin SA. First- and second-order Raman scattering from finite-size crystals of graphite. *Physical Review B*. 1979;20(2):392.
- [25] Cheng Y, Zhou O. Electron field emission from carbon nanotubes. *Comptes Rendus Physique*. 2003;4(9):1021-33.
- [26] Bonard J-M, Kind H, Stockli T, Nilsson L-O. Field emission from carbon nanotubes: the first five years. *Solid-State Electronics*. 2001;45(6):893-914.
- [27] Groning O, Kuttel OM, Groning P, Schlapbach L. Field emission properties of nanocrystalline chemically vapor deposited-diamond films. *Journal of Vacuum Science & Technology B: Microelectronics and Nanometer Structures*. 1999;17(5):1970-86.
- [28] Zhu W, Bower C, Zhou O, Kochanski G, Jin S. Large current density from carbon nanotube field emitters. *Applied Physics Letters*. 1999;75(6):873-5.
- [29] Zhao X. Field emission study of carbon nanostructure: College of William and Mary; 2006.
- [30] Dean KA, Chalamala BR. The environmental stability of field emission from single-walled carbon nanotubes. *Applied Physics Letters*. 1999;75(19):3017-9.
- [31] Private communication
- [32] Groning O, Kuttel OM, Emmenegger C, Groning P, Schlapbach L. Field emission properties of carbon nanotubes. *Journal of Vacuum Science & Technology B: Microelectronics and Nanometer Structures*. 2000;18(2):665-78.
- [33] Mackie WA, Morrissey JL, Hinrichs CH, Davis PR. Field emission from hafnium carbide. 38th National Symposium of the American Vacuum Society; 1992; Seattle, Washington (USA): AVS; 1992. p. 2852-6.

- [34] Mackie WA, Hartman RL, Anderson MA, Davis PR. Transition metal carbides for use as field emission cathodes. International vacuum microelectronics conference; 1994; Newport, Rhode Island (USA): AVS; 1994. p. 722-6.
- [35] Zhao J, Han J, Lu JP. Work functions of pristine and alkali-metal intercalated carbon nanotubes and bundles. *Physical Review B*. 2002;65(19):193401.
- [36] Zhao G, Zhang J, Zhang Q, Zhang H, Zhou O, Qin LC, Tang J. Fabrication and characterization of single carbon nanotube emitters as point electron sources. *Applied Physics Letters*. 2006;89(19):193113-3.
- [37] Xu Z, Bai XD, Wang EG, Wang ZL. Field emission of individual carbon nanotube with in situ tip image and real work function. *Applied Physics Letters*. 2005;87(16):163106-3.
- [38] Lim SC, Jeong HJ, Kim KS, Lee IB, Bae DJ, Lee YH. Extracting independently the work function and field enhancement factor from thermal-field emission of multi-walled carbon nanotube tips. *Carbon*. 2005;43(13):2801-7.
- [39] Gao R, Pan Z, Wang ZL. Work function at the tips of multiwalled carbon nanotubes. *Applied Physics Letters*. 2001;78(12):1757-9.
- [40] Nilsson L, Groening O, Emmenegger C, Kuettel O, Schaller E, Schlapbach L, Kind H, Bonard JM, Kern K. Scanning field emission from patterned carbon nanotube films. *Applied Physics Letters*. 2000;76(15):2071-3.
- [41] Purcell ST, Vincent P, Journet C, Binh VT. Hot Nanotubes: Stable Heating of Individual Multiwall Carbon Nanotubes to 2000 K Induced by the Field-Emission Current. *Physical Review Letters*. 2002;88(10):105502.
- [42] Huang NY, She JC, Chen J, Deng SZ, Xu NS, Bishop H, Huq SE, Wang L, Zhong DY, Wang EG, Chen DM. Mechanism Responsible for Initiating Carbon Nanotube Vacuum Breakdown. *Physical Review Letters*. 2004;93(7):075501-4.
- [43] Nilsson L, Groening O, Groening P, Kuettel O, Schlapbach L. Characterization of thin film electron emitters by scanning anode field emission microscopy. *Journal of Applied Physics*. 2001;90(2):768-80.

CHAPTER V  
FIELD EMISSION PROPERTIES OF CHROMIUM OXIDE COATED  
CARBON NANOSHEETS (CrO<sub>x</sub>-CNS)

### 5.1 INTRODUCTION

This chapter outlines the synthesis, structure, and field emission properties of chromium oxide coated carbon nanosheets (CrO<sub>x</sub>-CNS) fabricated by vacuum evaporating a thin chromium layer onto nanosheets and subsequently exposing them to atmosphere.

Carbon nanosheets, carbon nanotubes or nanofibers, and metallic single tips are three important candidates for use as the electron source in field emission devices such as field emission displays (FEDs), microwave power amplifier tubes, and compact x-ray sources [1-7]. Even though these candidates feature a high emission current at a low applied electric field, their practical application in commercial devices remains limited due to issues such as field emission uniformity and stability. Therefore, many efforts have been devoted to improving the intrinsic field emission properties of these candidates by incorporating a low work function material coatings, such as ZrC, HfC, and et al. Mackie et al [8, 9] reported that the work function of ZrC and HfC film are 3.5 eV and 3.34 eV, respectively. They also studied the field emission properties of ZrC and HfC coated Mo single tips. Their results revealed that a 50% lower voltage resulted in the same emission currents relative to pure Mo single tips. They confirmed that the enhanced

field emission performance of their carbide-coated Mo single tips originated from the low work functions of ZrC and HfC. However, the emission uniformity from carbide-coated Mo single tips was not discussed.

Our group has studied the field emission properties of ZrC coated carbon nanosheets (ZrC-CNS)[10], but no enhanced field emission performance was observed. This failure is probably caused by the trade-off between the lower work function of ZrC nanobeads and a decreased local field enhancement factor due to the geometry of these nanobeads. The results showed the importance of forming conformal coating on CNS in order to enhance their field emission properties. We are currently studying the field emission properties of carbon nanosheets conformally coated with 1 nm Mo<sub>2</sub>C film. These test results indicate that the Mo<sub>2</sub>C-CNS samples have much lower turn-on field than as-grown CNS, which is consistent with ~3.7 eV low work function of Mo<sub>2</sub>C.

Wide bandgap semiconductors, as alternative coating materials for field emitters, have also stimulated considerable attentions in recent years because of their remarkable physical and chemical stability during the electron emission process.

Zhirnov et al [11, 12] and Krauss et al [13] reported that only 25% of the voltage was needed to achieve the same amount of field emission current after Mo and Si single tips were coated with a thin wide-bandgap nanocrystalline diamond film. They suggested that this enhanced field emission performance originated from the negative electron affinity of diamond, resulting in decreasing the effective work function of coated single tips. Zhirnov et al [11] also applied a band diagram model, a theoretical model describing the quasi-thermionic emission of electrons to vacuum [14], to explain the mechanism behind the enhanced field emission performances of nanocrystalline diamond film coated

single Si tips.

Moon et al [15] utilized a chemical synthesis route to fabricate SiO<sub>x</sub>-coated multiwalled carbon nanotubes. They reported a greatly enhanced current density of 5.8 mA/cm<sup>2</sup> from SiO<sub>x</sub>-coated carbon nanotubes at an applied electric field of 2.5 V/μm as compared to a current density of 1.75 mA/cm<sup>2</sup> from raw carbon nanotubes. Yi et al [16] demonstrated that SiO<sub>2</sub>- and MgO-coated carbon nanotubes had not only a lower turn-on field but also a better emission stability against exposed O<sub>2</sub> gas than raw nanotubes. They also revealed that the emitted electrons originated from the conduction band of MgO coating.

Even though very little is known about the field emission behavior of wide bandgap materials, their enhanced, stable, and uniform emission make them attractive to incorporate with CNS. Chromium oxide, a wide bandgap semiconductor ( $E_g \approx 4$  eV)[17] with an electron affinity of 3.76 eV [18], has been proposed as a promising coating material for carbon nanostructures[19], but no details have been reported in the literature.

Here, we introduce a simple way to fabricate a conformal CrO<sub>x</sub> coating on as-grown CNS by initially vacuum evaporating a thin Cr layer on as-grown CNS and subsequently exposing them to air. We refer to chromium oxide coated CNS as CrO<sub>x</sub>-CNS in this study. The enhanced field emission performances of CrO<sub>x</sub>-CNS are presented. Moreover, we report the spatial uniformity of the emission from CrO<sub>x</sub>-CNS, which is reported for the first time.

## 5.2 SYNTHESIS OF CrO<sub>x</sub>-CNS

Carbon nanosheets are synthesized on a heavily doped Si wafer (resistivity of



0.003-0.005  $\Omega\cdot\text{cm}$ ) under typical CNS deposition conditions, as described in Sec. 4.3. In brief, the CNS deposition is conducted for 20 minutes at a substrate temperature of  $\sim 700^\circ\text{C}$ , a chamber pressure of 100 mTorr, and a radio frequency plasma power of 900W. The feedstock gases are 40%  $\text{CH}_4$  in  $\text{H}_2$  atmosphere with a total gas flow rate of 10 sccm.

The as-grown CNS samples are air-transferred into the vacuum evaporator (Ladd Research Industries) and a chromium layer is thereafter evaporated on the surface of CNS. A tungsten wire twisted into a conical shape is applied as the resistance heater in the evaporator. A high-purity chromium chip (99.999%, Ladd Research) is used as the evaporation source in this work. The evaporator is first pumped down to  $\sim 10^{-6}$  Torr and a direct current of 20 amperes is applied to the tungsten wire. The evaporation is conducted for several seconds, and the coated CNS is then exposed to the atmosphere. A color change from black to grey was visually observed after Cr evaporation and subsequent exposure to the atmosphere. We take this as an evidence of the formation of a  $\text{CrO}_x$  thin film.

### 5.3 CHARACTERIZATIONS OF $\text{CrO}_x$ -CNS

The elemental analyses of as-grown CNS and coated CNS were conducted by Energy Dispersive X-ray (EDX) analysis accompanied with SEM images. Here, the coated CNS was fabricated using 15 seconds Cr evaporation. Figure 5.1(a) shows the elemental distribution profile extracted from the EDX survey across the sample area of as-grown CNS seen in the SEM image (inset). Peaks associated with C and Si are observed in the profile. The Si peak originates from the substrate on which nanosheets grow and the C peak comes from CNS itself. No other elements are detected within this

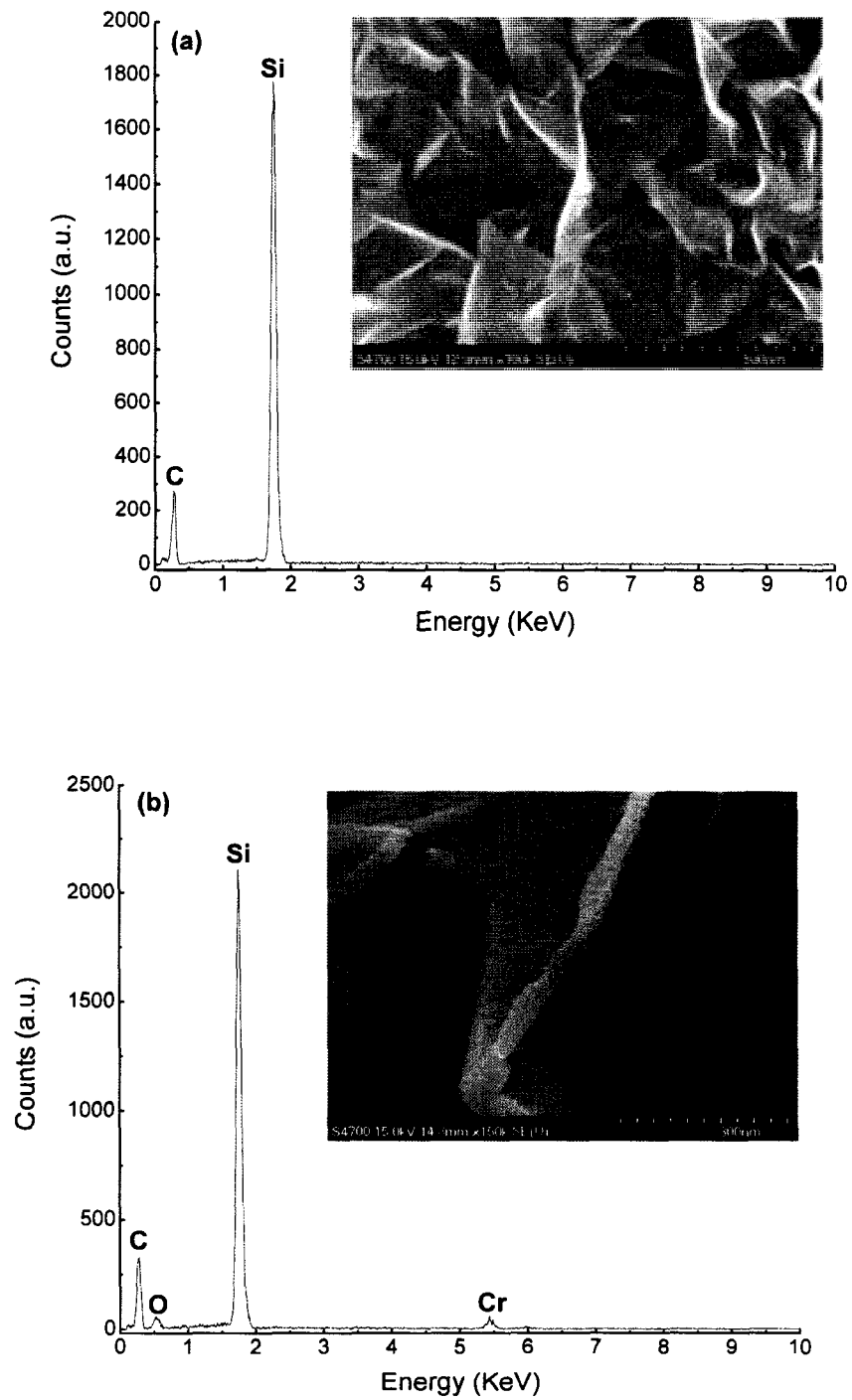


Figure 5.1 EDX spectra of as-grown and coated CNS samples and their corresponding SEM images of the survey area. (a) as-grown CNS, (b) coated CNS.

sample area. In contrast to as-grown CNS, the EDX spectrum of coated CNS shown in Fig. 5.1(b) not only has peaks associated with C and Si but also has peaks of Cr and O, which confirms the formation of chromium oxide coating on CNS. However, the stoichiometry of chromium oxide can not be accurately determined from these EDX spectra.

An Auger spectrum of the coated CNS fabricated using 10 seconds Cr evaporation is displayed in Figure 5.2. The spectrum is collected using a Physical Electronic 590 surface analysis system with a 3 kV/1  $\mu$ A electron beam. Instead of a single C peak as observed from as-grown CNS [10], Cr and O peaks are also found in the spectrum, again

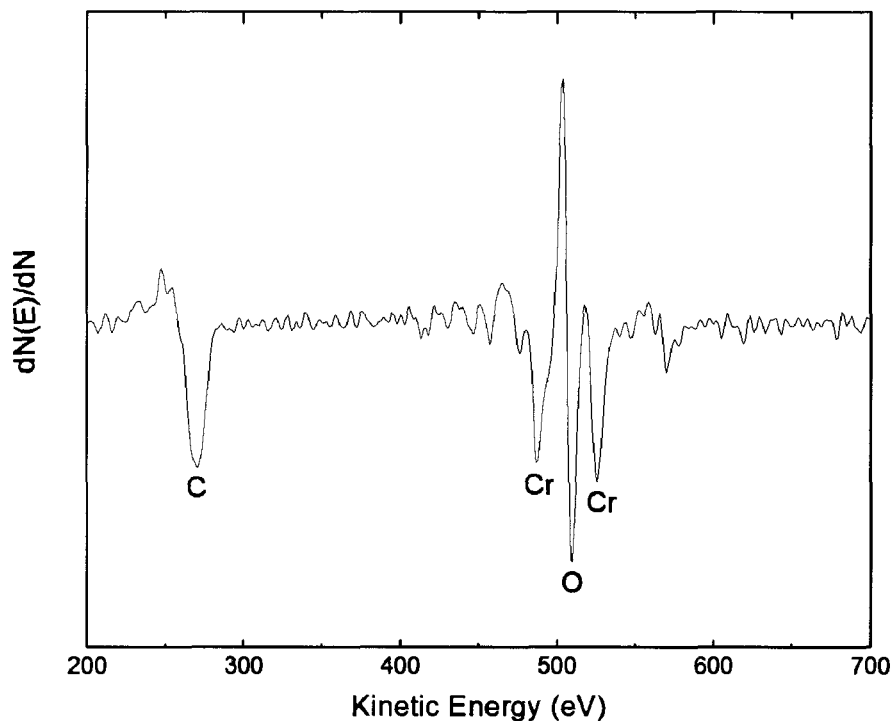


Figure 5.2 Auger spectrum of  $\text{CrO}_x$ -CNS.

confirming the formation of  $\text{CrO}_x$  thin layer on the surface of CNS. The atomic concentration of the layer is determined from the amplitudes of Cr and O peaks in the spectrum and their relative sensitive factors, which are 0.33 for Cr and 0.5 for O with the electron beam at an incident energy of 3 kV [20]. Therefore, the composition ratio for Cr to O is estimated to be 0.37, very close to the composition ratio of  $\text{Cr}_2\text{O}_3$ . The small deviation from the expected value of 0.4 may be the indication of chromium oxide with other stoichiometry present in the coating. Thus, we continue designating the film as  $\text{CrO}_x$  in this work.

Raman spectra of as-grown CNS and  $\text{CrO}_x$ -CNS, shown in Figure 5.3, are collected from a  $\text{CrO}_x$ -CNS sample that has a patterned structure by using a TEM grid as the mask on top of the CNS sample during the vacuum evaporation. Square pads of  $\text{CrO}_x$ -CNS and streets of as-grown CNS are alternatively formed on the same sample. Spectra are obtained from a square pad of  $\text{CrO}_x$ -CNS (indicated by the black arrow) and its nearest as-grown CNS street (indicated by the white arrow) by focusing the incident laser beam inside them to reduce the spatial-induced spectrum deviation. Three peaks are found in the spectrum of as-grown CNS, including a disorder-induced D peak at  $1355\text{ cm}^{-1}$ , a tangential-mode G peak at  $1583\text{ cm}^{-1}$ , and a D' shoulder at  $1620\text{ cm}^{-1}$ . The intensity ratio of the D peak to the G peak ( $I_D/I_G$ ) in the spectrum of as-grown CNS is  $\sim 0.50$ , consistent with the value of typical CNS reported in Sec. 4.4. In addition to these three peaks originating from as-grown CNS, one additional peak is observed from  $\text{CrO}_x$ -CNS that is located at  $551\text{ cm}^{-1}$ . According to published Raman data [21, 22],  $\text{Cr}_2\text{O}_3$  has a strong peak at  $551\text{ cm}^{-1}$  and two weak peaks at  $397$  and  $609\text{ cm}^{-1}$ . Therefore, we assign the  $551\text{ cm}^{-1}$  peak to  $\text{Cr}_2\text{O}_3$ . The broad band between  $551\text{ cm}^{-1}$  and  $800\text{ cm}^{-1}$  suggests the existence of

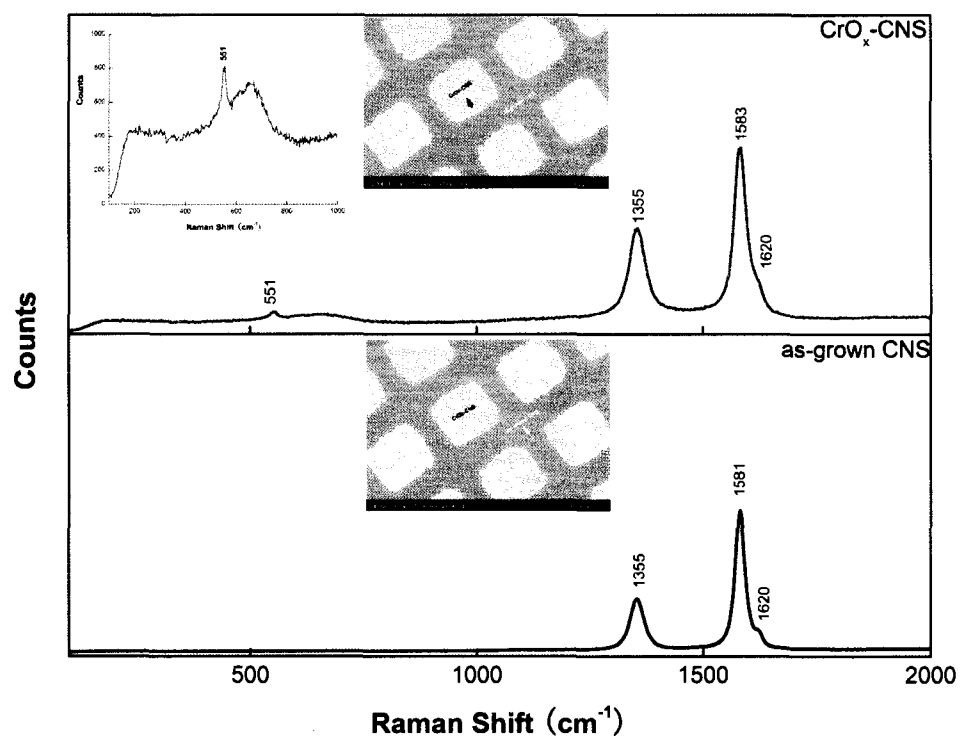
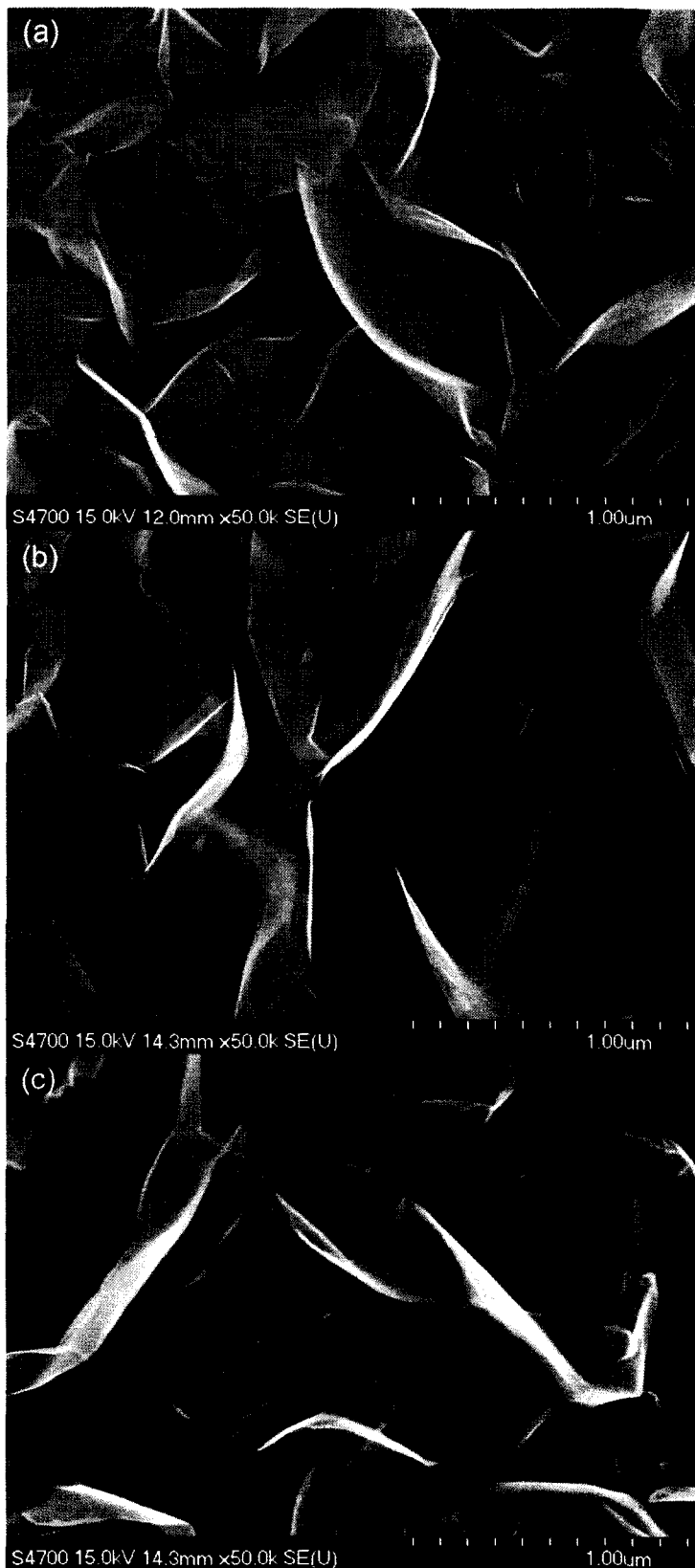


Figure 5.3 Raman spectra of  $\text{CrO}_x$ -CNS and as-grown CNS.

other stoichiometric chromium oxide, such as,  $\text{CrO}_2$  [23]. Further, the intensity ratio of the D peak to the G peak in the spectrum of  $\text{CrO}_x$ -CNS increases to 0.68. The result suggests that more disorder is generated in the CNS by Cr evaporation and oxidation. We believe that these disorders are most likely to be found at the interface between the  $\text{CrO}_x$  coating and CNS.

SEM images of  $\text{CrO}_x$ -CNS and as-grown CNS are shown in Figure 5.4. Here, the  $\text{CrO}_x$ -CNS were fabricated using different evaporation time. The top view image of as-grown CNS, shown in Fig. 5.4(a), reveals that typical nanosheets are corrugated assemblies of folded graphitic sheets with smooth surfaces that are  $\sim 1000$  nm long and on average  $\sim 2$  nm thick. Top view images of  $\text{CrO}_x$ -CNS with a Cr evaporation time of 2, 5,



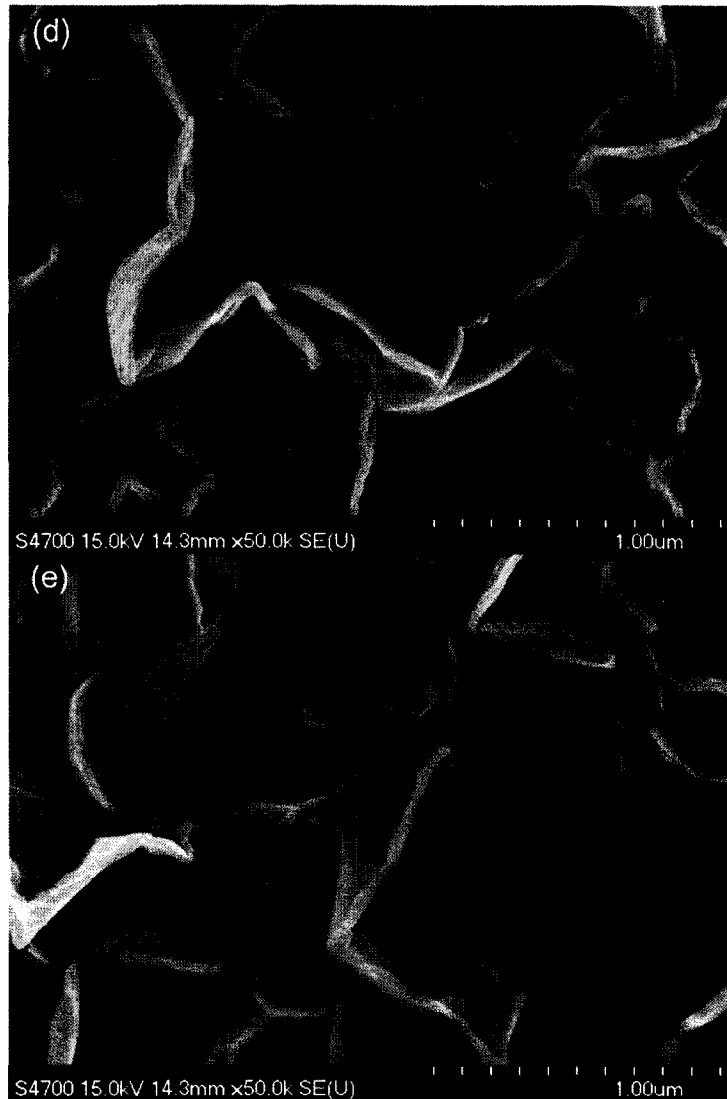


Figure 5.4 SEM images of as-grown CNS and  $\text{CrO}_x$ -CNS with a variety of evaporation time. (a)  $T=0$  second (as-grown CNS), (b)  $t=2$  seconds, (c)  $t=5$  seconds, (d)  $t=10$  seconds, (e)  $t=15$  seconds.

10, and 15 seconds are displayed in Figs. 5.4(b)-(e), respectively. These images reveal that a conformal  $\text{CrO}_x$  coating are formed in each case. Even though the  $\text{CrO}_x$  coatings do not appear as highly contrasted features in Figs. 5.4 (b) and (c), the observed edges

indicate that the coating must be conformal, as also confirmed by other characteristic methods. The thicknesses of  $\text{CrO}_x$  coating were determined from the average value of the thickness for the individual coated CNS taken throughout the sample. Since  $\text{CrO}_x$  layers are fabricated on both sides of nanosheets, the thickness of the coating is close to the half thickness difference of CNS before and after the evaporation. The results are summarized in Table 5.1. We note that the thickness of  $\text{CrO}_x$ -CNS is quite uniform along the length of each individual nanosheet for each value of the evaporation time.

#### 5.4 PEEM AND FEEM OBSERVATIONS ON $\text{CrO}_x$ -CNS

As described in Sec. 2.5, PEEM captures both photoelectrons generated by the photon source and field emission electrons extracted by the applied electric field to form images while FEEM only uses field emission electrons for imaging with the absence of photon source in PEEM. The contrast information of PEEM and FEEM images yields the spatial distributions of electron source in the sample and thereby determines the emission uniformity of the sample. In Sec. 4.7, PEEM and FEEM observations present the existence of hot spots in as-grown CNS, suggesting that their emission uniformity is quite poor. Here, we will show that  $\text{CrO}_x$ -CNS films have the excellent emission uniformity and enhanced field emission performance.

Table 5.1 The thickness of  $\text{CrO}_x$  coating with regard to various evaporation time.

Evaporation time (s)	2	5	10	15
Coated CNS thickness (nm)	3	5	32	42
$\text{CrO}_x$ thickness (nm)	~0.5	~1.5	~15	~20



To directly compare the field emission performance of CrO<sub>x</sub>-CNS and as-grown CNS, patterned CrO<sub>x</sub>-CNS samples were used for PEEM and FEEM observations. Patterned CrO<sub>x</sub>-CNS samples were fabricated by using an evaporation time of 10 seconds through a TEM grid over as-grown CNS samples to form alternating CrO<sub>x</sub>-CNS squares and as-grown CNS streets. Two PEEM systems (modified Elmitec PEEM located at Ohio University and modified Staib PEEM located at NIST) operating at a pressure on the order of  $\sim 10^{-8}$  Torr were used to conduct these observations with four CrO<sub>x</sub>-CNS samples. Results show the same pattern for all observations. In addition to imaging, the in-situ *I-V* measurements of the patterned CrO<sub>x</sub>-CNS sample were conducted in the modified Elmitec PEEM.

Figure 5.5 shows SEM, PEEM and FEEM images of the patterned CrO<sub>x</sub>-CNS sample. The SEM image, Fig. 5.5(a), reveals that a well-patterned structure was formed on the CNS sample. The CrO<sub>x</sub>-CNS squares are 50  $\mu\text{m} \times 50 \mu\text{m}$  in area and separated with each other by 25  $\mu\text{m}$  wide as-grown CNS streets. Here, an electric field of  $\sim 4 \text{ V}/\mu\text{m}$  was applied between the patterned CrO<sub>x</sub>-CNS sample (cathode) and the extractor of PEEM (anode) during PEEM and FEEM observations. The PEEM image, Fig. 5.5(b), shows the dark CrO<sub>x</sub>-CNS squares and bright as-grown CNS streets. According to the in-situ emission current measurements of the patterned CrO<sub>x</sub>-CNS taken in the field of view with a diameter of 300  $\mu\text{m}$  that contains alternating squares and streets, the collected currents are 2.4 pA for photoelectron emission and 0.1 pA for field electron emission. Photoelectrons are therefore the dominant electron source for imaging in this case. The PEEM image suggests that CrO<sub>x</sub>-CNS squares generate fewer photoelectrons than as-grown CNS streets, which is consistent with the fact that the wide-bandgap CrO<sub>x</sub> coating

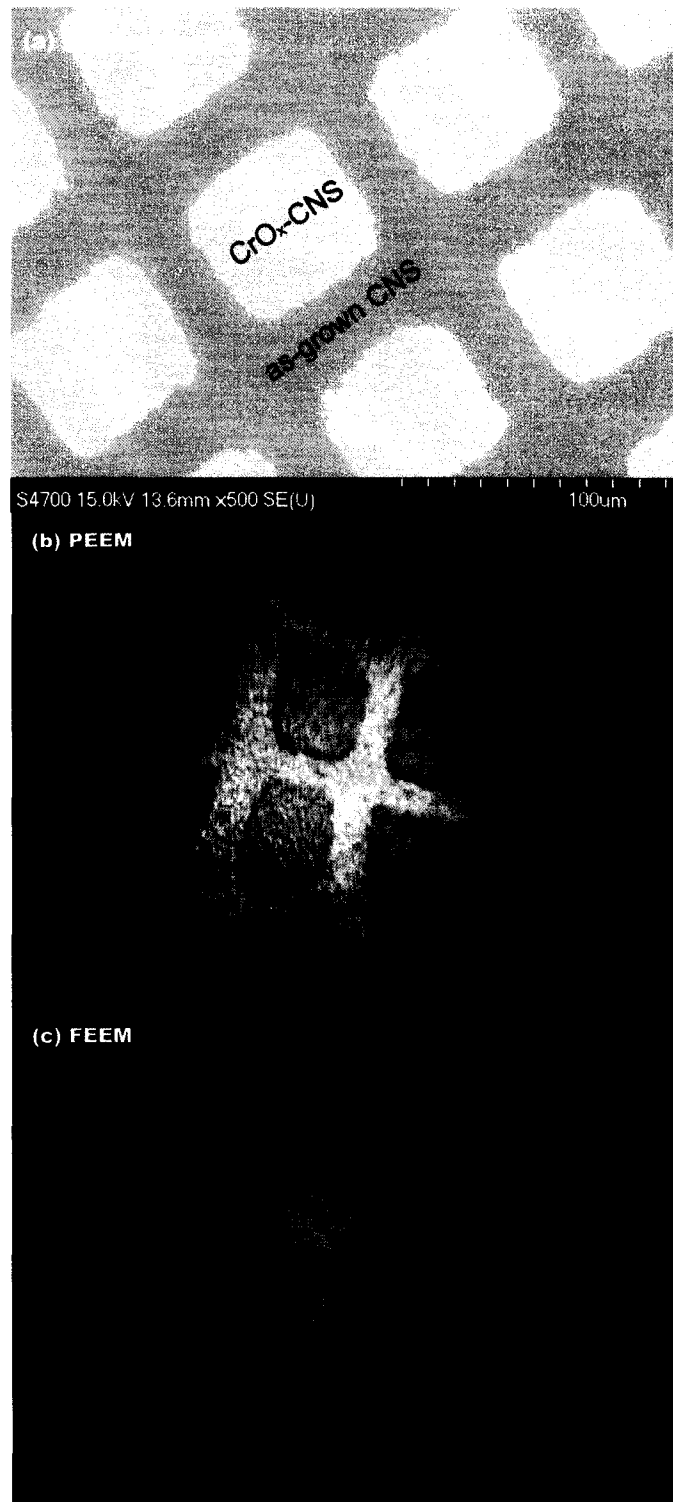


Figure 5.5 SEM, PEEM, and FEEM images of patterned CrO<sub>x</sub>-CNS, (a) SEM image, (b) PEEM image, (c) FEEM image.

can suppress the photoelectron production from the wavelength of light used in this instrument [24]. The FEEM image shown in Fig. 5.5(c), on the other hand, presents bright CrO<sub>x</sub>-CNS squares and dark as-grown CNS streets, suggesting an enhanced field emission property of CrO<sub>x</sub>-CNS. The turn-on field of CrO<sub>x</sub>-CNS is less than 4 V/μm since the patterned structure has already been visible in the FEEM image. Moreover, the almost equal brightness of CrO<sub>x</sub>-CNS squares over the entire field of view indicates their excellent emission uniformity. The slight brightness variation among CrO<sub>x</sub>-CNS squares is caused by the electron optics of the microscope.

*I-V* characteristics of patterned CrO<sub>x</sub>-CNS and as-grown CNS in the field of view of the microscope (300 μm in diameter) were measured during the FEEM observations. As noted, the patterned CrO<sub>x</sub>-CNS and as-grown CNS come from the same sample. Figure 5.6 shows the collected emission current of patterned CrO<sub>x</sub>-CNS and as-grown CNS as a function of the applied electric field. The error bars origin from the collected current fluctuation recorded at each measured field. No electron emission from as-grown CNS is detected in FEEM observations while the collected emission currents from as-grown CNS are less than 0.3 pA at all applied electric fields. We conclude that CNS do not turn on at the low applied electric fields of this instrument. On the other hand, the CrO<sub>x</sub>-CNS squares start emitting electrons at an applied electron field of 3.86 V/μm. Even though the collected emission current from the patterned CrO<sub>x</sub>-CNS is only 0.2 pA at this field, the CrO<sub>x</sub>-CNS squares are clearly visible in FEEM images. A turn-on field of 3.83 V/μm is quite consistent with our previous observations of CrO<sub>x</sub>-CNS. Thereafter, the collected emission current increases to 3.3 pA at an applied electric field of 4.61 V/μm.

PEEM and FEEM observations were also conducted on the CrO<sub>x</sub>-CNS sample with

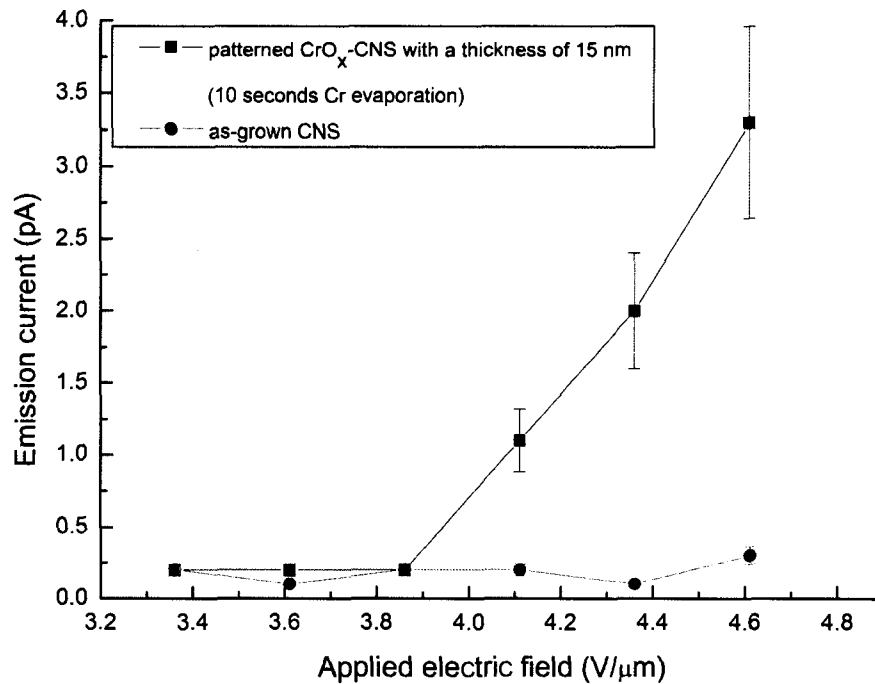


Figure 5.6 Collected emission currents of patterned CrO<sub>x</sub>-CNS and as-grown CNS as a function of the applied electric field.

a coating thickness of 1.5 nm (5 seconds Cr evaporation). Figure 5.7 displays FEEM images of the CrO<sub>x</sub>-CNS sample taken at various applied electric fields and the PEEM image taken from the same sample area at 4.33 V/μm. Here, the PEEM image, Fig. 5.7(a), is used as a reference for FEEM images, Figs. 5.7(b)-(e). The field of view in PEEM and FEEM images is 300 μm in diameter. The electron optic system and imaging system of PEEM were fixed during these observations. All FEEM images, shown in Figs. 5.7(b)-(e), indicate that the electron emission from CrO<sub>x</sub>-CNS is spatially uniform over the field of view with only a slight brightness variation caused by the electron optics.

(a) PEEM image taken at 4.34 V/ $\mu\text{m}$

(b) FEEM image taken at 4.34 V/ $\mu\text{m}$

(c) FEEM image taken at 4.08 V/ $\mu\text{m}$

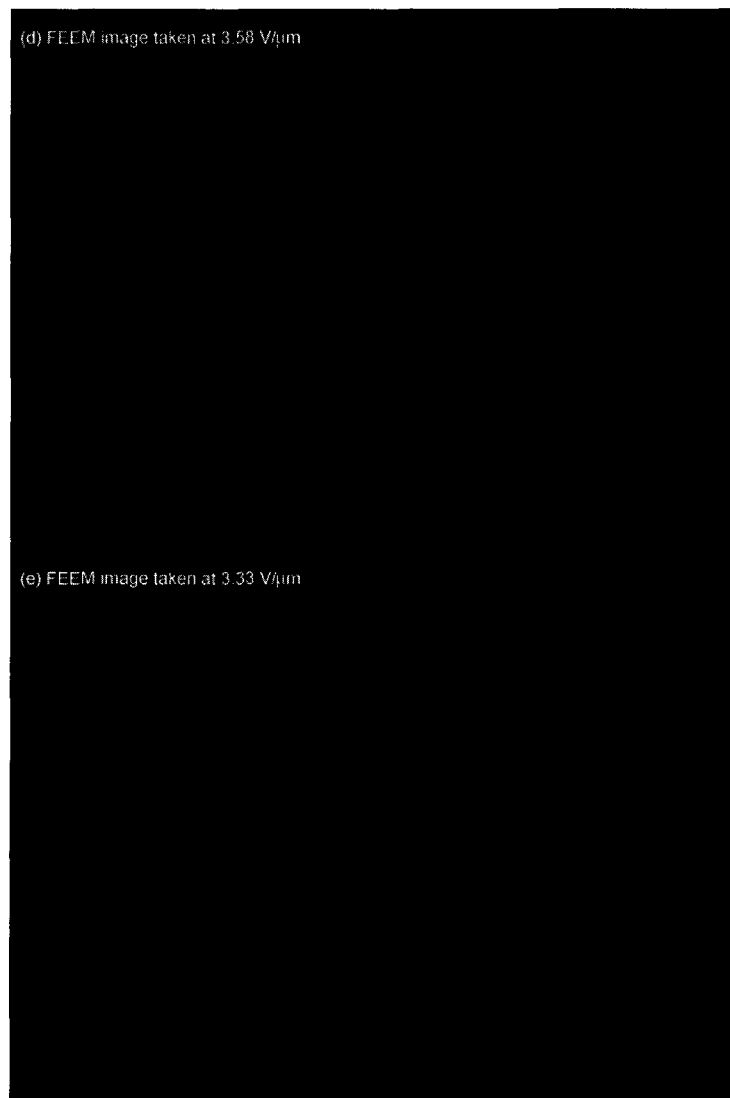


Figure 5.7 PEEM and FEEM images of  $\text{CrO}_x$ -CNS with a coating thickness of 1.5 nm. (a) PEEM image taken at  $4.34 \text{ V}/\mu\text{m}$  as a reference for FEEM images, (b) FEEM image taken at  $4.34 \text{ V}/\mu\text{m}$ , (c) FEEM image taken at  $4.08 \text{ V}/\mu\text{m}$ , (d) FEEM image taken at  $3.58 \text{ V}/\mu\text{m}$ , (e) FEEM image taken at  $3.33 \text{ V}/\mu\text{m}$ .

FEEM observations over the whole surface of the sample at various applied electric fields yield no hot runners, further confirming the spatially uniform emission of  $\text{CrO}_x\text{-CNS}$ . Although FEEM images of the  $\text{CrO}_x\text{-CNS}$  start being observed at an applied electric field of  $2.33 \text{ V}/\mu\text{m}$ , the PEEM imaging system could not record them until the field increased to  $3.33 \text{ V}/\mu\text{m}$ . So we conclude that the turn-on field of  $1.5 \text{ nm}$   $\text{CrO}_x\text{-CNS}$  is  $\sim 2.33 \text{ V}/\mu\text{m}$ . The in-situ  $I$ - $V$  characteristic of  $1.5 \text{ nm}$   $\text{CrO}_x\text{-CNS}$  from the field of view of the microscope was measured during FEEM observations. Figure 5.8 displays the collected emission current of the  $\text{CrO}_x\text{-CNS}$  as a function of the applied electric field. The collected current increases from  $1 \text{ pA}$  to  $43 \text{ pA}$  as the applied electric field increases from  $2.33$  to  $4.33 \text{ V}/\mu\text{m}$ , consistent with the increasing brightness of FEEM images demonstrated in Figs 5.7 (b)-(e) as the field increases. The error bars in the figure represent the collected current fluctuation recorded at each measured field.

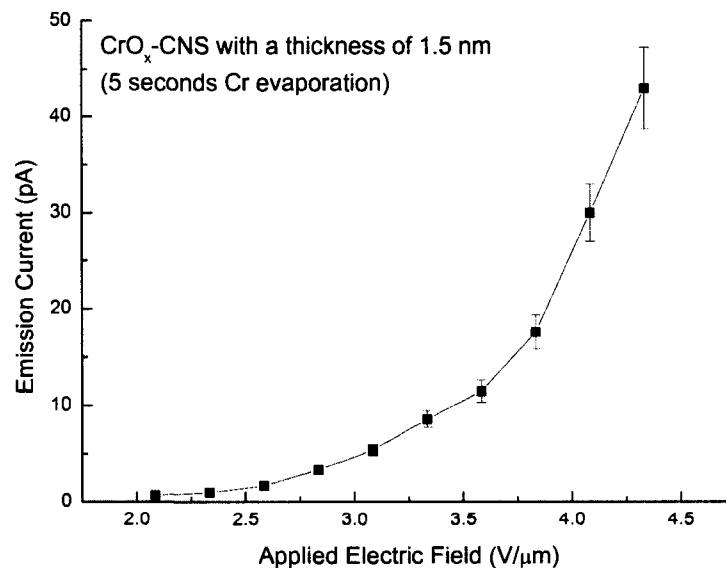


Figure 5.8 Collected emission current of  $\text{CrO}_x\text{-CNS}$  with a thickness of  $1.5 \text{ nm}$  as a function of the applied electric field.

Since the electron emission from CrO<sub>x</sub>-CNS with a coating thickness of 1.5 nm and 15 nm are uniform, a direct comparison of their spatially averaged field emission is valid so long as we count for the actual area incorporated in the field of views. Figure 5.9 displays the  $J$ - $V$  characteristics of CrO<sub>x</sub>-CNS with a coating thickness of 1.5 nm and 15 nm. The low collected current density measured here results from the electron loss during the transport in the electron optic system of PEEM. The 1.5nm CrO<sub>x</sub>-CNS has a far better field emission performance than the 15 nm CrO<sub>x</sub>-CNS according to the lower turn-on field and higher emission current at every value of the applied electric field.

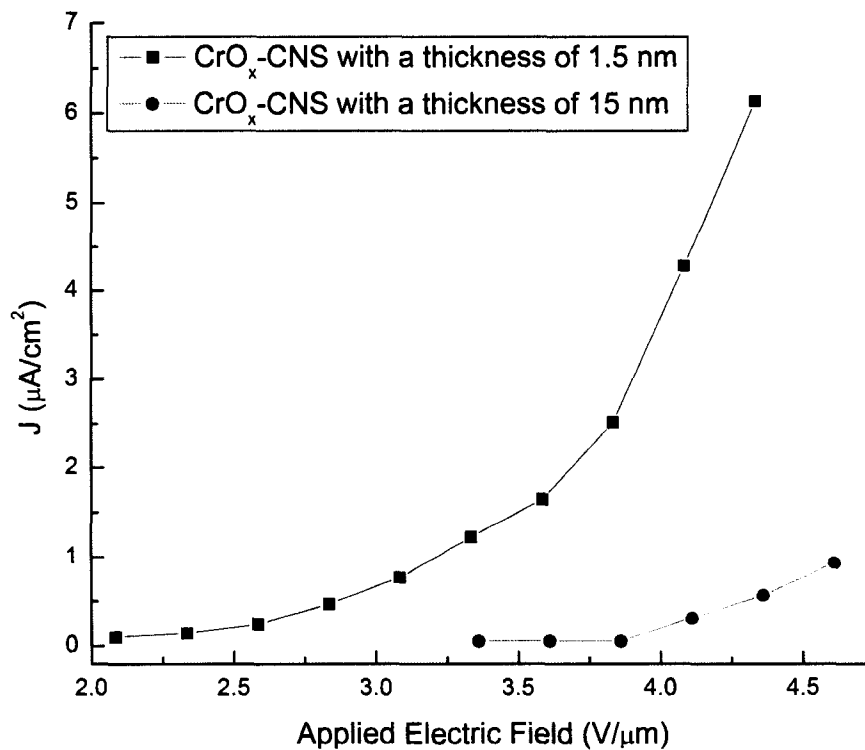


Figure 5.9  $J$ - $V$  characteristics of CrO<sub>x</sub>-CNS with a coating thicknesses of 1.5 nm and 15 nm.



Therefore, we suggest that the field emission performance of CrO<sub>x</sub>-CNS should depend on the coating thickness.

## 5.5 EFFECTS OF COATING THICKNESS ON FIELD EMISSION PERFORMANCE OF CrO<sub>x</sub>-CNS

The field emission properties of CrO<sub>x</sub>-CNS samples with a variety of coating thicknesses were studied using the diode holder assembly in the UHV test system. CrO<sub>x</sub>-CNS samples were used as the cathode and separated from a 6 mm wide copper anode by alumina spacers having a thickness of 254 μm. The chamber pressure was  $\sim 4 \times 10^{-8}$  Torr at the beginning of each test and the test area of samples was 30 mm<sup>2</sup>. The coating thickness of CrO<sub>x</sub>-CNS samples used in this study were controlled by Cr evaporation time, which are 2 seconds, 5 seconds, 10 seconds, and 15 second, respectively. The corresponding coating thicknesses are estimated to be 0.5 nm, 1.5 nm, 15 nm, and 20 nm, respectively (See Fig. 5.4). The as-grown CNS samples used to produce CrO<sub>x</sub>-CNS were cleaved from a central area of an as-grown CNS wafer four inches in diameter in order to minimize the height and morphology variation of CNS so that the change of the field emission of coated samples can be completely attributed to the thickness variation of coatings.

Figure 5.10 shows the emission current of CrO<sub>x</sub>-CNS having different thicknesses as a function of the applied electric field (*I-V* curves). Here, each *I-V* curve is the average of ten measurements from CrO<sub>x</sub>-CNS with the same coating thickness. The field emission data of these *I-V* curves are also summarized in Table 5.2. The as-grown CNS is used here as the reference for CrO<sub>x</sub>-CNS. The *I-V* curve of as-grown CNS shows a turn-on

field of  $4.25 \text{ V}/\mu\text{m}$ , consistent with our previous test results (See Sec. 4.5.1). Meanwhile, the applied electric field required for as-grown CNS to generate a peak current of  $1.45 \text{ mA}$  is  $8.9 \text{ V}/\mu\text{m}$ . The  $I$ - $V$  curves of  $\text{CrO}_x$ -CNS with a coating thickness of  $1.5 \text{ nm}$  and  $15 \text{ nm}$  reveal that their turn-on fields are  $2.4 \text{ V}/\mu\text{m}$  and  $3.9 \text{ V}/\mu\text{m}$ . The turn-on fields measured here are almost the same as those measured by FEEM (see Figs. 5.6 and 5.8), which are  $2.33 \text{ V}/\mu\text{m}$  for the  $1.5 \text{ nm}$  coating and  $3.83 \text{ V}/\mu\text{m}$  for the  $15 \text{ nm}$  coating. The applied electric fields to generate a peak current of  $1.45 \text{ mA}$  are  $5.0 \text{ V}/\mu\text{m}$  and  $8.5 \text{ V}/\mu\text{m}$  for the  $1.5 \text{ nm}$  coating and the  $15 \text{ nm}$  coating, respectively. Thus,  $\text{CrO}_x$ -CNS in thickness

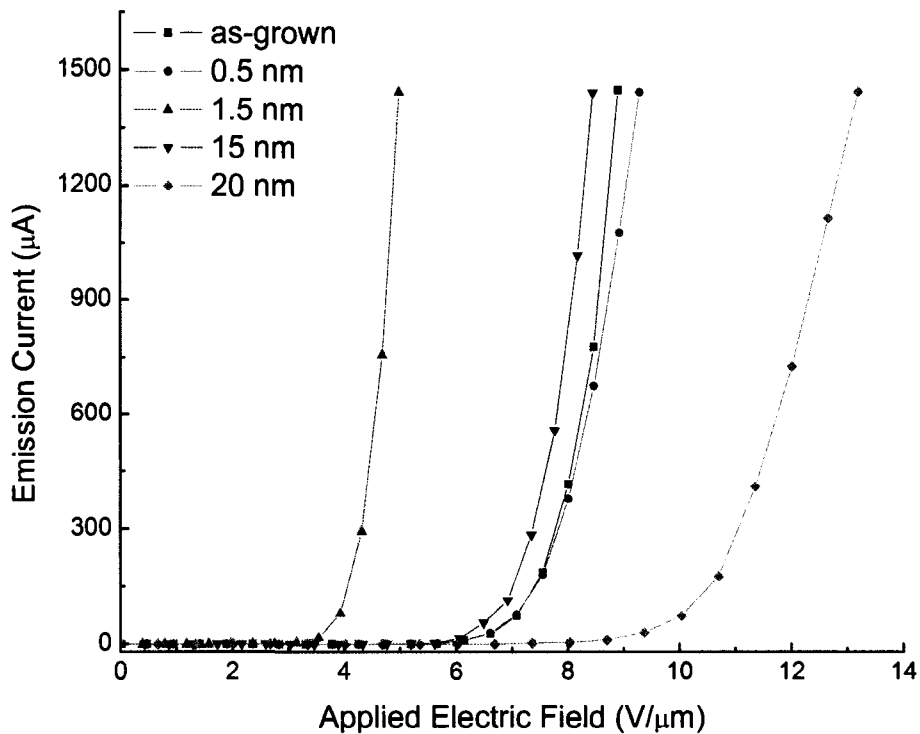


Figure 5.10 Emission currents of  $\text{CrO}_x$ -CNS with a variety of coating thicknesses as a function of the applied electric field. These  $I$ - $V$  curves show that the best field emission performance is achieved from  $\text{CrO}_x$ -CNS with a coating thickness of  $1.5 \text{ nm}$ .

up to 15 nm shows better field emission performances than as-grown CNS. Moreover, CrO<sub>x</sub>-CNS with a coating thickness of 1.5 nm shows a better field emission performance than those with a coating thickness of 15 nm, consistent with our previous results shown in Fig. 5.9.

The *I-V* curves of CrO<sub>x</sub>-CNS with a coating thickness of 0.5 nm and 20 nm have turn-on fields of 4.3 V/μm and 6.1 V/μm, respectively. The applied electric fields to generate a peak current of 1.45 mA are 9.3 V/μm for the 0.5 nm coating and 13.2 V/μm for the 20 nm coating. Thus, CrO<sub>x</sub>-CNS with a coating thickness too thin or too thick degrade CNS field emission performance. Only CrO<sub>x</sub>-CNS with appropriate coating thicknesses possess enhanced field emission performances compared to the as-grown CNS. In our case, the optimum thickness of CrO<sub>x</sub> coating on CNS appears to be 1.5 nm.

Latham et al[25] proposed a quasi-thermionic band diagram model to explain the enhanced electron emission performance of field emitters coated with a nano-scale dielectric film on the basis of field-induced band bending of the dielectric. There are two

Table 5.2 Turn-on fields and applied electric fields required to generate 1.445 mA emission current of CrO<sub>x</sub>-CNS samples with a variety of coating thicknesses.

	as-grown	0.5 nm CrO <sub>x</sub>	1.5 nm CrO <sub>x</sub>	15 nm CrO <sub>x</sub>	20 nm CrO <sub>x</sub>
Turn-on field* (V/ μm)	4.25	4.3	2.4	3.9	6.1
Field required to generate a peak current of 1.45 mA (V/ μm)	8.9	9.3	5.0	8.5	13.2

\*Turn on field is defined as the applied electric field under which 10 nA emission current is measured

main features of this model: (1) electron tunneling from emitters into the conduction band of the dielectric through a depletion layer at the emitter/dielectric interface, and (2) electron escape from the conduction band of the dielectric into vacuum quasi-thermionically through a small potential barrier. The  $I$ - $V$  characteristic of this model is nearly indistinguishable from the form originating from the Fowler-Nordheim mechanism. To apply this model to the experimental data, the dielectric requires a carrier concentration of  $10^{17} \text{ cm}^{-3}$  in its conduction band in order to form a thin depletion layer. Therefore, flat-band conditions may be assumed for the emitter/dielectric interface in the case of  $\text{CrO}_x$ -CNS. A schematic of the highly simplified planar band diagram of  $\text{CrO}_x$ -CNS with onset of electron emission is displayed in Figure 5.11. This model shows electrons ejection from CNS through two interfacial potential barriers to the vacuum. The electron emission of  $\text{CrO}_x$ -CNS in this model can be described as following processes: (1) electron tunneling from Fermi level of CNS into the conduction band of  $\text{CrO}_x$ , (2) electron thermalization during the transport from CNS/ $\text{CrO}_x$  interface to  $\text{CrO}_x$ /vacuum interface, (3) electron thermally-assisted tunneling from  $\text{CrO}_x$  into vacuum. The tunneling width of electrons ejected from the Fermi energy level of CNS is postulated to increase at the CNS/ $\text{CrO}_x$  interface with the increasing coating thickness because of the negative charge generated by the uncompensated electrons present in the dielectric. As a result, the field emission properties of  $\text{CrO}_x$ -CNS generally degrade with regard to increasing coating thicknesses. If the  $\text{CrO}_x$  coating is thinner than the tunneling width of electrons ejected from the Fermi energy level of CNS, as in the case of  $\text{CrO}_x$ -CNS with a thickness of 0.5 nm, electrons may not gain kinetic energy during their transport from CNS/ $\text{CrO}_x$  interface to  $\text{CrO}_x$ /vacuum interface. We suspect that the probability of

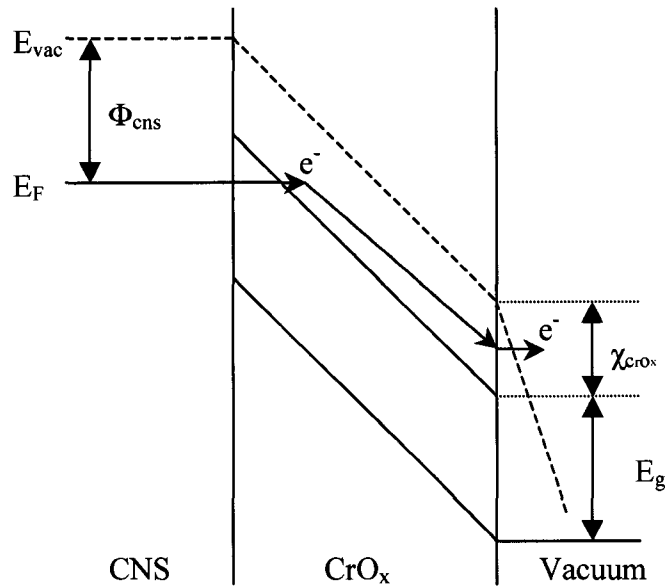


Figure 5.11 The band diagram of CrO<sub>x</sub>-CNS with onset of electron emission.

Here,  $\Phi_{CNS}$  is the work function of CNS,  $\chi_{CrO_x}$  is the electron affinity of CrO<sub>x</sub>, and  $E_g$  is the bandgap of CrO<sub>x</sub>.

electrons tunneling through these two barriers is smaller than that of electrons tunneling through the potential barrier acted on the surface of as-grown CNS, resulting in the degraded field emission performance of CrO<sub>x</sub>-CNS with a coating thickness of 0.5 nm as demonstrated in Fig. 5.10.

## 5.6 SUMMARY

We have fabricated a conformal CrO<sub>x</sub> coating of nano-scale thickness on carbon nanosheets using vacuum evaporation and subsequent atmospheric exposure. By controlling the evaporation time, a variety of CrO<sub>x</sub> coating thicknesses from 0.5 nm up to

20 nm were achieved. Material characterization methods, including SEM, EDX, AES, and Raman, were employed to study the morphology, composition, and structure of CrO<sub>x</sub>-CNS. The results reveal that CrO<sub>x</sub> is formed after Cr coated CNS is exposed to the atmosphere after vacuum evaporation of Cr.

PEEM was used to study the field emission properties of CrO<sub>x</sub>-CNS. FEEM observations revealed that a spatially uniform emission could be achieved from CrO<sub>x</sub>-CNS and suggest that the field emission performance of CrO<sub>x</sub>-CNS depended on the coating thickness. The in-situ I-V measurements during FEEM observations reveal that the field emission performance of CrO<sub>x</sub>-CNS with a coating thickness of 15 nm is better than as-grown CNS but worse than CrO<sub>x</sub>-CNS with a 1.5 nm coating.

The field emission properties of CrO<sub>x</sub>-CNS with a variety of thicknesses were studied by using the diode holder assembly in the UHV test apparatus. The results confirm that their field emission properties are closely related to the thicknesses of these coatings. Field emission properties of CrO<sub>x</sub>-CNS degrade when the coating is either too thin (0.5 nm) or too thick (20 nm), but field emission properties of CrO<sub>x</sub>-CNS improve when the thicknesses of the coating lies between 1.5 nm and 15 nm. According to the study, CrO<sub>x</sub>-CNS with a coating thickness of 1.5 nm has the best emission properties among all samples tested, which has the lowest turn on field (2.36 V/μm) and the lowest applied electric field (4.99 V/μm) to generate ~1.445 mA. Moreover, the test results of CrO<sub>x</sub>-CNS with a coating thickness of 1.5 nm and 15 nm are quite consistent with those measured during FEEM observations. A two-barrier model may account for the variation of field emission performance with regard to the coating thickness.

## References for Chapter V

- [1] Teo KBK, Minoux E, Hudanski L, Peauger F, Schnell J-P, Gangloff L, Legagneux P, Dieumegard D, Amaratunga GAJ, Milne WI. Microwave devices: Carbon nanotubes as cold cathodes. *Nature*. 2005;437(7061):968.
- [2] Minoux E, Groening O, Teo KBK, Dalal SH, Gangloff L, Schnell JP, Hudanski L, Bu IYY, Vincent P, Legagneux P, Amaratunga GAJ, Milne WI. Achieving High-Current Carbon Nanotube Emitters. *Nano Lett*. 2005;5(11):2135-8.
- [3] Baughman RH, Zakhidov AA, de Heer WA. Carbon Nanotubes--the Route Toward Applications. *Science*. 2002;297(5582):787-92.
- [4] Choi YS, Kang JH, Park YJ, Choi WB, Lee CJ, Jo SH, Lee CG, You JH, Jung JE, Lee NS, Kim JM. An under-gate triode structure field emission display with carbon nanotube emitters. *Diamond and Related Materials*. 2001;10(9-10):1705-8.
- [5] Wang S, Wang J, Miraldo P, Zhu M, Outlaw R, Hou K, Zhao X, Holloway BC, Manos D, Talmage T, Shenderova O, Mark R, Dalton J, McGuire G. High field emission reproducibility and stability of carbon nanosheets and nanosheet-based backgated triode emission devices. *Applied Physics Letters*. 2006;89(18):183103-3.
- [6] Tyler T, Shenderova O, Ray M, Dalton J, Wang J, Outlaw R, Zhu M, Zhao X, McGuire G, Holloway BC. Back-gated milliamperes-class field emission device based on carbon nanosheets. *Journal of Vacuum Science & Technology B: Microelectronics and Nanometer Structures*. 2006;24(5):2295-301.
- [7] Temple D. Recent progress in field emitter array development for high performance applications. *Materials Science and Engineering: R: Reports*. 1999;24(5):185-239.
- [8] Mackie WA, Morrissey JL, Hinrichs CH, Davis PR. Field emission from hafnium carbide. 38th National Symposium of the American Vacuum Society; 1992; Seattle, Washington (USA): AVS; 1992. p. 2852-6.
- [9] Mackie WA, Hartman RL, Anderson MA, Davis PR. Transition metal carbides for use as field emission cathodes. International vacuum microelectronics conference; 1994; Newport, Rhode Island (USA): AVS; 1994. p. 722-6.
- [10] Zhao X. Field emission study of carbon nanostructure. Williamsburg: College of William and Mary; 2006.
- [11] Zhirnov VV, Choi WB, Cuomo JJ, Hren JJ. Diamond coated Si and Mo field emitters: diamond thickness effect. *Applied Surface Science*. 1996;94-95:123-8.
- [12] Zhirnov VV, Lizzul-Rinne C, Wojak GJ, Sanwald RC, Cuomo JJ, Hren JJ. Optimizing high-current yields from diamond coated field emitters. *Journal of Vacuum Science & Technology B: Microelectronics and Nanometer Structures*. 2001;19(1):17-22.
- [13] Krauss AR, Auciello O, Ding MQ, Gruen DM, Huang Y, Zhirnov VV, Givargizov EI, Breskin A, Chechen R, Shefer E, Konov V, Pimenov S, Karabutov A, Rakhimov A, Suetin N. Electron field emission for ultrananocrystalline diamond films. *Journal of Applied Physics*. 2001;89(5):2958-67.
- [14] Latham R. *High Voltage Vacuum Insulation* Academic Press 1995.
- [15] Moon JS, Alegaonkar PS, Han JH, Lee TY, Yoo JB, Kim JM. Enhanced field emission properties of thin-multiwalled carbon nanotubes: Role of SiO<sub>x</sub> coating. *Journal of Applied Physics*. 2006;100(10):104303-7.

- [16] Yi WK, Jeong TW, Yu SG, Heo JN, Lee CS, Lee JH, Kim WS, Yoo JB, Kim JM. Field-Emission Characteristics from Wide-Bandgap Material-Coated Carbon Nanotubes. *Advanced Materials*. 2002;14(20):1464-8.
- [17] Mientus R, Grotchel R, Ellmer K. Optical and electronic properties of  $\text{CrO}_x\text{N}_y$  films, deposited by reactive DC magnetron sputtering in  $\text{Ar}/\text{N}_2/\text{O}_2(\text{N}_2\text{O})$  atmospheres. *Surface and Coatings Technology*. 2005;200(1-4):341-5.
- [18] Scherer H, Weimann T, Hinze P, Samwer BW, Zorin AB, Niemeyer J. Characterization of all-chromium tunnel junctions and single-electron tunneling devices fabricated by direct-writing multilayer technique. *Journal of Applied Physics*. 1999;86(12):6956-64.
- [19] Lee JW, Lee WJ, Sim KJ, Yi WK. 20th International Vacuum Nanoelectronics Conference; Chicago, IL: IEEE; 2007. p. 175.
- [20] Davis LE, MacDonald NC, Palmberg PW, Riach GE, Weber RE. *Handbook of Auger Electron Spectroscopy: Physical Electronics Industries, Inc.* 1976.
- [21] Li YS, Wang K, P.X. H, X. HB, Kovas P. Surface-enhanced Raman spectroelectrochemical studies of corrosion films on implant Co-Cr-Mo alloy in biosimulating solutions. *Journal of Raman Spectroscopy*. 1999;30(2):97-103.
- [22] Mougin J, Rosman N, Lucazeau G, Galerie A. In situ Raman monitoring of chromium oxide scale growth for stress determination. *Journal of Raman Spectroscopy*. 2001;32(9):739-44.
- [23] Tortet L, Guinneton F, Monnereau O, Stanoi D, Socol D, Mihailescu IN, Zhang T, Grigorescu C. Optimization of  $\text{Cr}_8\text{O}_{21}$  targets for pulsed laser deposition. *Crystal Research and Technology*. 2005;40(12):1124-7.
- [24] Habliston D, Birrel GB, Griffith OH. Photoelectron Imaging of DNA: A Study of Substrates and Contrast. *J Phys Chem*. 1993;97:3022-7.
- [25] Latham RV. The origin of prebreakdown electron emission from vacuum-insulated high voltage electrodes. *Vacuum*. 1982;32(3):137-40.



## CHAPTER VI

### SUMMARY AND FUTURE WORK

#### 6.1 SUMMARY

During the course of this work, the synthesis, characterization, and field emission properties of carbon nanostructures, including 1-D carbon nanofibers (CNF), 2-D carbon nanosheets (CNS), and 2-D chromium oxide coated carbon nanosheets ( $\text{CrO}_x\text{-CNS}$ ), have been studied as the electron source in vacuum microelectronic devices. The application of CNF and CNS as the emissive materials embedded in a novel back-gated triode field emission device has also briefly introduced.

We have employed a variety of materials characterization methods and apparatus to investigate the morphology, microstructure, composition and field emission properties of carbon nanostructures. These methods and apparatus are SEM, EDX, Raman, Auger, PEEM, FEEM and an FE test system. An introduction to these apparatus as well as their operational principles was briefly introduced in Chapter II. Three types of sample holder assemblies were used in FE measurements: cartridge holder assembly, diode holder assembly, and 24-pin header assembly. The merits and drawbacks of each sample holder assembly were discussed.

We presented the synthesis, characterization, and field emission properties of 1-D CNF. A direct current plasma enhanced chemical vapor deposition (DC PECVD) system was designed and constructed for the purpose of direct CNF growth on metallic

substrates. We have successfully synthesized both spaghetti-like CNF and aligned CNF on blank TiW substrates without using a buffer layer. By adjusting the plasma power, we found that the degree of alignment of deposited CNF could be controlled. Spaghetti-like CNF with a high degree of nanoscale graphitic ordering were fabricated at lower plasma powers, while aligned CNF with a higher degree of nanoscale disorder were grown at higher plasma powers. We suggested that the morphology of CNF deposited on TiW substrates is determined by the electric field generated in the plasma sheath and by the growth rate of CNF, which can be tuned by the plasma power. The field emission properties of CNF deposited on blank TiW substrates were measured.

The processes to fabricate both spaghetti-like and aligned CNF on TiW lines of controlled cross-sectional profiles to create back-gated triode field emission devices were described. Only aligned CNF based back-gated triode field emission devices survive our present wet-cleaning post processing steps to remove co-deposited amorphous carbon from the dielectric layer. These devices, using aligned CNF as the cathode, were measured for diode and triode field emission operations by using the 24-pin header assembly. The results indicated that back gate triode operation yielded greatly enhanced field emission performance of these devices.

We also presented the synthesis, characterization, and field emission properties of 2-D CNS. In this study, CNS were deposited on four-inch Si wafers in inductively coupled plasma using 4 sccm CH<sub>4</sub> and 6 sccm H<sub>2</sub> gas composition with a chamber pressure of 100 mTorr and an input RF power of 900W at a substrate temperature of 700 °C. Materials characterization revealed that CNS was hundreds of nanometers in length and height, but only <1-4 nm in thickness. Further, these measurements show that

the honeycomb-like morphology, graphitic structure, and atomic thickness of CNS can be fabricated on a variety of substrates, including Si, Al<sub>2</sub>O<sub>3</sub>, SiO<sub>2</sub>, Ni, Ti, W, TiW, Mo, Cu, Au, Pt, Zr, Hf, Nb, Ta, Cr, 304 Stainless steel, and graphite, without the need for catalysts.

The field emission properties of as-grown CNS have been studied using the diode holder assembly from a broad range of perspectives, such as turn-on and threshold field, maximum total current, lifetime in a slow pulse mode, lifetime in a direct current mode, and emission uniformity. We showed that the turn-on and threshold field of as-grown CNS lie in the range from 3 to 4.7 V/ $\mu$ m and 3.5 to 5.2 V/ $\mu$ m, respectively. So far, a peak current of 33 mA has been measured from an as-grown CNS sample with a test area of 32 mm<sup>2</sup> at an applied electric field of 26.8 V/ $\mu$ m. Further, we routinely achieved a total current of more than 20 mA from as-grown CNS samples with test areas of  $\sim$ 30 mm<sup>2</sup>. After an as-grown CNS sample was electrically conditioned for half an hour, we showed more than 200 hours of stable emission in a slow pulse mode. These test results suggest that CNS may have better field emission properties than single metal single tips, carbon nanotubes/nanofibers, and diamond when high total-currents and long-life are required.

The study of the field emission behavior of CNS was carried out by applying Fowler-Nordheim equation to field emission characteristics (*I-V* curves) of the as-grown CNS sample collected immediately before and after the dc lifetime test. The slope of *F-N* plots and the intercept of *F-N* plots with  $\ln(I/V^2)$  axis were used to determine the field amplification factor and emission area by substituting an assumed work function of as-grown CNS into the Fowler-Nordheim equation. The results suggest that a small number of the numerous possible nanosheet emission sites (hot runners) dominate the emission

current. These hot runners are most likely removed through the thermal runaway process during the conditioning process, leading to the turn-on of more emitters with lower field amplification factors. Therefore, removal of hot runners leads to a very stable field emission of 1.5 mA on as-grown CNS samples. PEEM and FEEM observations confirmed the existence of hot runners in unconditioned CNS. The in-situ  $I$ - $V$  measurements of hot runners reveal their unpredictable and unstable emission. In addition, these studies validated the effectiveness of back-gated triode field emission device design.

This thesis presented the synthesis, characterization, and field emission properties of chromium oxide coated carbon nanosheets ( $\text{CrO}_x$ -CNS). A conformal chromium oxide coating in a nanoscale thickness was fabricated on as-grown CNS by vacuum evaporating a thin Cr layer and subsequently exposing to the atmosphere. A variety of  $\text{CrO}_x$  coating thicknesses from 0.5 nm to 20 nm are achieved by controlling the evaporation duration. The material characterizations confirm the formation of  $\text{CrO}_x$ , most likely  $\text{Cr}_2\text{O}_3$ , on as-grown CNS after the coating process. PEEM observations and simultaneous in-situ  $I$ - $V$  measurements presented that  $\text{CrO}_x$ -CNS with a coating thickness of 1.5 nm and 15 nm had not only enhanced field emission properties but also excellent emission uniformity. This was probably the first time that such an excellent emission uniformity has ever been seen on a wide-field carbon nanostructure. These observations suggest that the field emission performance of  $\text{CrO}_x$ -CNS depends on the coating thickness.

The field emission properties of  $\text{CrO}_x$ -CNS were also studied using the diode holder assembly for various coating thicknesses. Field emission properties of  $\text{CrO}_x$ -CNS degraded when the coating is too thin (0.5 nm) or too thick (20 nm), but enhanced when

the coating thickness ranging from 1.5-15 nm. A CrO<sub>x</sub>-CNS sample with a coating thickness of 1.5 nm had the best emission property among all samples with various coating thicknesses with respect to the lowest turn-on field (2.36 V/μm) and the lowest field to generate specified current. We proposed a two-barrier model to interpret the effect of coating thickness on the field emission performance of CrO<sub>x</sub>-CNS.

## 6.2 FUTURE WORK

In this work, a 2-D carbon nanostructure that we have called carbon nanosheets has been confirmed as a promising candidate for the application as the electron source in vacuum microelectronic devices. Future work should focus on improving emission stability, uniformity, and lifetime of CNS at currents of tens (or hundreds) of milliamperes.

### 6.2.1 STUDY ON WORK FUNCTION OF CARBON NANOSHEETS

We studied the field emission behavior of carbon nanosheets by applying the Fowler-Nordheim equation to collected  $I$ - $V$  curves and their corresponding  $F$ - $N$  plots before and after the dc lifetime test. In this work, we assumed that the value of the work function of carbon nanosheets was equal to that of graphite (4.8 eV). However, the work function of CNS may be considerably different from 4.8 eV as a result of hydrogen adsorbates at the terminating edges of CNS. Therefore, it remains an open challenge to accurately measure the work function of CNS.

One technical approach to measure the work function of CNS is to acquire the field emission energy distribution (FEED) using field emission energy spectrometry (FEES).

From an accurate measurement of the peak position of FEED, the work function of CNS could be accurately determined. Moreover, the peak width can tell the energy spread of emitted electrons from CNS, which is important for the device applications. Preliminary work along these lines was begun in our laboratory [1], but needs to be continued for a wider variety of conditions.

### 6.2.2 PEEM AND FEEM MEASUREMENTS ON CNS

This thesis has demonstrated that emission sites of as-grown CNS samples and their I-V curves can be measured during PEEM and FEEM observations. However, FEEM observations after conditioning could not be done because the maximum applied electric field of the instrument we had available was limited by the high voltage power supply applied due to safety considerations. Conditioning has been studied on wide area emitters by using phosphor screens to form emission images [2], but the resolution of the phosphor screen is too low to provide enough details for quantitative analysis of the field emission performance of emissive materials. Therefore, a higher voltage PEEM apparatus will be necessary for this purpose.

By comparing PEEM and FEEM observations and in-situ  $I-V$  measurements of CNS sample before and after the conditioning process, some important parameters and phenomena with regard to the conditioning process can be discovered. These include details on the processes that eliminate hot runners, increase emission site density, and decrease the emission current. Learning the details of these processes would guide the development of more efficient conditioning procedures.

### 6.2.3 EFFECTS OF H<sub>2</sub>O ON FIELD EMISSION PROPERTIES OF CNS

All field emission tests presented in this work were conducted in an un-baked UHV test system. As a result, a large amount of residual H<sub>2</sub>O was present in the test system, affecting the field emission properties of CNS. Dean et al[3] reported that H<sub>2</sub>O can initially improve the field emission performance of CNT by introducing an adsorbate energy state to CNT, but in the longer run degrades the performance by ion bombardment. Thus, at times of tens of hours, these workers saw emission instability during their dc lifetime test.

One simple technical approach to study H<sub>2</sub>O effect is through comparing I-V curves and dc lifetime test results collected from the same sample in un-baked and baked test system, respectively. Meanwhile, the H<sub>2</sub>O pressure change must be carefully monitored and recorded during these tests to determine whether such changes correlate with the field emission properties of CNS.

### 6.2.4 EFFECT OF ANODE AND CATHODE TEMPERATURE ON FIELD EMISSION PROPERTIES OF CNS

One experimental observation during dc lifetime tests was that the temperature increased in the copper anode. At 5 mA and 5000 V, the continuous 25 W causes the chamber pressure to change from  $\sim 1 \times 10^{-9}$  Torr to  $\sim 5 \times 10^{-6}$  Torr. This enhanced outgassing from the anode and the nearby structures is indicative of a much higher pressure still in the anode-cathode gap. Such a pressure leads to arcing and irreversible damage to the CNS cathode. Consequently, we have not yet found the intrinsic limitation of the maximum field emission current density for this material.

In this work, we have described a thermal runaway process associated with the existence of hot runners. The peak temperature of a hot runner is determined not only by the emission current density at emitters but also by the thermal transport along CNS to the substrate. Therefore, if more efficient the thermal transport can be achieved, a higher stable emission current might be achieved even in the presence of a small number of hot runners. Consequently, measuring the local surface temperature of the cathode is an important improvement to the current level of experiments.

To do so, the test chamber and sample holder assembly have to be modified to permit thermocouples, or other thin-film devices to contact multiple locations of the anode and cathode. A multiplicity of current-time and temperature-time measures could then be used to construct an accurate thermal model of the surface temperature.

#### 6.2.5 STUDY ON FIELD EMISSION PROPERTIES OF WIDE-BANDGAP MATERIAL COATED CNS

We have presented field emission properties of  $\text{CrO}_x$ -CNS. The results indicated that  $\text{CrO}_x$ -CNS had improved turn-on field and lowered field levels to achieve a given current. We also showed that emission uniformity of  $\text{CrO}_x$ -CNS is much better than CNT/CNF and as-deposited CNS. Unlike the  $\text{Mo}_2\text{C}$ -CNS that takes advantage of low work function of  $\text{Mo}_2\text{C}$ , we suggested that  $\text{CrO}_x$ -CNS depends on a combination of field-induced band bending in a dielectric overlayer, coupled to a quasi-thermionic enhancement of tunneling through that dielectric. Therefore, wide-bandgap coating materials may be useful to improve field emission performance of carbon nanostructures.  $\text{CrO}_x$  may not be the best wide-bandgap material for such a purpose. Therefore, a



systematic study of a variety of wide-bandgap materials should be measured as the functional coating of CNS. These would include SiO<sub>2</sub>, MgO, ScO<sub>x</sub>, YO<sub>x</sub>, and perhaps a sequence of heavier oxides such as Rh<sub>2</sub>O<sub>3</sub>.

#### 6.2.6 CNS GROWTH PARAMETERS OPTIMIZATION

So far, we have shown that CNS have competitive field emission properties to be an electron emissive material for application as electron source in vacuum microelectronic devices. The field emission properties of CNS can be improved by optimizing their growth parameters in order to synthesize dispersive nanosheets on substrates, resulting in the minimum screening effects originated from the similarity of neighboring emitters.

One approach is making aligned CNS on the whole substrate surface. We have successfully synthesized aligned CNS in a small peripheral area by contacting a grounded electrode to the substrate. It is suspected that the change of the plasma sheath surrounded the contact point of grounded electrode causes alignment of the CNS. To achieve a large scale growth of aligned CNS, the change of plasma sheath surrounding the grounded electrode has to be experimentally studied while the grounded multi-electrode system on Si substrates has to be carefully designed.

Another approach is altering the emitter characteristics using photolithographic techniques to control emitter densities with designed pattern. Systematic studies would be needed to find the optimal emitter density of CNS.

## References for Chapter VI

- [1] Zhao X. Field emission study of carbon nanostructure: College of William and Mary; 2006.
- [2] Liang XH, Deng SZ, Xu NS, Chen J, Huang NY, She JC. On achieving better uniform carbon nanotube field emission by electrical treatment and the underlying mechanism. *Applied Physics Letters*. 2006;88(11):111501-3.
- [3] Dean KA, Chalamala BR. The environmental stability of field emission from single-walled carbon nanotubes. *Applied Physics Letters*. 1999;75(19):3017-9.

## VITA

Kun Hou was born in Harbin, Heilongjiang Province, China on January 11, 1976. He graduated from Harbin No. 3 High School in June 1994. He was enrolled in Materials Science and Engineering Department at Zhejiang University, Hangzhou, China in September 1994. He received his Bachelor of Engineering degree with a concentration in Metal Materials in July 1998.

He worked for Synjones Incorporated as a sales representative from September 1998 to July 2000. Afterwards, he was enrolled in the graduate program of Zhejiang University in August 2000. He received his Master of Engineering in Materials Science and Engineering in April 2003. His graduate research focused on studies of the friction properties of carbon nanorods synthesized on anodic aluminum oxide template by chemical vapor deposition.

In August 2003, he was admitted to the graduate program of Applied Science department at College of William and Mary. In September 2007, he successfully completed his graduate research program and passed the oral examination for the degree of Doctor of Philosophy with a concentration in Materials Science and Engineering from College of William and Mary.